

211

A Model for Converting SI Engine Flame Arrival Signals into Flame Contours

by

Nicolas G. Hadjiconstantinou

Bachelor of Science in Engineering
Cambridge University, U.K.
(1993)

SUBMITTED TO THE DEPARTMENT OF
MECHANICAL ENGINEERING IN PARTIAL
FULFILLMENT OF THE REQUIREMENTS
FOR THE DEGREE OF

MASTER OF SCIENCE IN MECHANICAL ENGINEERING

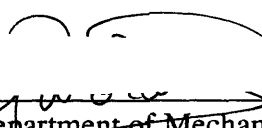
at the

MASSACHUSETTS INSTITUTE OF TECHNOLOGY

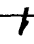
January 1995

©1994 Massachusetts Institute of Technology
All rights reserved

Signature of Author _____


Department of Mechanical Engineering
15 January 1995

Certified by _____


John B. Heywood
Professor, Department of Mechanical Engineering
Thesis Supervisor

Accepted by _____


Ain A. Sonin
Chairman, Departmental Graduate Committee

Eng.

MASSACHUSETTS INSTITUTE
OF TECHNOLOGY

APR 06 1995

LIBRARIES

A Model for Converting SI Engine Flame Arrival Signals into Flame Contours

by

Nicolas G. Hadjiconstantinou

Submitted to the department of Mechanical Engineering
on January 15, 1995 in Partial fulfillment of the
Requirements for the Degree of Master of Science

Abstract

A model was formulated which converts flame arrival times at a set of head gasket ionization probes into flame contours at any time required. The head gasket was manufactured at MIT using printed circuit board techniques. It has eight electrodes symmetrically spaced around the circumference (top of cylinder liner) and it replaces the conventional head gasket.

The model is based on flame contour data taken from the literature. Data from optical studies of combustion or studies utilizing optical fibre or ionization probe diagnostics are processed in terms of the apparent flame speed and the entrainment speed (flame speed relative to the fluid ahead). This allows inferences to be made about the general way in which a flame behaves in the cylinder of an S.I. engine. Then by applying the processing procedure backwards we can estimate how the flame develops in any combustion chamber given its geometrical characteristics and the ionization probe arrival times.

Experiments were run in order to check the accuracy of the model's predictions. Eighteen different operating conditions were tested which included variations of equivalence ratio, engine speed, and flowfield inside the combustion chamber. The overall agreement between the model and the experiments was good. Calculations were also done using a thermodynamic burn-rate analysis that gave the mass fraction of the mixture burned at a given time. This was compared to the mass fraction burned predicted from the model-derived flame contours and good agreement was found.

The above experimental set up and analysis procedure was then coupled to a fast response FID in order to examine the behavior of the hydrocarbon emissions when the combustion quality deteriorates. For this reason the experiments were conducted at very lean operating conditions. It was interesting to find that when the equivalence ratio reaches about 1.4 the in cylinder oxidation as well as exhaust port oxidation stops being important and an increase in emissions is observed for slow burning cycles. It was also observed that partial burns occur during the latest part of the cycle (5% mass left to burn) and they can be either local or global (resulting from global slow burning). In both cases they usually occur too late in the cycle to be observed using the ion probe signals. Sampling very close to the

exhaust valve gives the actual hydrocarbon emission profile as it comes out of the cylinder. However, the concentration is non-uniform across the exhaust port cross section and hence by sampling at one location only the information obtained is incomplete.

Thesis Supervisor: John B. Heywood

**Title: Sun Jae Professor of Mechanical Engineering
Director, Sloan Automotive Laboratory**

To my Parents

GEORGE

and

ATHENA

HADJICONSTANTINOU

ACKNOWLEDGEMENTS

There so many people that the least I have to do for them is to thank them! Without them my work here at the Sloan automotive laboratory would have been almost impossible. Not just because they gave me the answer to many of my questions but also for making the laboratory such a nice place to work in.

I am most grateful to Professor John B. Heywood, my thesis advisor for his invaluable guidance and encouragement in the course of this work. I would also like to thank Professor Wai K. Cheng for his guidance and assistance. Without his expertise in almost anything somebody could imagine many of the experiments wouldn't have been possible. I am indebted to Olivier Salvat from which I inherited the current project. Along with the project I inherited his vast knowledge on diagnostics (definitely not all of it) and also invaluable programs masterfully written by him for processing the ionization probe signals. The discussions we had together were as useful as the hardware support he provided for the various experiments. Thanks to Ed Cheng for his help during my early (and difficult) times in the lab. I also have to thank Kyoungdoug Min (the hydrocarbon emissions expert) for his advise and also invaluable help during the last part of the experimental work. He was a great asset both in setting up the experiments as in providing the programs for the data analysis.

I would like to thank all the students of the Sloan laboratory for their advice and willingness to help. Special thanks to Pete Hinze, Jonathan Fox, Jan-Roger Linna, Mike Norris, for their advice and help. Also special thanks to Joan Kenney probably the best secretary there is. I am also indebted to Brian Corkum for his invaluable help in the course of my experiments and for the huge number of things he has taught me during the past year. I would also like to thank Don Fitzgerald for the technical support he provided for my experiments. I would also like to extend special thanks to Wolf Bauer for the stimulating (and endless) discussions we had during the course of this work. Having discussions with him has been a huge insight gaining experience.

This work has been supported (both financially and intellectually) by the Industrial Consortium for Engine Research. Member companies are Chrysler Motors Corporation, Ford Motor Company, General Motors Research, Peugeot S.A, Renault and Volvo Car Corporation.

Nicolas Hadjiconstantinou
January, 1995

Table of Contents

Abstract	2
Acknowledgements	5
Table of Contents	6
List of Tables	7
List of Figures	8
Chapter 1: Introduction	11
1.1 Background	11
1.2 Objectives	12
Chapter 2: Experimental Work	13
2.1 Experimental Apparatus	13
2.2 The Head Gasket Ionization Probe	14
2.3 Verification Experiments	15
2.4 The Fast Response F.I.D.	15
Chapter 3: Data Acquisition and Processing	23
3.1 Data Acquisition	23
3.2 Signal processing	23
3.2.1 Ionization Probe Signals	24
3.2.2 Exhaust Gas Hydrocarbon Concentration Signals	24
Chapter 4: Modelling the Flame Evolution Inside the Cylinder	28
4.1 Background	28
4.2 Model Description	28
Chapter 5: Verification Experiments	43
5.1 Method	43
5.2 Results	44

Chapter 6: Investigation of Poor Combustion Quality Operating Conditions	57
6.1 Background	57
6.2 Experimental Results	57
6.3 Changing the Sampling Location	60
6.4 Conclusions	61
Chapter 7: Summary and Conclusions.....	83
7.1 Summary	83
7.2 Conclusions	83
Appendix A.....	85
Appendix B.....	87
References	88

List of Tables

Table 2.1	Ricardo Engine Geometry	17
Table 2.2	Flow Room Test Results	17
Table 5.1	Verification Experiment Set up	49
Table 6.1	Comparison of Single Cycle Hydrocarbon Emission Profiles	64
Table 6.2	Comparison of Single Cycle Hydrocarbon Emission Profiles	65
Table 6.3	Comparison of Single Cycle Hydrocarbon Emission Profiles	66
Table 6.4	Summary	67

List of Figures

Figure 2.1 Schematic of the ionization probe used in this study. (a) shows the top view and (b) shows a cross-sectional view.

Figure 2.2 Relative (to cylinder head geometry) orientation of the ionization probe electrodes.

Figure 2.3 Location of the extra ionization probes fitted for the model verification experiments.

Figure 2.4 Schematic of the Fast Response FID.

Figure 2.5 Schematic of FR FID sampling at a distance of 15 cm from the exhaust valve seat.

Figure 3.1 Example of ionization probe signal and arrival time definition.

Figure 3.2 Polar diagram of arrival times as defined by setting different thresholds.

Figure 4.1 Example of data for flame propagation obtained from SAE paper 902126.

Figure 4.2 Summary of all flame propagation data obtained from the literature.

Figure 4.3 Flame Front definition

Figure 4.4 Calculation results for the ratio of apparent flame speed to entrainment speed for the Ricardo Hydra MK II.

Figure 4.5 Variation of entrainment speed with mass fraction entrained for the three engines analysed and assumed variation for the Ricardo Hydra engine.

Figure 4.6 Variation of entrainment speed with mass fraction entrained for the Ricardo Hydra engine-Modelling wall effects.

Figure 4.7 Flame evolution profile for the Ricardo Hydra engine.

Figure 5.1 Verification experiment results. The predicted flame location (as calculated from

:

the eight arrival times) at the time of arrival of the flame at the two (extra) ionization probes is plotted for 18 different operating conditions. Primes denote lean air/fuel ratio, $\lambda=1.1$ for 900 rpm, $\lambda=1.25$ otherwise. Averages over 350 cycles.

Figure 5.2 Verification experiment results. The predicted flame location (as calculated from the eight arrival times) at the time of arrival of the flame at the optical spark plug is plotted for 6 different operating conditions. Averages over 350 cycles.

Figure 5.3 Correction required resulting from the flame lagging at the wall.

Figure 5.4 Verification experiment results. Frequency plot of one of the operating conditions (2500 rpm, $\lambda=1$, swirling flow).

Figure 5.5 Effect of changing the flow field on the flame contours.

Figure 5.6 Effect of changing the equivalence ratio on the flame contours.

Figure 5.7 Comparison of mass fraction burned as predicted by the model and by an independent pressure trace analysis.

Figure 5.8 Examples of individual cycles demonstrating cyclic variability. Inlet pressure is 0.5 bar and λ is 1.

Figure 6.1 Mass averaged hydrocarbon emissions plotted against max pressure for 120 cycles.

Figure 6.2 Mass averaged hydrocarbon emissions plotted against max pressure for 120 cycles.

Figure 6.3 Mass averaged hydrocarbon emissions plotted against max pressure for 120 cycles.

Figure 6.4 Relation between the 'Effective flame radius' and max pressure for 120 cycles at

1600 rpm 0.5 bar and $\lambda=1.45$.

Figure 6.5 Investigation of single cycle behavior.

Figure 6.6 Representative flame evolution contours for the four regions identified in figure 6.5.

Figure 6.7 Representative single cycle hydrocarbon emissions profiles for the regions identified in figure 6.5.

Figure 6.8 Representative single cycle hydrocarbon emissions profiles for the regions identified in figure 6.5.

Figure 6.9 Mass averaged hydrocarbon emissions plotted against cycle IMEP for 120 cycles at 1600 rpm, 0.5 bar, $\lambda=1.45$.

Figure 6.10 Mass averaged hydrocarbon emissions plotted against cycle IMEP for 120 cycles at 1600 rpm, 0.5 bar, $\lambda=1$.

Figure 6.11 Investigation of flame arrival times of high emitting cycles.

Figure 6.12 Examples of individual cycles from region 3

Figure 6.13 Examples of individual cycles from region 4

Figure 6.14 Schematic of the three different sampling locations for the FR FID.

Figure 6.15 Averaged emission profiles (200 cycles) with sampling position close to exhaust valve. (a) In the center of the exhaust port and (b) close to the port wall.

Figure 6.16 Examples of different high hydrocarbon emitting behavior at 1600 rpm, 0.5 bar, $\lambda=1.45$.

Chapter 1: Introduction

1.1 Background

The internal combustion engine and particularly the spark ignition type has been around for so many years that an enormous amount of development work has been expended on it. Developers are now facing the toughest of the requirements (emission and noise pollution for example) the internal combustion engine has been subjected to for its long life period. One of the most important tools at the researcher's-developer's disposal are the various kinds of diagnostics. The most widely used one is the pressure transducer which can provide invaluable information (following from an analysis of the pressure trace) about the flame growth process after the ignition of the fuel-air mixture in the engine cylinder.

One of the more recent developments in this area is the use of sets of ionization probes to monitor the time of flame arrival at specified locations in the cylinder. The idea of an ionization probe is not new. Flame speeds are usually calculated by measuring the time taken by the flame to travel between two probes in a combustion bomb. Use of ionization probes in engines was reported in 1934 [1]. Their major disadvantage was the complexity of installation and the fact that modifications had to be made to the engine in order for them to be accommodated. Muller et al. [2] proposed the integration of the ionization probes to the head gasket of the engine. This would make the installation fairly easy. More importantly, however, this technique ensured that the ionization probes could be installed on production engines with no modification and it can only be a number of years before they become a permanent feature of production engines as a part of their management system. Witze et al. [3] was the first to introduce the idea of a head gasket made from circuit board material, replacing the conventional head gasket. This resulted in a cost effective and robust diagnostic as further results suggested [4,5].

1.2. Objectives:

An ionization probe installed between the cylinder head and the liner will give flame arrival times at the probe electrodes. In our case the probe had eight electrodes. Arrival times, however, are not easy to interpret. They are (roughly) inverse to flame speed. Their absolute magnitude depends on many factors and also on the operating conditions. A concise way to display all the information possible, without making the procedure cumbersome, is by means of flame shapes at given time intervals after ignition. This, however, requires knowledge of the flame evolution behaviour for the whole of the burn duration. The objective of this study was therefore:

- 1) To develop a model that would estimate the flame contours at any time, given the flame arrival times at the ionization probe electrodes.
- 2) Test the model for accuracy
- 3) Use the model to investigate the characteristics of the slow or partial burning cycles in conjunction with the hydrocarbon emissions resulting from those cycles.

Chapter 2: Experimental work

2.1 Experimental apparatus:

The engine used for the experimental part of this study was the Ricardo Hydra Mark III single cylinder research engine. The engine has two valves and two overhead camshafts, each driving a single valve. The combustion chamber shape is hemispherical with a radius of curvature of 51 mm. The spark plug lies between the two valves but is offset from the center by 17 mm. A similar hole, symmetrically placed with respect to the center of the combustion chamber accommodates the water-cooled Kistler 7061 pressure transducer connected to a Kistler 5026 charge amplifier (Fig.2.2). Table 2.1 lists relevant engine data and geometry.

A laminar air flow element was used to measure the volumetric air flow rate into the engine. The air/fuel ratio was measured by an NTK model MO-100 air/fuel ratio analyser (lambda sensor). The engine was water cooled as described in [6]. The cooling water flow rate was set to its maximum in an attempt to keep the head gasket as cool as possible. The durability of circuit board material when used in such adverse environments such as the combustion chamber of a S.I. engine was not expected to be good. It was encouraging to find out (after removing the cylinder head) that after 100+ hours of operation the head gasket is only very slightly recessed. The load, however, was relatively low (inlet pressure 0.5 bar) the maximum pressure in the cylinder being always less than 40 bar.

The engine was connected to an Eaton Dynamatic Model AF 6360 dynamometer via the crankshaft. This variable frequency dynamometer is both capable of motoring the engine and absorbing power in either constant load or constant speed mode. In our experiments it was set to the constant speed mode in which it provides the required load to the engine in order to keep it running at the same speed.

Because of the hemispherical combustion chamber shape and the cross-flow valve arrangement the flow field was characterised as a weak tumbling one (baseline case). Experiments were also performed with a modified flowfield. This was achieved by inserting deflector plates inside the inlet port. Measurements performed at the Chrysler Powertrain Engineering Flow Room showed that a moderate swirling flow could be generated by the swirl inducing plate and a different level of tumble compared to the baseline case was generated by the tumble inducing plate. When the effect of flowfield was examined a restrictor plate was added to the baseline case in order to account for the restriction introduced by the deflector plates.

The engine was operated with an optical fibre instrumented spark plug, described in [3]. The reason for this was that at the same time the above experiments were performed parallel work was being done for the development of this diagnostic. This spark plug differs in geometry from the conventional spark plugs for obvious reasons. For the above reason all the experiments were performed with MBT (Maximum Brake Torque) spark timing. The experiments concerning the hydrocarbon emissions were performed using a normal NGK spark plug again with MBT spark timing.

The fuel supply system was relatively simple. The Hydra, being a research engine, can be operated with a variety of fuel supply systems. Since, however, the experiments were performed using propane which is a gaseous fuel, no special fuel injection system was required. The fuel was introduced continuously through an orifice 5 cm away from the inlet valve seat and it was metered using a manually operated valve.

2.2. The Head Gasket Ionization Probe

The head gasket used in our experiments was manufactured in MIT using standard printed circuit board techniques [7]. As shown in Fig.2.1 this particular probe has eight electrodes equally spaced around the circumference of the cylinder bore. The circuit pattern was etched on the one side of the double sided copper-clad board, while the other side was left intact and

was used as a ground connection to the cylinder liner. The circuit on top was isolated from the cylinder head using a thin sheet of teflon. The eight ionization probes are flush with the cylinder liner. Their width is 3 mm (approximately) and their thickness is 1.5 mm. The circuit on the gasket top was insulated from the cylinder head using a thin sheet of teflon making the cylinder head a second ground connection. The electrodes of the probe were biased by the biasing circuit to around 200 V and they are fit flush with the surface of the cylinder liner. The signal conditioning circuit amplified the signal through an adjustable gain. The output voltage ranged between -15 and 15 volts. The location of the probe relative to the other cylinder head parts is shown in Fig. 2.2

2.3. Verification Experiments

After the model described in chapter 4 was formulated, it was necessary to test whether its predictions were accurate enough to use them with confidence in further investigations. For this reason a set of verification experiments was run. In these experiments two more ionization probes were installed on the cylinder head. They consisted of two 0.8 mm diameter type K thermocouple wires (one used as a ground) insulated from the cylinder head by a ceramic tube. The wires protruded about 2mm into the combustion chamber. The location of the probes is shown in Fig. 2.3. In addition to the two probes the fibre optic instrumented spark plug was located in the place of the pressure transducer. The spark plug was used as an ionization probe and as an optical probe, thus giving two arrival times of the flame as the two different diagnostics would perceive it. The above spark plug has actually eight windows equally spaced around its circumference (1 cm diameter). The optical arrival time was taken to be the average of the eight arrival times.

2.4. The Fast Response F.I.D.

The fast response Flame Ionization Detector allows the hydrocarbon emission signature of a single cycle to be recorded for the whole of its duration owing to its high frequency

response. It was used in the final series of experiments performed where the effect of slow burning cycles or more generally conditions with marginal flame development on hydrocarbon emissions was investigated. The exhaust gas was sampled from two locations. Originally it was sampled 15 cm away from the exhaust valve seat. This was the shortest distance at which the hydrocarbon concentration was uniform across the exhaust pipe and hence it could be used in calculating the mass weighted average emissions per cycle. Later on the sampling point was moved much closer to the valve (1 cm) so that the emission profile characteristics could be attributed to the physical processes taking place during the exhaust stroke such as blowdown, piston scraping the quench layer off the cylinder liner and so on. The details of the operation, calculation of delay times, and general set up of the F.I.D. are covered in [6]. Figures 2.4 and 2.5 (from [6]) demonstrate schematically the F.I.D. and the sampling set up for the case when the sample was taken 15 cm away from the exhaust valve seat.

Table 2.1 Ricardo Engine Geometry

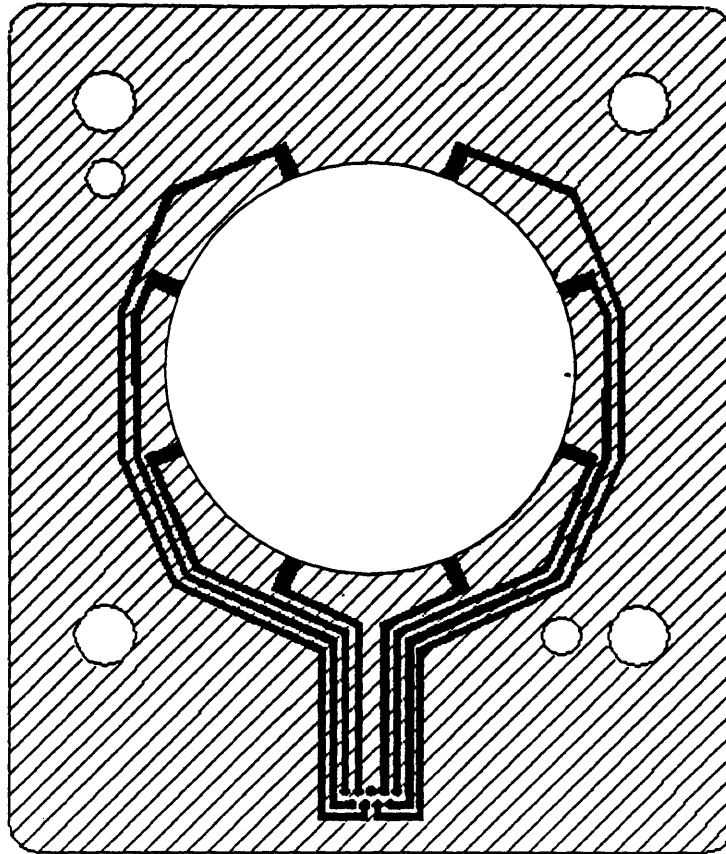
Model:	Ricardo Hydra MK III	
Type:	Single cylinder, iron block and liner (wet), alloy head, two valve, separate overhead cams	
Chamber:	Hemispherical	
Compression ratio:	8.3	
Bore x Stroke:	85.67 mm x 86.00 mm	
Clearance volume:	68 cm ³	
Displacement:	496 cm ³	
Valve timing:	IVO: 4° BTC	IVC: 49° ABC
	EVO: 54° BBC	EVC: 16° ATC

Table 2.2 Flow Room Test Results

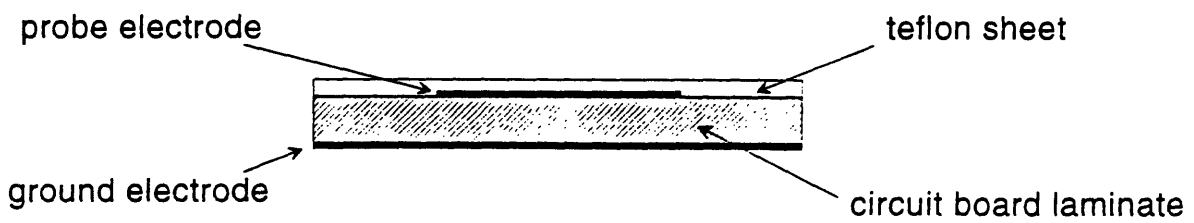
Experiments conducted at 45.7 cm of water pressure drop and 11.4 mm valve lift

Flow characterization	Swirl (Hz)	Tumble (Hz)
Tumble (T)	0	48
Tumble 1 (T1)	0	32
Swirl (S)	22*	19

* Fast-burning swirl is normally above 40 Hz



(a)



(b)

Figure 2.1 Schematic of the ionization probe used in this study. (a) shows the top view and (b) shows a cross-sectional view.

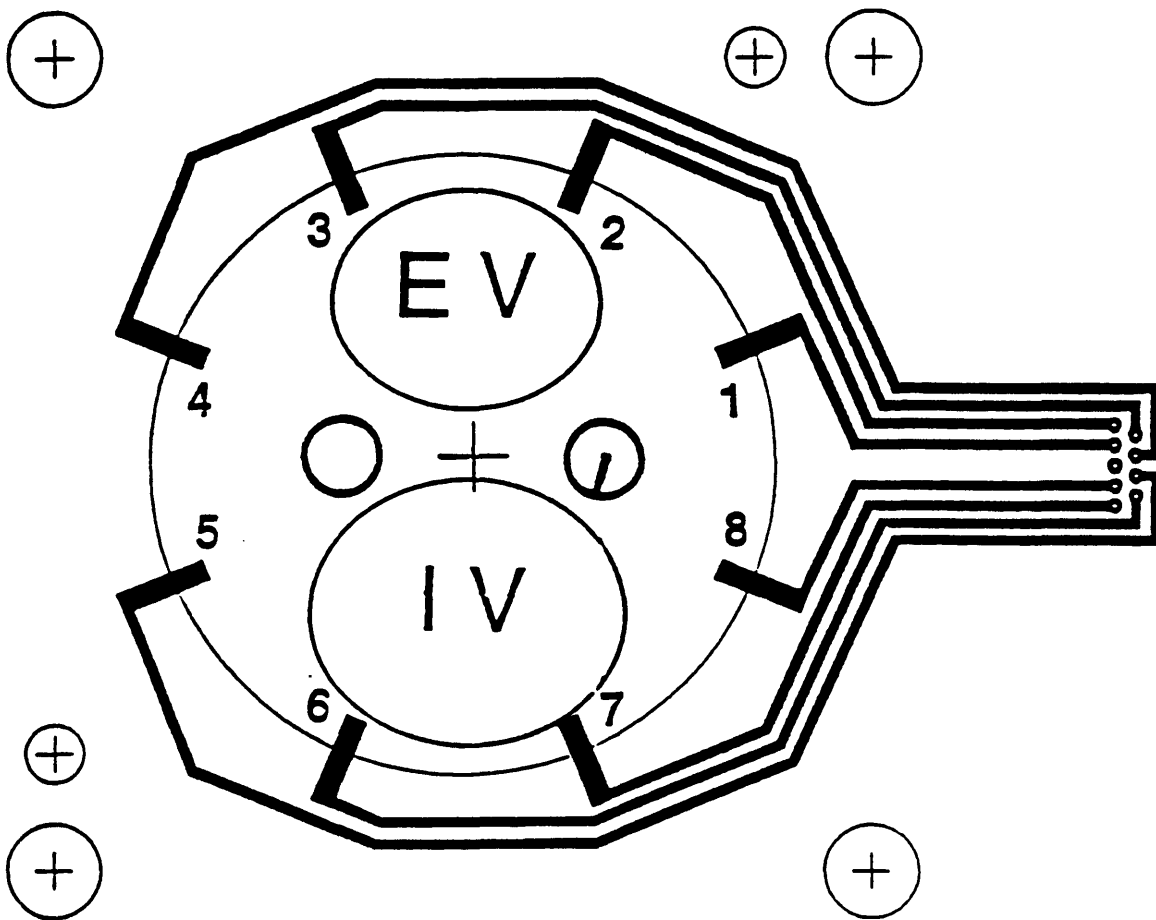


Figure 2.2 Relative (to cylinder head geometry) orientation of the ionization probe electrodes.

Verification experiment set up

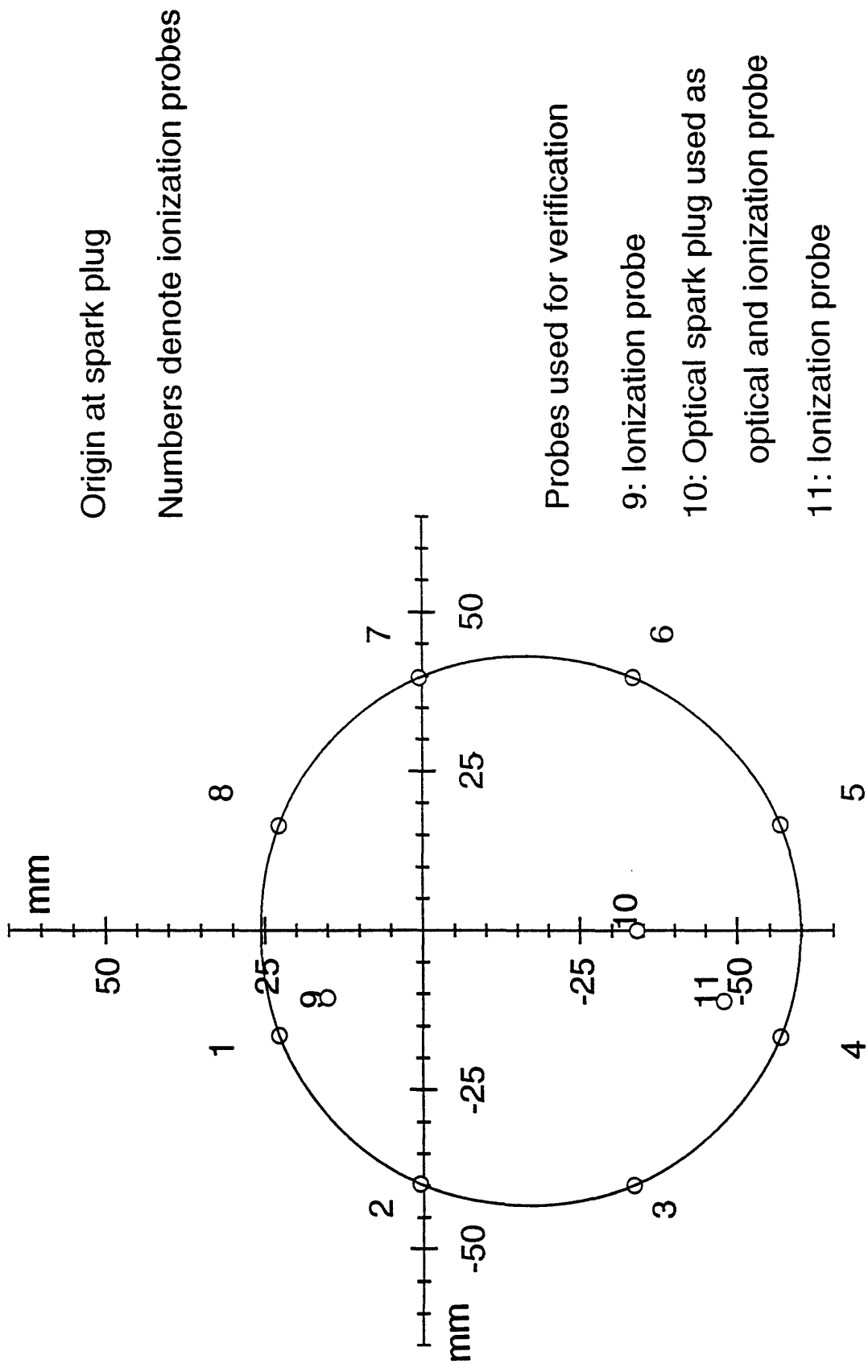


Figure 2.3 Location of the extra ionization probes fitted for the model verification experiments.

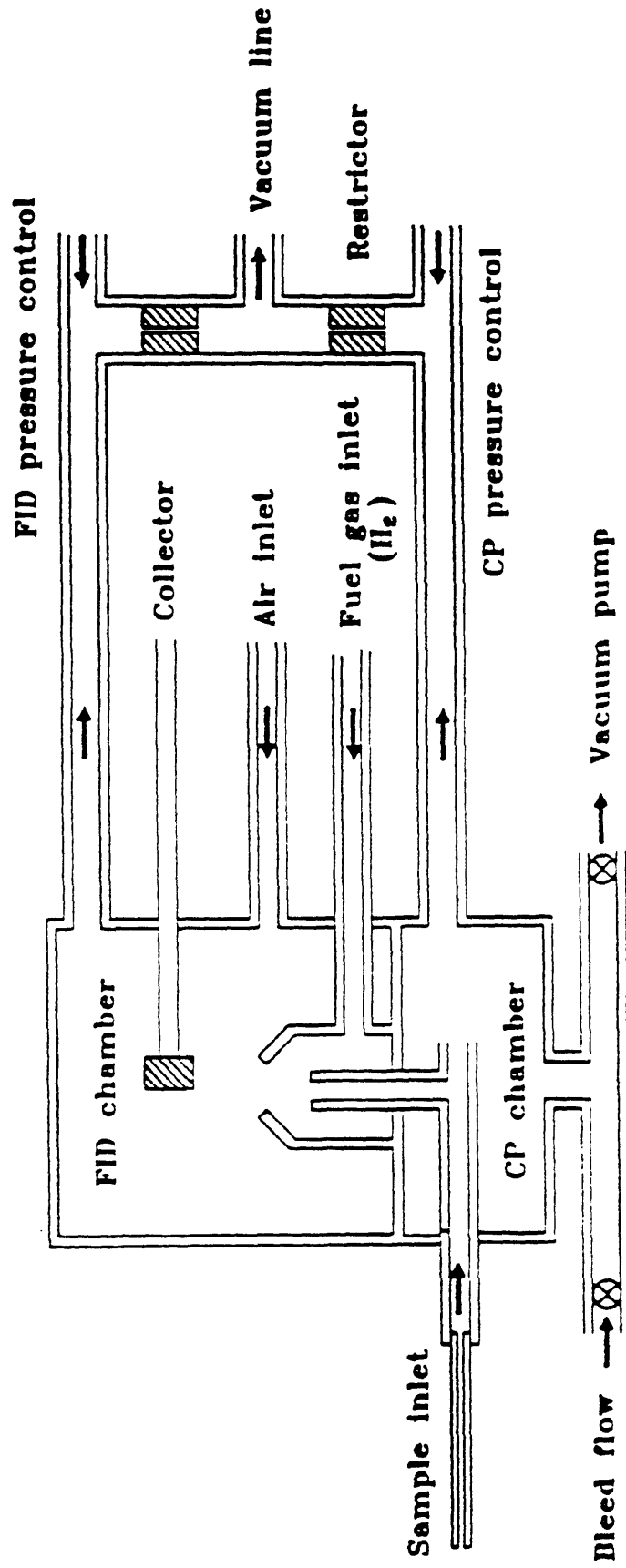


Figure 2.4 Schematic of the Fast Response FID.

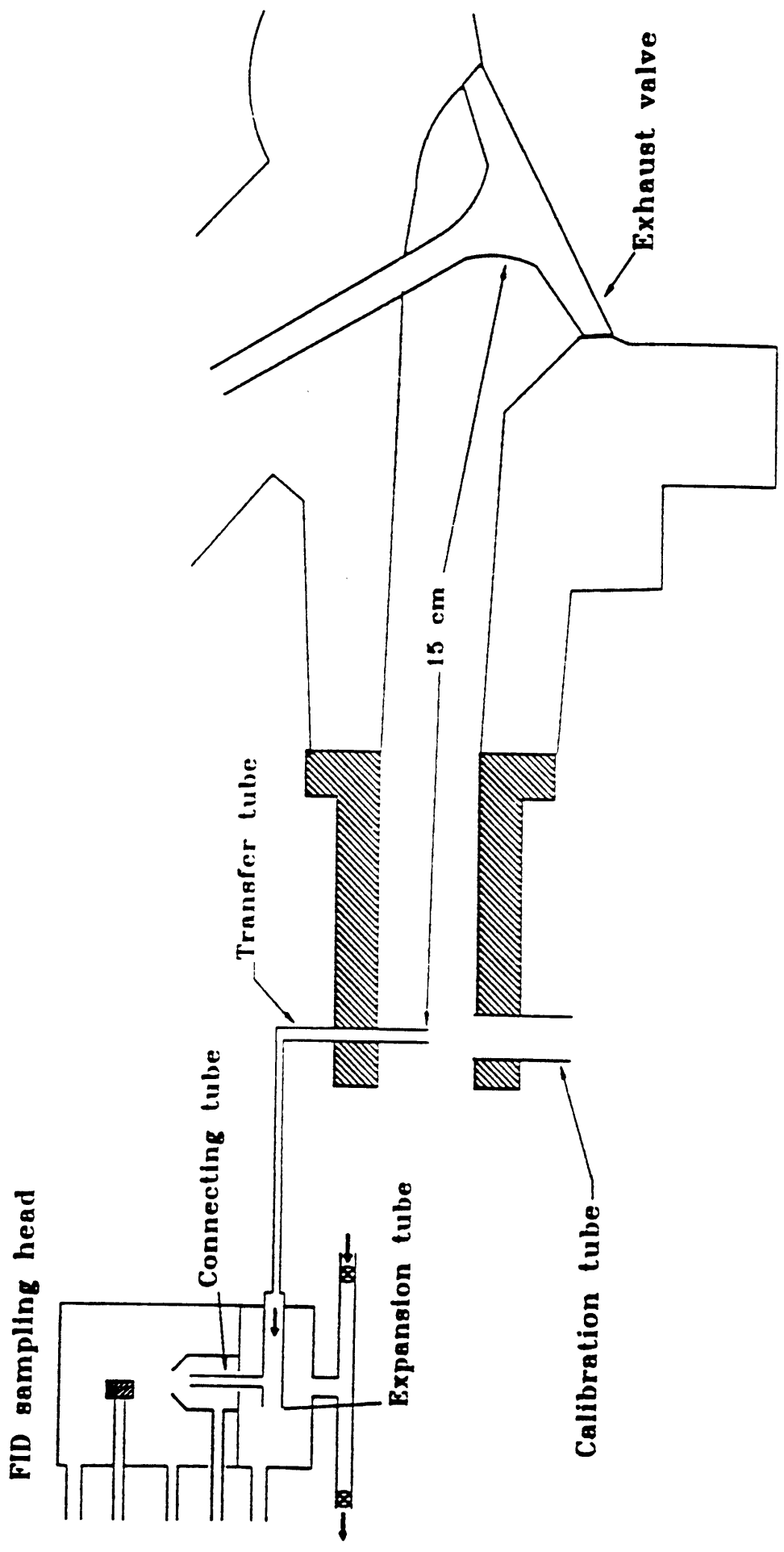


Figure 2.5 Schematic of FR FID sampling at a distance of 15 cm from the exhaust valve seat.

Chapter 3: Data acquisition and processing

3.1. Data Acquisition.

Two data acquisition systems were used. One system recorded the pressure and (later) the F.I.D. signal. For this system a shaft encoder supplied the external clock. The samples were taken every other crankangle degree. The board used was a DT 2828 analog-to-digital (a/d) converter connected to a 386 PC. The second system was working in the time domain, sampling at an aggregate throughput rate of 250 KHz. The board used was a DT 2831 a/d converter connected to a 486 PC. This system was recording the eight ionization probe signals, the pressure trace, and the ignition pulse. The pressure trace was recorded with both acquisition systems as a consistency check. In order to reduce the memory requirements of the second acquisition system, sampling was only effected between 45 degrees BTC and 90 degrees ATC. In the verification experiments the pressure trace was not recorded, but the extra three ionization probes were added and four of the eight optical signals from the optical spark plug were also recorded.

3.2. Signal Processing

3.2.1 Ionization probe signals

Fig. 3.1 shows an example of the signal from an ionization probe representative of stoichiometric operation at 1600 or 2500 rpm. When, however, the engine is running lean the signal strength is reduced and the rise is not always as sharp as in the example above. In addition, the signals vary from probe to probe in shape, maximum value and reference value. A digital arrival time of the flame is obtained when the signal exceeds a certain threshold. Hence a consistent way of setting the threshold had to be devised that would not introduce

bias into our measurements. If the threshold is set too low triggering on noise could occur. If the threshold is too high the arrival time is triggered too late and in the case of slow rising signals this delay could lead to an error of up to 50% of the arrival time. For this reason we defined several arrival times as shown in Fig.3.1. $t_{-5\%}$ means the time at which the signal has reached 5% of the difference between the maximum value of the signal and the reference. The same is true for all the times using this notation. In addition to the above, $t_{\text{-noise}}$ was defined by defining a threshold that was above the reference value by 3 standard deviations of the noise of the reference portion of the signal. $t_{\text{-slope}}$ was defined as the time at which the line approximating the slope of the signal during its rise period, intersected the signal. The slope was approximated by connecting the points where the signal has reached its 10% value (as defined above) and its 90% value. In order to determine which was the best choice we plotted the arrival times in the polar diagram shown in Fig.3.2. In this figure the arrival time, as defined by the method of definition under examination, was plotted for every probe electrode in the direction of the probe. The eight points were then connected by a spline to form a contour. We found that the shortest time that would not distort the general time scaling as suggested by the majority of the arrival times was $t_{-10\%}$. As a result the threshold was set for every signal in this way using a Fortran program written for this reason.

3.2.2 Exhaust gas hydrocarbon concentration signals

The output signal from the fast response F.I.D. gives the instantaneous hydrocarbon concentration at the sampling location. This measurement is independent of the mass flow rate and of the exhaust pressure [8,9]. In order to obtain a 'proper' average of the hydrocarbon emissions of a single cycle, the emissions signature has to be mass averaged using the instantaneous exhaust gas mass flow rate. This is calculated using an energy balance on the time varying contents of the cylinder during the blowdown and exhaust stroke, namely:

$$dU = dQ - dW - h \cdot dm$$

where

U = internal energy of the cylinder contents

Q = heat transfer to the cylinder contents

W = work done by the cylinder contents

h_e = enthalpy of gas leaving the cylinder

After some manipulation the instantaneous mass flow rate is obtained:

$$\frac{\dot{m}}{m} = \frac{1}{\gamma} \frac{\dot{p}}{p} + \frac{\dot{V}}{V} - \frac{\gamma - 1}{\gamma} \frac{\dot{Q}}{pV}$$

where \dot{m} is the mass flow rate and

m = total mass in cylinder

p = in-cylinder pressure

V = cylinder (instantaneous) volume

γ = ratio of specific heats

For the heat transfer rate as well as for the variation of the ratio of the specific heats (as a function of temperature) correlations were used [6]. In the calculation for the mass inside the cylinder the residual gas fraction was calculated using the model by Fox [10].

After leaving the cylinder the exhaust gas has to travel for fifteen centimeters before it reaches the probe. The time taken for this and the delay introduced is calculated by integrating the velocity of the exhaust gas by dividing it into small plugs that do not mix between them. It is also assumed that there is no heat loss to the exhaust port wall. It takes 10-20 C.A degrees [6] for the gas to reach the probe. The fast response FID delay is calculated using the program SATFLAP3 [11].

We finally obtain the mass averaged single cycle hydrocarbon emissions:

$$[\overline{HC}] = \frac{\int_{EVO}^{IVO} [HC] m dt}{\int_{EVO}^{IVO} m dt}$$

The time varying hydrocarbon concentration is corrected for all the delays explained above before being integrated.

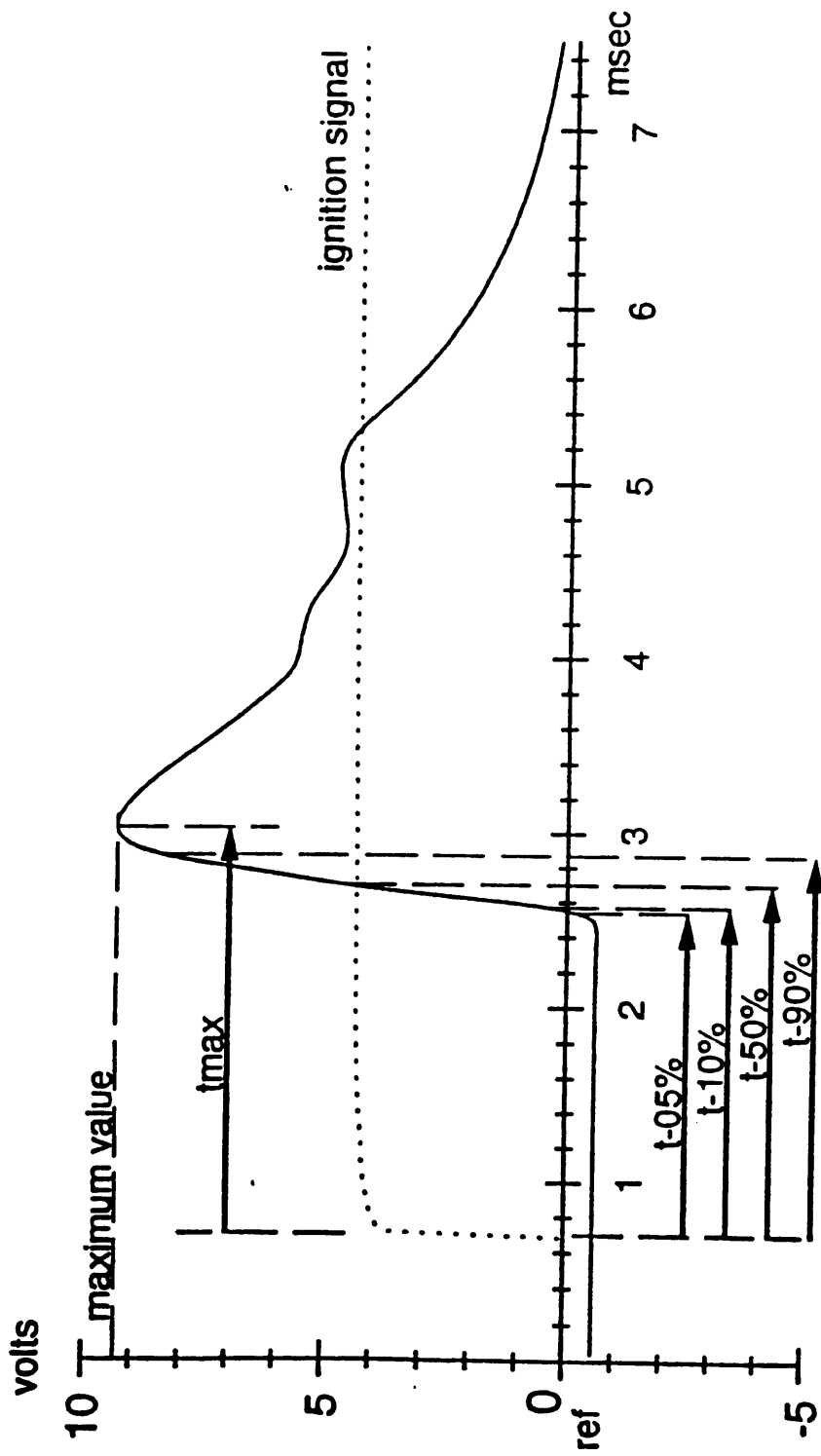


Figure 3.1 Example of ionization probe signal and arrival time definition.

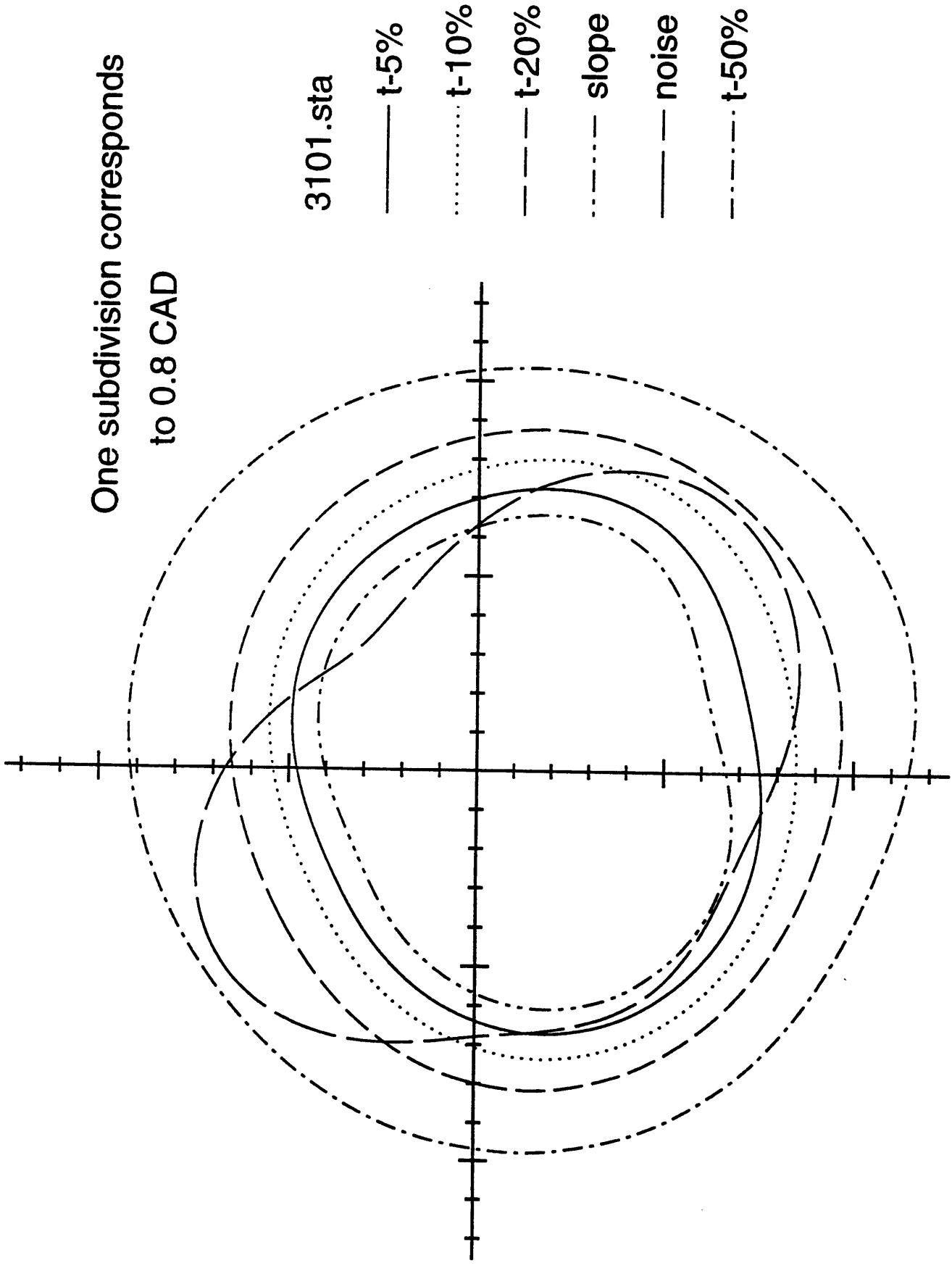


Figure 3.2 Polar diagram of arrival times as defined by setting different thresholds.

Chapter 4: Modelling the flame evolution inside the cylinder

4.1. Background

To draw the flame contours at any given time we have to know how the flame evolves from the point of ignition both in space and time. A model had to be developed that would give the general scaling law for the flame speed or the distance traveled by the flame at any time after ignition. The different approaches to modeling flame propagation in the cylinder of an S.I. engine were recently reviewed in [12]. The modeling approach followed in this work is one which assumes that the flame propagation speed has a given functional form for a given engine. The absolute value of the speed is allowed to vary but the way it scales during the flame propagation process does not change. We have adopted the above modeling approach for two reasons: Firstly, the data obtained from the literature were easily interpretable in terms of the model, facilitating the analysis. Secondly, this requires no further assumptions about the turbulent flame propagation physics.

4.2. Model description

Data from the literature displaying the results of photographic studies of combustion in transparent engines or studies utilizing diagnostics like the ones used here (optical fibers or ionization probes) were used as the basis of the model. Note that ionization probes give flame front arrival times at a specific point in space whereas optical fibers give the location of the leading edge of the enflamed volume in some plane normal to their line of sight, i.e. there is no information about the distance of the flame from the optical fiber windows along its line of sight.

The data available were for three different engines each operated under a variety of different conditions. The first was a Volkswagen engine with a Heron combustion chamber, run at 3000 rpm and relative air/fuel ratios of 1 and 1.3 [13]. The second was an optical access engine run at 600 and 1200 rpm at relative air/fuel ratios of 1.1 and 1.4 [14]. The third engine was again an optical access engine run at 300 rpm with a stoichiometric mixture [15].

It was decided to obtain the flame evolution curve for the above engines, and hence for any engine, by expressing it in the following form:

$$\frac{r}{r_o} = f\left(\frac{t}{t_o}\right) \quad (1)$$

i.e., the distance traveled by the flame in any direction normalized by a known distance r_o is given by a function of the time to travel there normalized by the time t_o taken to travel to r_o . As we show later, this way of specifying the distance traveled by the flame at a given time is equivalent to specifying the normalised speed of the flame (for the whole of burn duration).

Thus the data for the three different engines were plotted and fitted in the form of equation (1) where $f(t/t_o)$ is a polynomial of order 5 in (t/t_o) for each engine. The reference radius r_o was taken to be about in the middle of the distance traveled (25 mm), in order to allow more data to be included in the plots. Note that for the same engine, data in different directions were treated separately but then plotted on the same graph, for example as in Fig. 4.1. This reinforces the assumption that the flame speed is influenced temporally by the changing conditions in the cylinder which are approximately the same for all of the unburned gas. The function f is fitted for every engine as a fifth order polynomial.

Differentiation of the above expression yields the apparent flame speed U :

$$\frac{U}{r_o} = f\left(\frac{t}{t_o}\right)$$

or

$$U \frac{t_o}{r_o} = g\left(\frac{t}{t_o}\right) \quad (2)$$

where in obtaining the second equation we used the fact that $f(t/t_o)$ is a polynomial. Eliminating the time from the above two equations allows us to determine how the apparent flame speed varies during the burn duration.

$$U \frac{t_o}{r_o} = h\left(\frac{r}{r_o}\right) \quad (3)$$

This was done by plotting equation (1) versus equation (2) (treating time as a parameter) and fitting the resulting curve as a fifth order polynomial.

This shows that requiring the distance traveled by the flame to follow equation (1) is equivalent to requiring that the normalized flame speed profiles (as a function of radius) be the same in all the directions although the magnitude of the speed may vary. In other words the scaling relation obeyed by the flame speed during the flame propagation process is fixed for every engine. Specifying the flame arrival time fixes the absolute magnitude of the speed as a function of radius. Equations (1) and (3) allow the flame speed as a function of time to be calculated once it is known as a function of radius.

The normalized distances travelled as a function of time for the three different engines considered are plotted in Fig.4.2. We can see that the flame propagation curves for the three different engines are not the same. Although the phasing of the flame propagation is similar in most engines (to obtain the best compromise between fuel efficiency, emissions, and bmep) the normalised speed varies. This was attributed to the different geometrical characteristics of

the engine cylinder. By taking the geometrical characteristics of every engine into account we expect to arrive to a more general scaling relation (for a quantity related to the flame speed) that holds for every engine. From that relation we could construct the (scaled) flame evolution curve for any engine given its geometrical characteristics. The flame contours can then be drawn given the flame arrival times, as explained above.

Following Beretta et.al. [16] we define the flame as the region delimited by: The flame front where the conditions of flame propagation are met and hence the exothermic reaction is advancing, the flame back where the burning process is completed, and the quench areas where the flame cannot sustain itself because of high heat losses due to contact with the chamber walls, Fig.4.3. The enflamed region is defined as the region behind the flame front. The non-enflamed region is the region that has had no contact with the flame front to the time in question.

The average flame speed over the whole front is defined as:

$$u_f = \frac{I}{\rho_u A_f} \int_{A_f} \rho_u u_f n dA \quad (4)$$

Using a similar definition we can define the (average) gas speed ahead of the flame front u_{gf} .

Then the average speed at which mixture is entrained into the flame is given by:

$$u_e = u_f - u_{gf} \quad (5)$$

In their work, Blizard and Keck [17] and Beretta et al [18] suggested that u_e remains constant during the cycle. More extensive studies by McCuiston et al. [19], Hires et al. [20] and Tabaczynski et al. [21] suggested that u_e varies as a function of the unburned gas density which is a function of the in-cylinder conditions. We argue that since the phasing of the burn event is similar in many spark-ignition engines we can find a way to scale the entrainment

speed against a suitably normalized time. The entrainment speed is also known in the literature as the turbulent flame speed. There have been many attempts to relate it to the laminar burning speed and the local turbulence intensity. Examples can be found in flame speed models [22,23] and recent reviews [24,25] .

A control volume analysis [16] gives the well known result (neglecting piston motion) that:

$$U = \left[\frac{\rho_u}{\rho_b} (1 - y_b) + y_b \right] u_e \quad (6)$$

where u_e is the entrainment speed, y_b is the volume fraction burned and ρ_u and ρ_b are the unburned and burned gas densities, respectively. The entrainment speed is the velocity with which the flame advances relative to the unburned gas ahead of it. The volume fraction burned can be calculated as a function of r/r_o for any combustion chamber geometry. In order for the above calculation to yield a result depending on r only we had to assume that the flame propagates spherically from the point of ignition. Introducing more parameters would not increase the accuracy of the calculations in a significant way. By using the fact that $\rho_u / \rho_b \cong 4$ we can calculate how the ratio U/u_e varies as a function of r/r_o :

$$\frac{U}{u_e} = w\left(\frac{r}{r_o}\right) \quad (7)$$

Equation (7) is a polynomial fit of order 3. A higher order fit was not necessary since the curve is very smooth (an example is given in Fig. 4.4).

Using equations (6) and (7) we obtain:

$$u_e \frac{t_o}{r_o} = h\left(\frac{r}{r_o}\right) / w\left(\frac{r}{r_o}\right) \quad (8)$$

This implies that the normalized entrainment speed is a function of the radius of the flame and hence the mass fraction enflamed x_f :

$$u_e \frac{t_o}{r_o} = q(x_f) \quad (9)$$

Turbulent flames have a complex internal structure [26,27] and may contain pockets of unburnt gas. As demonstrated by Beretta et al. [16] the mass fraction burned is almost always less than (or at most equal to) the mass fraction enflamed. This is a result of the definition of the flame front, since it takes a finite time for the charge to burn after it has been entrained [17,21]. If we can assume that the effect of this burn up time is small or that it has an almost similar effect in all engines, then we get:

$$u_e \frac{t_o}{r_o} = q(x_b) \quad (10)$$

where x_b is the mass fraction burned. Thus starting from an equation of the form of equation (1) for every engine, we can get an expression for the variation of the entrainment speed as a function of the mass fraction burned, for the given engine.

The results of the above analysis are plotted in Fig. 4.5 (see also appendix). We can see that there is good agreement between the data from the three engines. The physical basis of this modeling approach is that, since the phasing of the burn event is similar for most engines we expect the normalized entrainment speed to be similar for most engines. Thus we can use this scaling relationship and integrate it to produce the equivalent of equation (1) for each specific engine (in our engine the Hydra MK III). The integration constant can be determined by the fact that for t/t_o , r/r_o has to be 1, by definition.

The above analysis gives us the behavior of the flame in the direction of maximum flame travel. In combustion chambers in which the spark plug is not located in the middle of the

chamber the flame reaches the wall at different times. In that case we assume that the flame follows the above velocity profile until it comes close to the wall. The velocity is then made to go to zero in a manner resembling the final flame slow down period in Fig. 4.5. The distance from the wall at which this happens again follows the final slow down period, as shown in Fig. 4.6.

In calculating the enflamed volume as a function of the radius in equation (7) we have made the assumption that the flame grows as a sphere from the ignition point. The flame does not necessarily propagate as a sphere (as we have eight different arrival times in the eight different directions in general). If we need to take deviations from this behavior into account for the calculation of equation (7) we can do that by defining an equivalent spherical flame front being fit to the enflamed volume at any time and defining the radius as an equivalent radius of a sphere having the same volume as the enflamed volume. This will introduce minor changes to the above mentioned calculations (see later). This approximation becomes very good when the model is used to generate average flame contours over a large number of cycles where the resulting average contour is very smooth and almost spherical.

The scaling relation of Fig. 4.5 along with the information about the geometrical shape of an engine's combustion chamber can be used to produce the flame evolution curve of the given engine. This was done for the Ricardo Hydra engine and the results are shown in Fig. 4.7. Using this we can produce the flame contours (given eight arrival times) as follows: The distance of each ionization probe from the spark plug is known and so we know the time the flame has arrived at a particular place, the probe location. Given an r_0 (in our case 25 mm) we can then solve for the time the flame was 25 mm away from the spark plug. So, we can solve for r , the only unknown, at any given time. Thus from eight arrival times, we obtain

eight flame front locations for the same time. These are then smoothly connected by a spline fit to produce the flame contour.

Data from SAE 902126

3000 rpm

lambda 1, 1.3

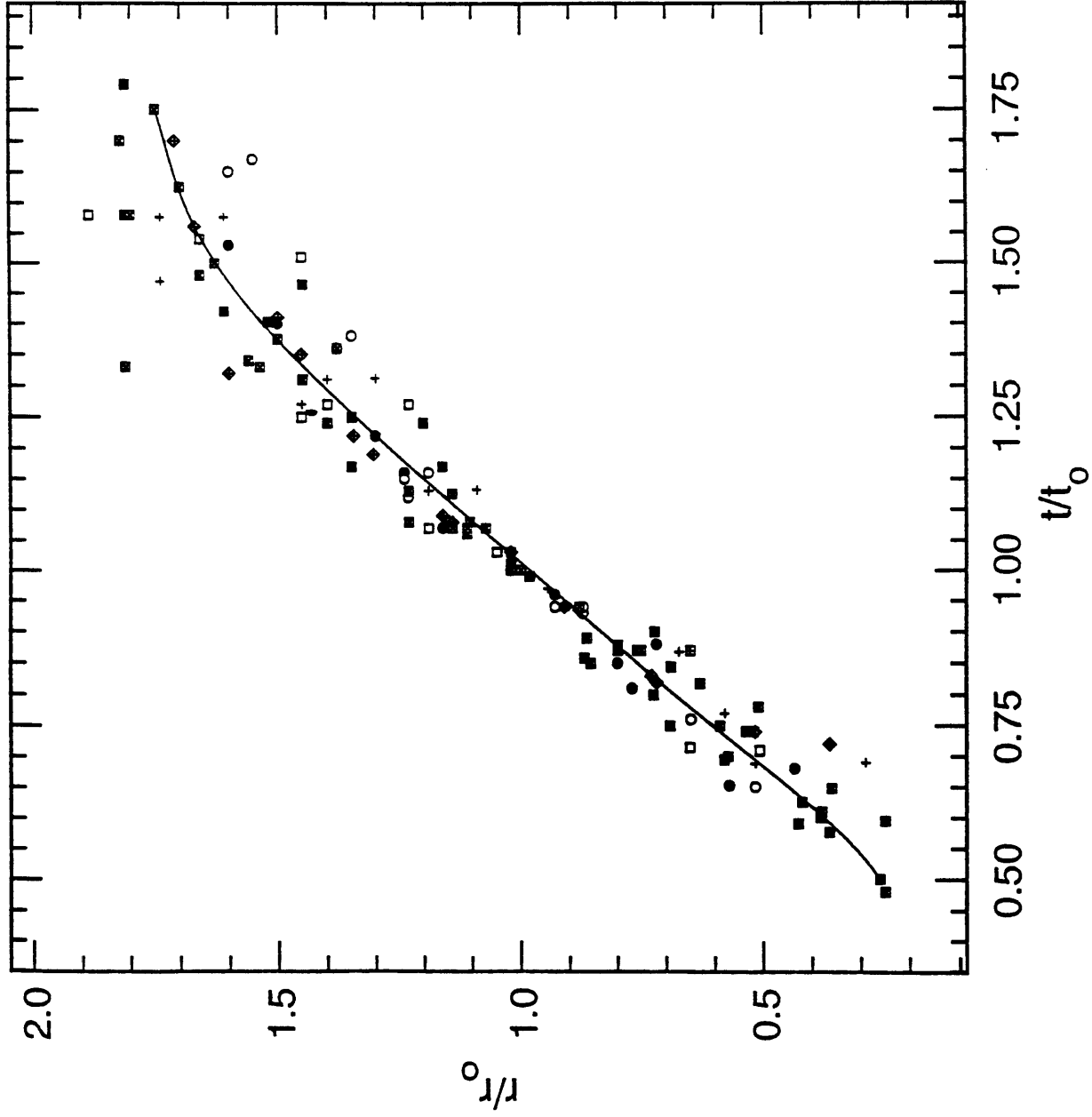


Figure 4.1 Example of data for flame propagation obtained from SAE paper 902126.

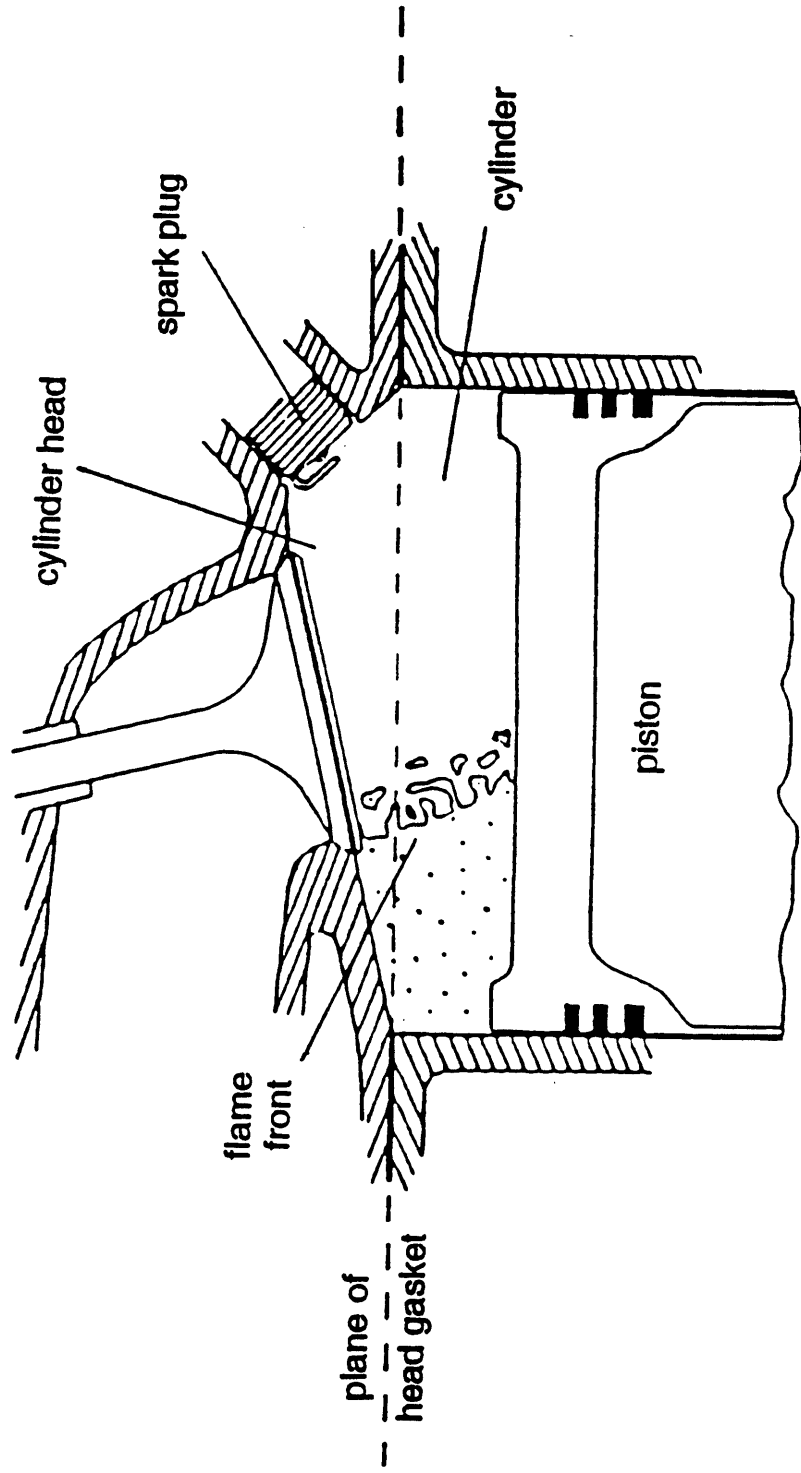


Figure 4.3 Flame Front definition.

- SAE Paper 892098
- ▼ SAE Paper 861531
- ▲ SAE Paper 902126

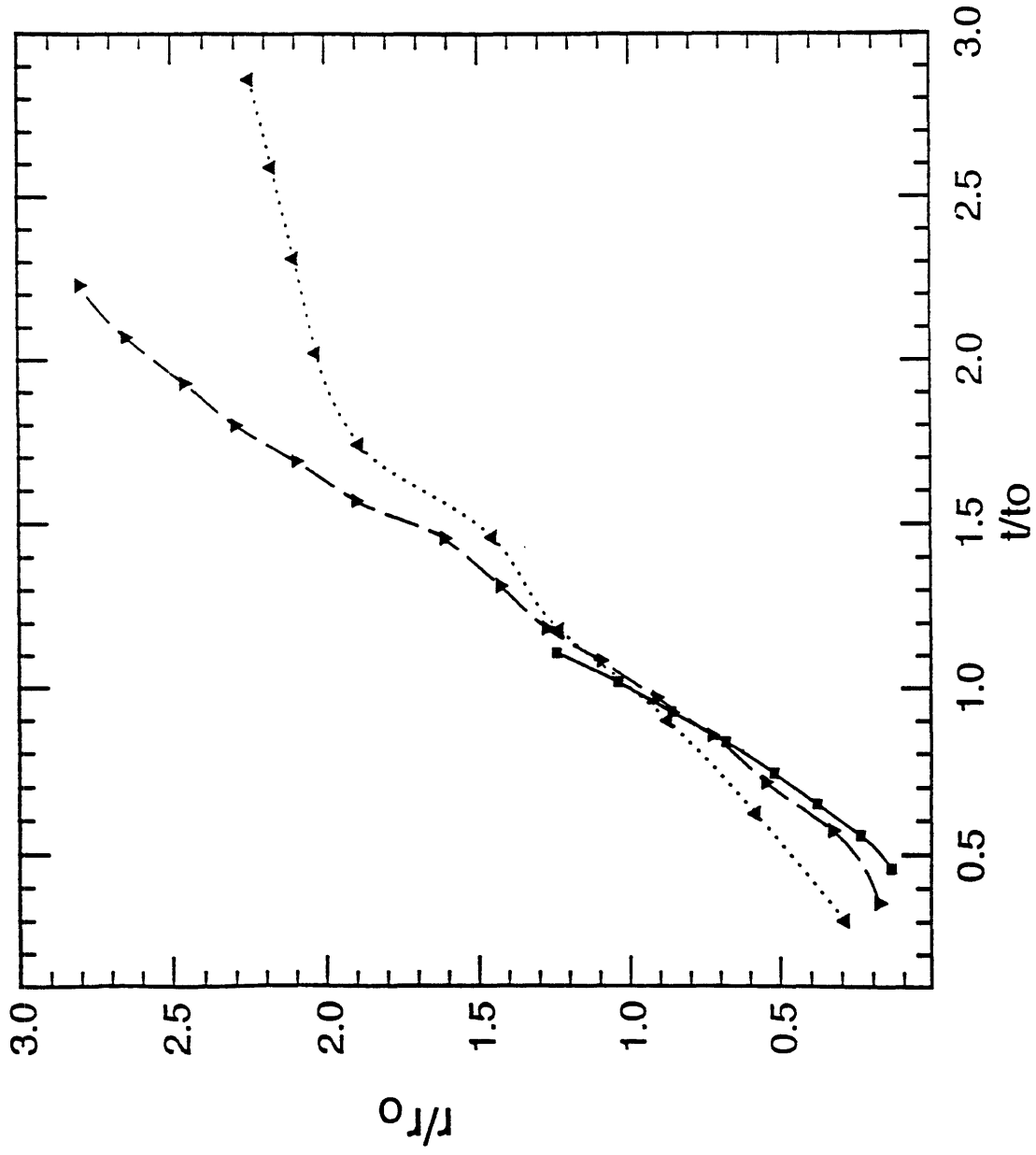


Figure 4.2 Summary of all flame propagation data obtained from the literature.

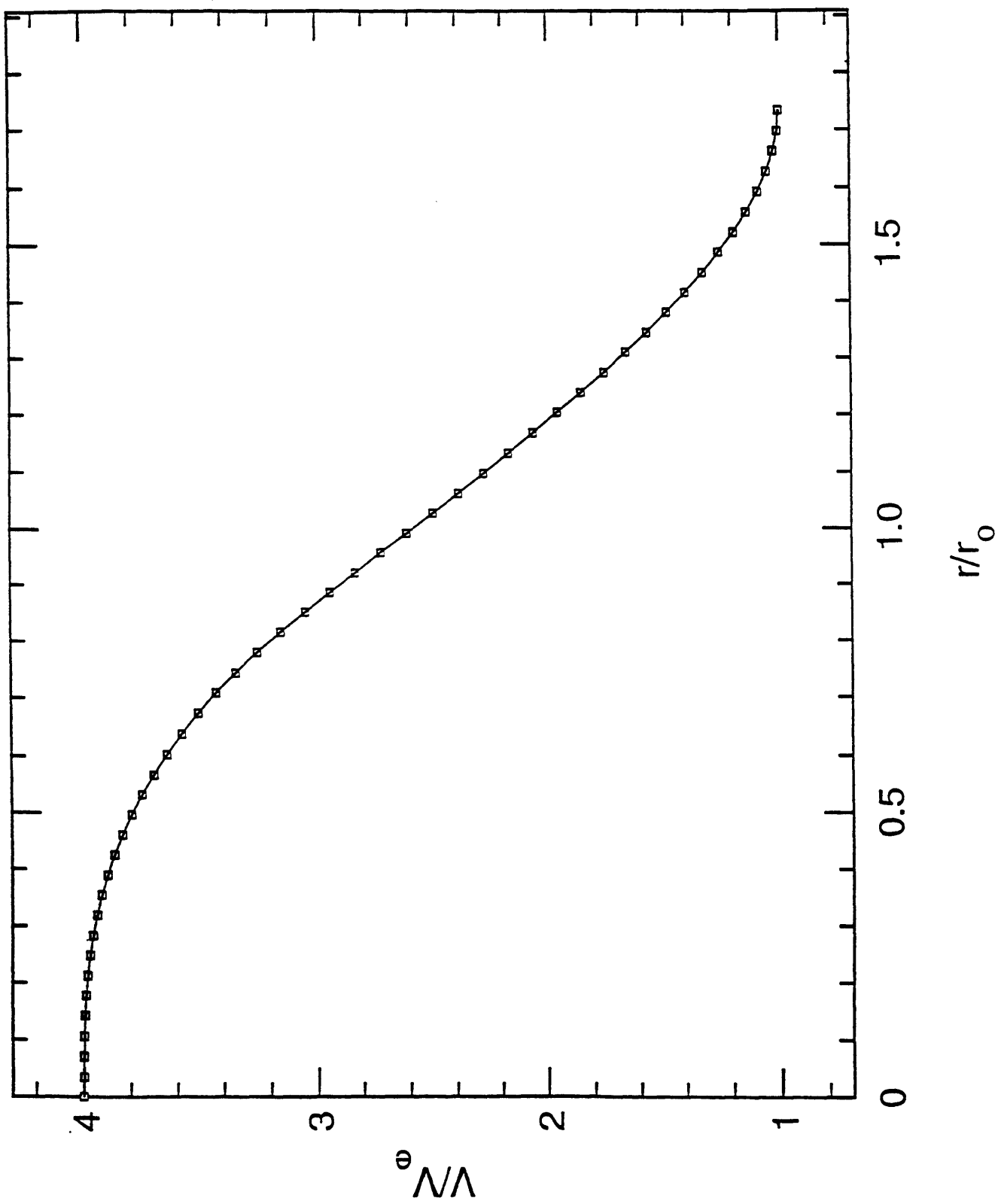


Figure 4.4 Calculation results for the ratio of apparent flame speed to entrainment speed for the Ricardo Hydra MK II.

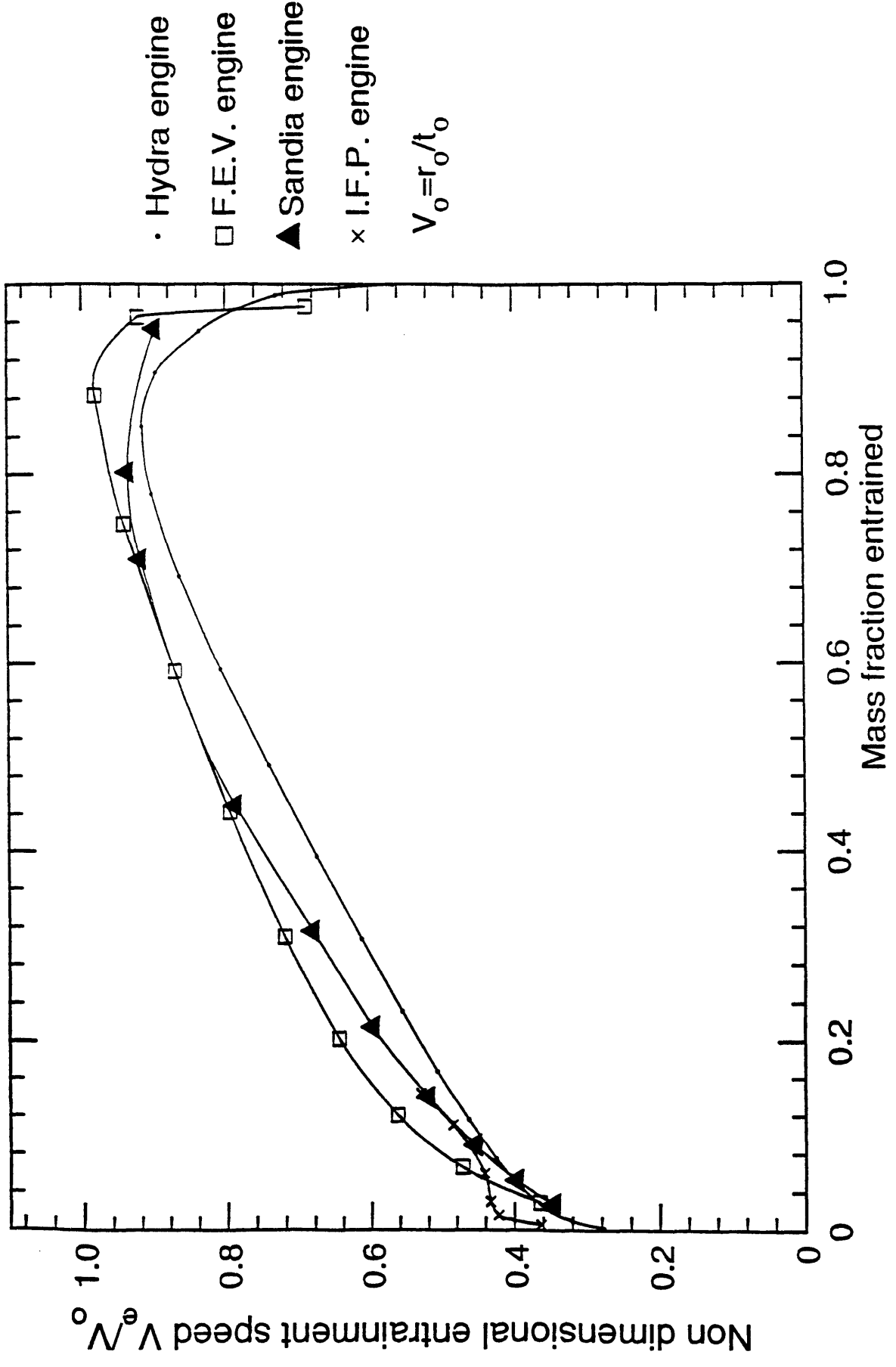


Figure 4.5 Variation of entrainment speed with mass fraction entrained for the three engines analysed and assumed variation for the Ricardo Hydra engine.

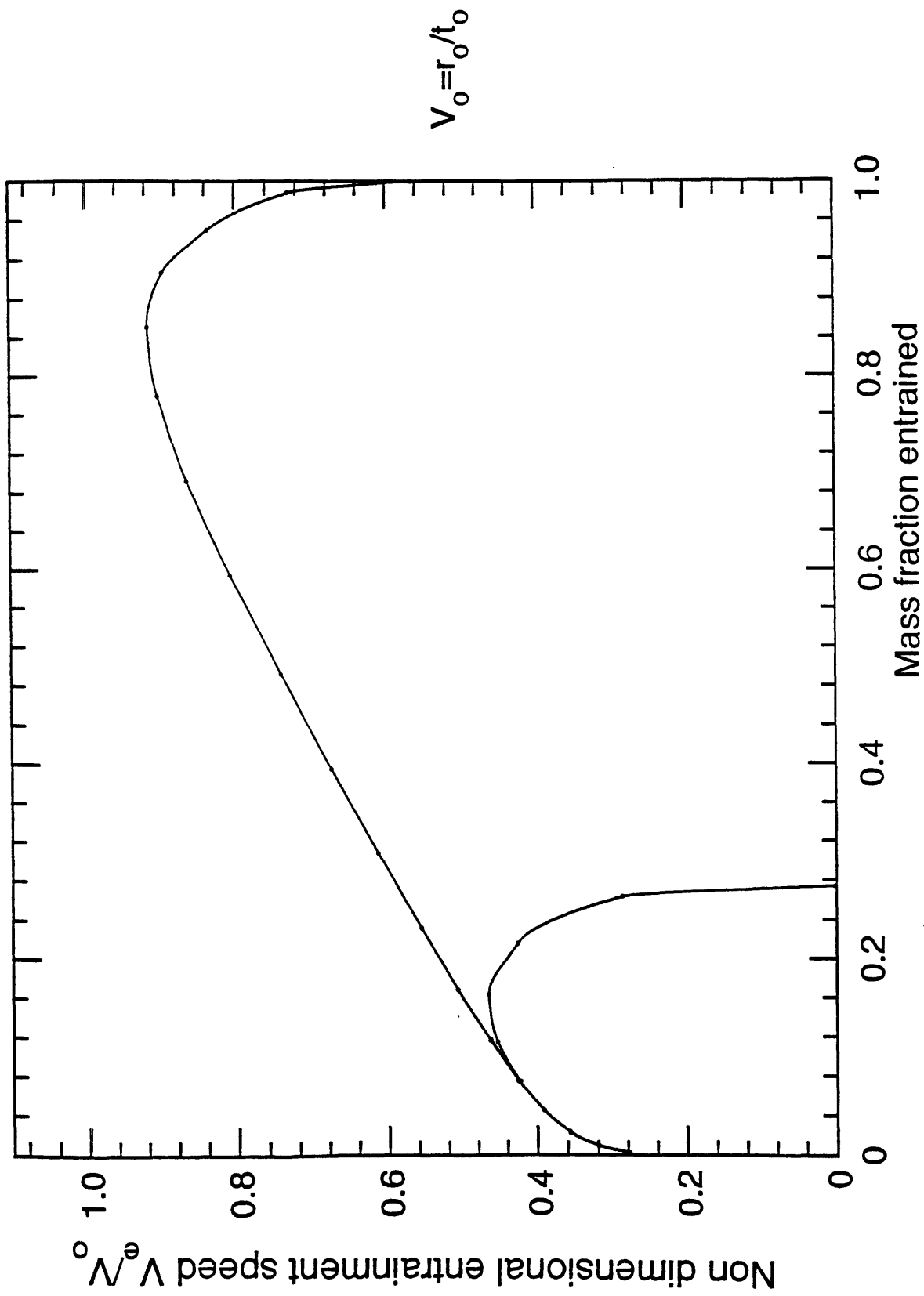


Figure 4.6 Variation of entrainment speed with mass fraction entrained for the Ricardo Hydra engine-Modelling wall effects.

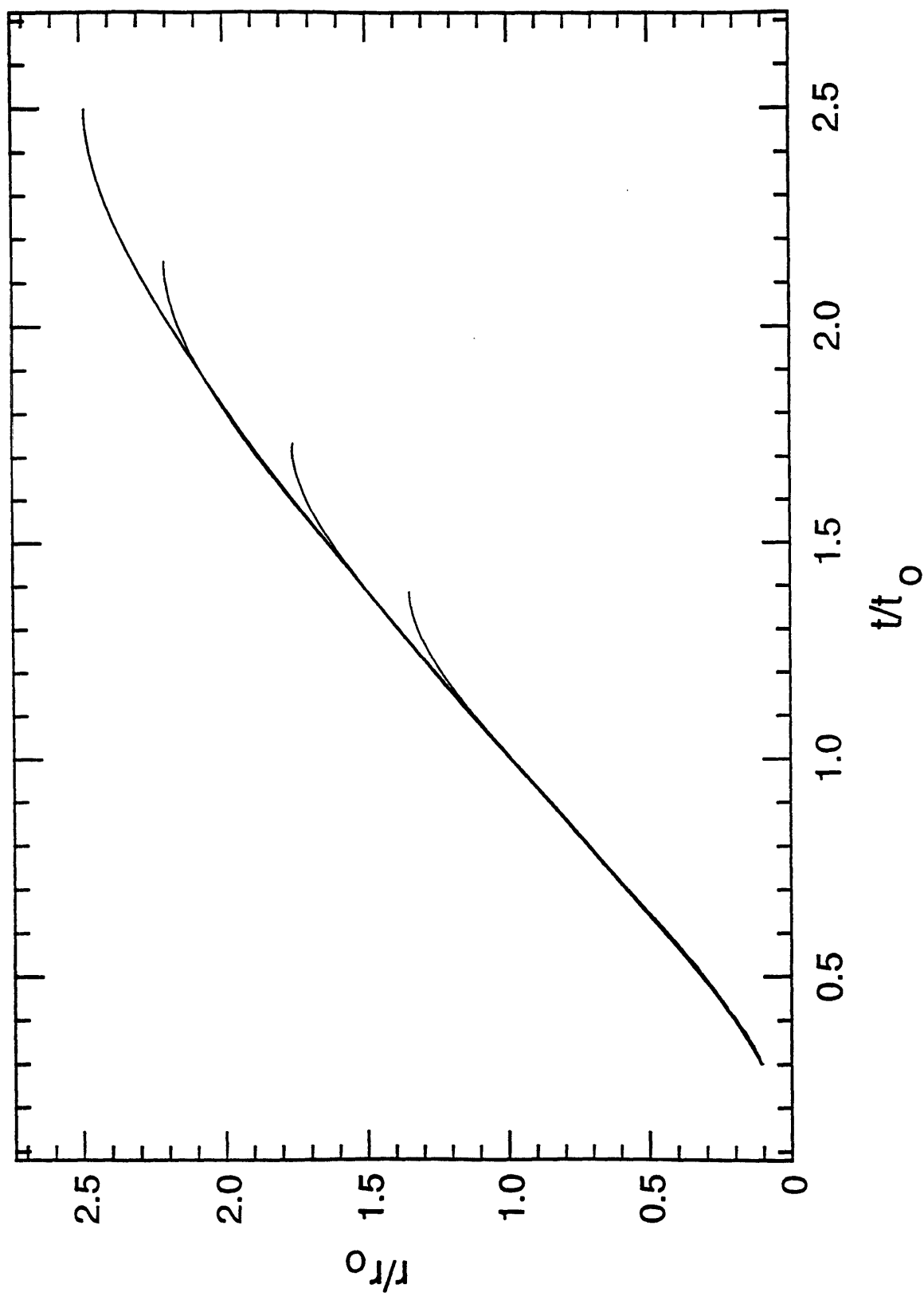


Figure 4.7 Flame evolution profile for the Ricardo Hydra engine.

Chapter 5: Verification experiments

5.1 Method

The experimental set up used to check the accuracy of the flame contour predictions of the model was explained previously. The extra ionization and optical probes installed in the cylinder head give the arrival times of the flame at intermediate points in the combustion chamber. Experiments were carried out for a variety of equivalence ratios and flowfields (see Table 5.1). Note, however, that the model gives the flame radius along the eight lines connecting the spark plug to the eight ionization probes (called lines of propagation). The extra ionization probes are located close to the cylinder head so they detect the flame arrival close to the wall. In general, this is at a different time than the arrival time at a point at the same distance from the spark but along the lines of propagation. Had we tried to estimate when the flame would arrive at the extra probe location we would have had to make an explicit assumption about the effect of the flame slowing down close to the wall. This effect is a result of two phenomena: Firstly quenching at the wall is significant so the flame speed will be slower close to cylinder head. Secondly the gas velocity is smaller close to the wall because of the boundary layer. These two effects result in the flame front close to the wall 'lagging behind' the rest of the flame front. Since we have not modelled these effects, the data are plotted as explained below, without any correction.

5.2. Results

Figure 5.1 shows the physical location of the extra probes (dotted lines) as compared to the predictions of the model at the time the flame arrived at the probe. In order to account for the difference in height between the line of propagation and the location of the probe on the cylinder head, the flame in that direction was taken to have a constant radius in the vertical direction at that point in time. As we can see there is some deviation. This has to be explained by the above arguments regarding flame lagging near the wall, since Fig. 5.2 shows that the optical probe which reports the position of the leading edge of the front (and hence is uninfluenced by the flame lagging close to the wall) is in good agreement with the model. Figure 5.3 shows that the correction required because of this flame lagging scales with the distance of the cylinder head probe from the line of flame propagation.

Another point has to be taken in account. The flame arrival times taken at the head gasket ionization probe are averaged over ensembles of 300-350 cycles. Since the flame is a wrinkled thin reaction sheet, the arrival times obtained correspond not to the leading edge of the flame front but to a contour between the average flame front and the average flame back. Hence the measured arrival of the flame front is slightly later than an arrival time based on the flame's leading edge. As a result the model gives the position of this average contour rather than the leading edge. This has been taken into account when drawing the flame contours for the optical data. Best agreement with the experimental results was obtained when a flame brush half-thickness of 2-3 mm was assumed and the reduction in arrival time because of that was accounted for. In addition, the 10 degree conical angle field of view of the optical probes was taken into account. This required a correction of about 1 mm.

The results were also examined on a cycle-by-cycle basis. The approach was the same; the predicted location was plotted at the time of flame arrival at the test probe. This time, however, a frequency plot was obtained for all of the 350 cycles. Figure 5.4 shows an example of the results obtained. The frequency plot shows that the predicted locations are distributed around the average location used in the results discussed above. The spread is well within the limits of cycle to cycle variation and there is nothing to suggest that the model is not applicable for plotting of single cycle contours.

An additional test for the model would be to check how its predictions of the flame contours vary with engine operating conditions. For example, the standard deviation in the contours should increase when the air/fuel ratio becomes leaner. Figure 5.5 demonstrates this effect. Figure 5.6 shows the rotation of the flow pattern when the flow in the cylinder is made swirling.

We have also checked whether the mass fraction burned as predicted by the enflamed volume was consistent between the different cases, and if it agreed with a separate thermodynamic analysis of the pressure trace, done using a one-zone pressure trace analysis model [28]. The calculation of the mass fraction burned assumed that the flame center remained at the spark plug. Firstly the area of the flame contour under question was calculated. This is simply the projected area of the enflamed volume on the line of flame propagation. The volume enflamed was then taken to be the volume of the sphere centered at the spark plug having the same projected area (on the line of flame propagation) to the area of the contour. A constant ratio of unburned to burned gas densities of 4 was assumed. If the flame contour is very irregular, the above assumption is not valid. However, where mean contours of 350 cycles are examined the approximation is good. The assumption of no

flame center motion then was examined; it was shown that with this assumption the mass fraction calculated was the lower bound. The actual value could be as much as 5% more depending on the distance moved and also on the direction moved. The reason for this is that although the flame contours show that their center is displaced from the spark plug, the motion is in the azimuthal direction thus keeping the distance of their center to the center of the combustion chamber the same as before the distance of spark plug to the center of the combustion chamber. This, because the cylinder head is hemispherical, means that the mass fraction burned does not change. If the center moves towards the center of the cylinder (worst case) the mass fraction burned is bigger because the enflamed region is truncated less by the piston and the cylinder head walls.

The same arguments can be used to correct for the assumptions used in the derivation of equation (6). Unburned fuel inside the flame brush would reduce the mass fraction burned. We noted before that the flame contour lies between the flame front and back but this does not mean that it corresponds to mean mass fraction unburned equal to zero contour. It is rather a geometrical mean, and taking into account the fact that the unburned gas is roughly 4 times as dense as the burned gas, it is obvious that the mean contour may contain net unburned gas. The above two phenomena tend to oppose each other. This may be a reason for the good agreement between the model prediction and the independent thermodynamic analysis. (Fig.5.7). Since then the error associated with the mass fraction of unburned fuel in the mean contour is estimated to be of the order of 5 %, then the unburned fuel in the flame brush is estimated to be about 10 % which is in reasonable agreement with the findings of [16].

Some additional plots were added in Fig.5.8 that demonstrate the cyclic variability inherent in S.I Engine operation. Each flame contour is drawn 10 CAD after the previous one. Closely spaced contours indicate slow flame propagation. In Fig.5.8 we can see that the flame propagates faster in some direction (not always the same) in every cycle and also with very different speeds from cycle to cycle. The operating condition in the examples given is very favorable since the air/fuel ratio is stoichiometric. In chapter 6 similar plots reveal that the cyclic variability increases considerably in marginal combustion situations.

Table 5.1 Verification Experiment Matrix

Operating Condition	Engine speed	Equivalence Ratio	Flowfield
Number			
1-2	900	1	T
3-4	900	1.1	T
5-6	900	1	T1
7-8	900	1.1	T1
9-10	900	1	S
11-12	900	1.1	S
13-14	1600	1	S
15-16	1600	1.25	S
17-18	1600	1	T1
19-20	1600	1.25	T1
21-22	1600	1	T
23-24	1600	1.25	T
25-26	2500	1	T
27-28	2500	1.25	T
29-30	2500	1	T1
31-32	2500	1.25	T1
33-34	2500	1	S
35-36	2500	1.25	S

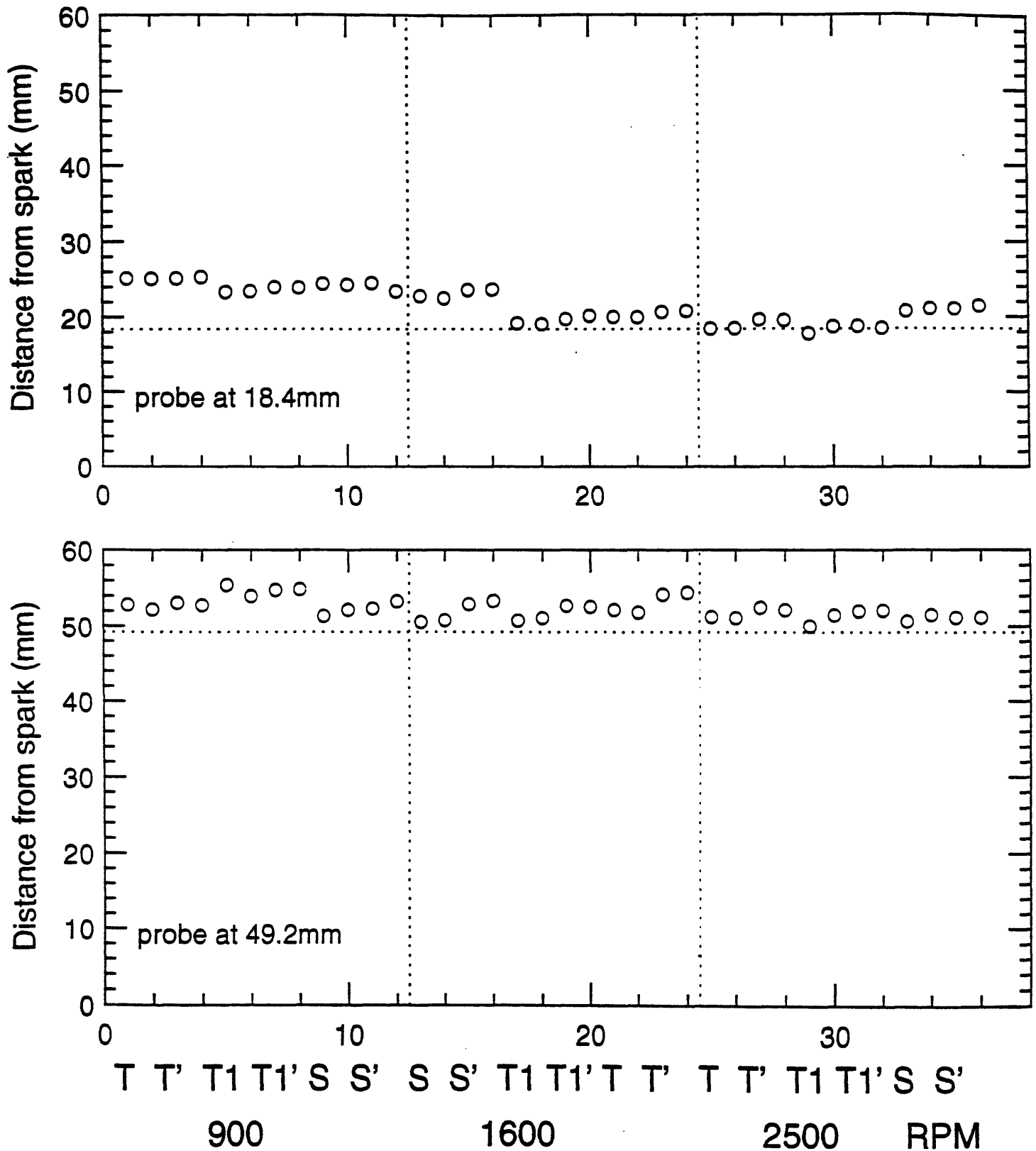


Figure 5.1 Verification experiment results. The predicted flame location (as calculated from the eight arrival times) at the time of arrival of the flame at the two (extra) ionization probes is plotted for 18 different operating conditions. Primes denote lean air/fuel ratio, $\lambda=1.1$ for 900 rpm, $\lambda=1.25$ otherwise. Averages over 350 cycles.

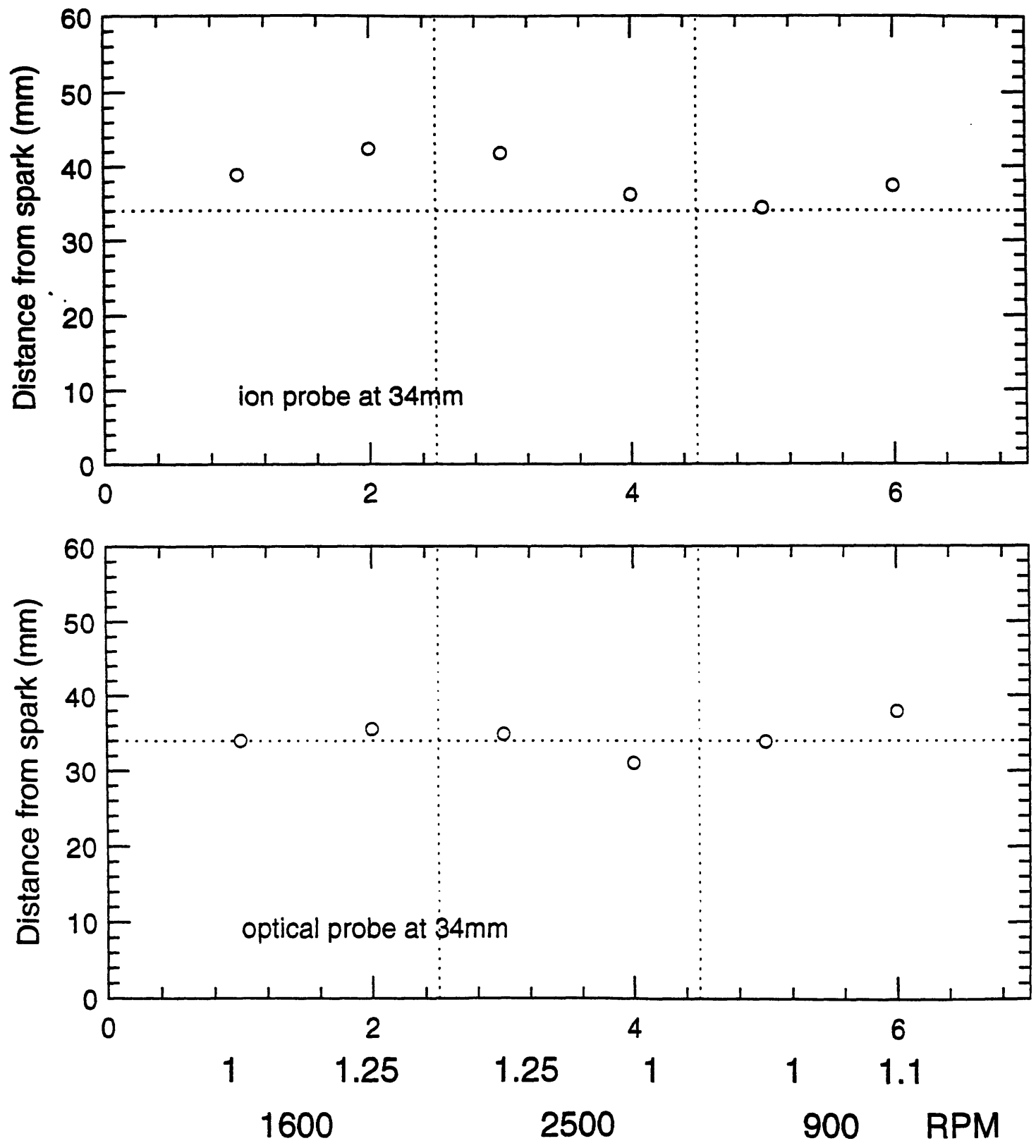
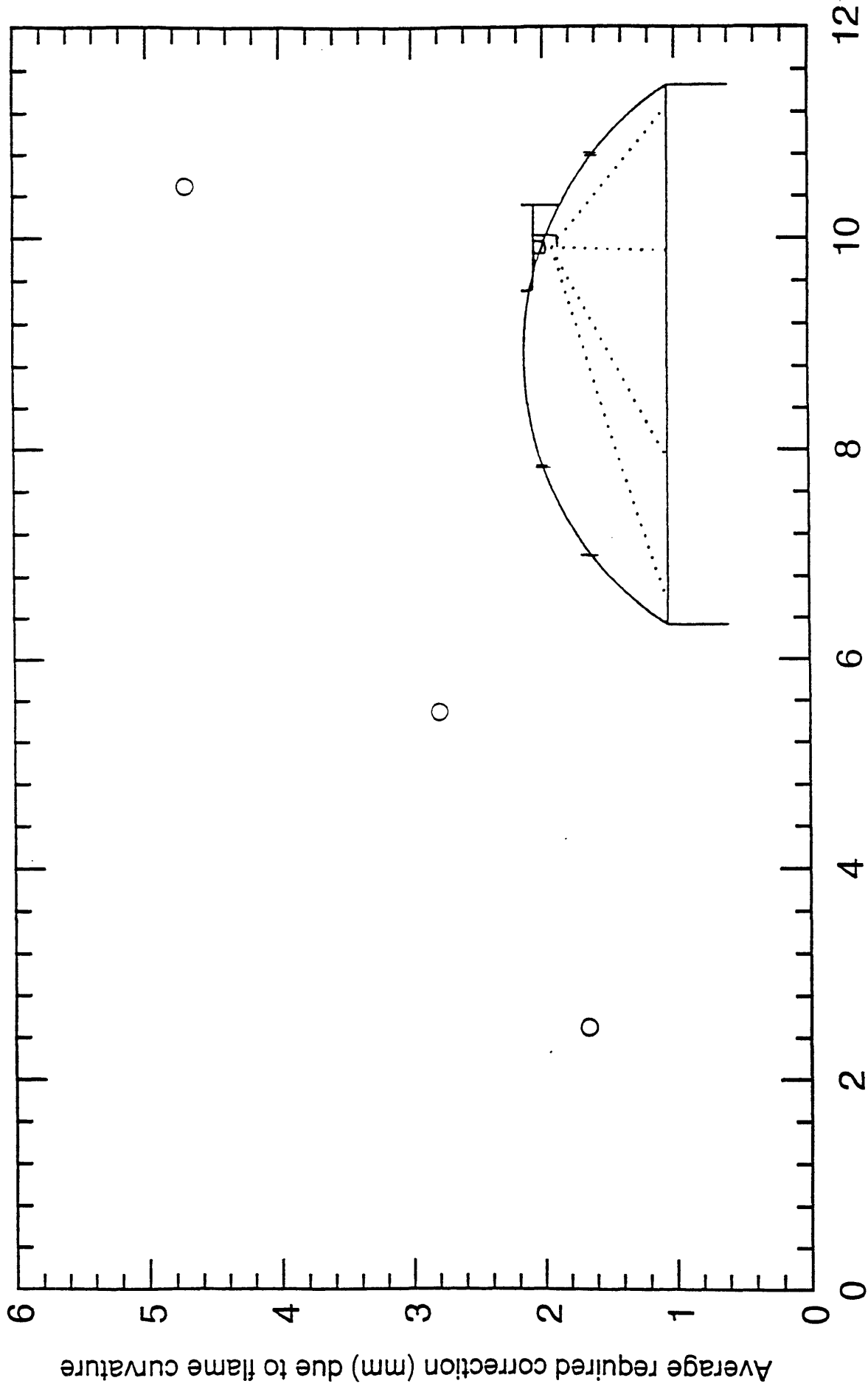


Figure 5.2 Verification experiment results. The predicted flame location (as calculated from the eight arrival times) at the time of arrival of the flame at the optical spark plug is plotted for 6 different operating conditions. Averages over 350 cycles.



Vertical distance (mm) between flame propagation line and ion probe location

Figure 5.3 Correction required resulting from the flame lagging at the wall.

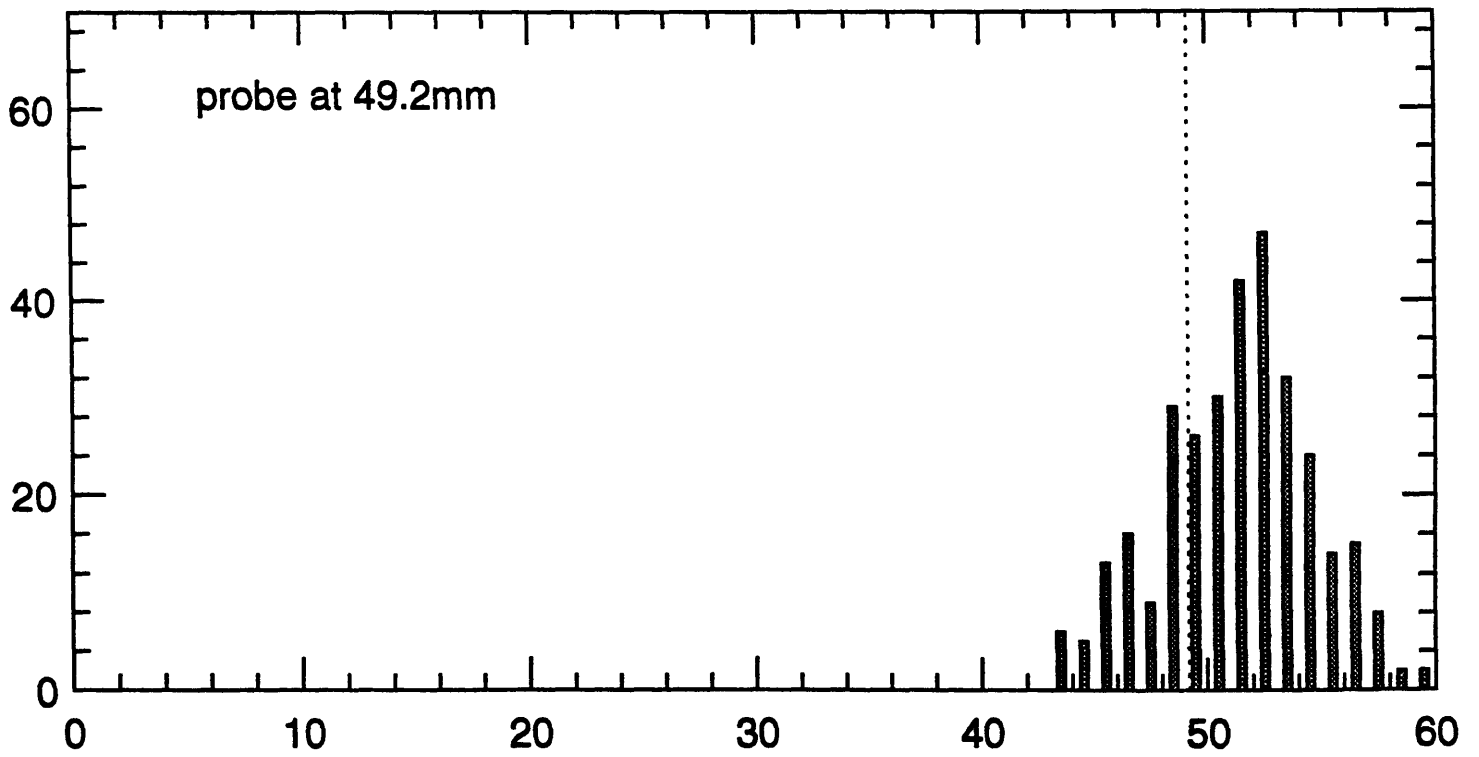
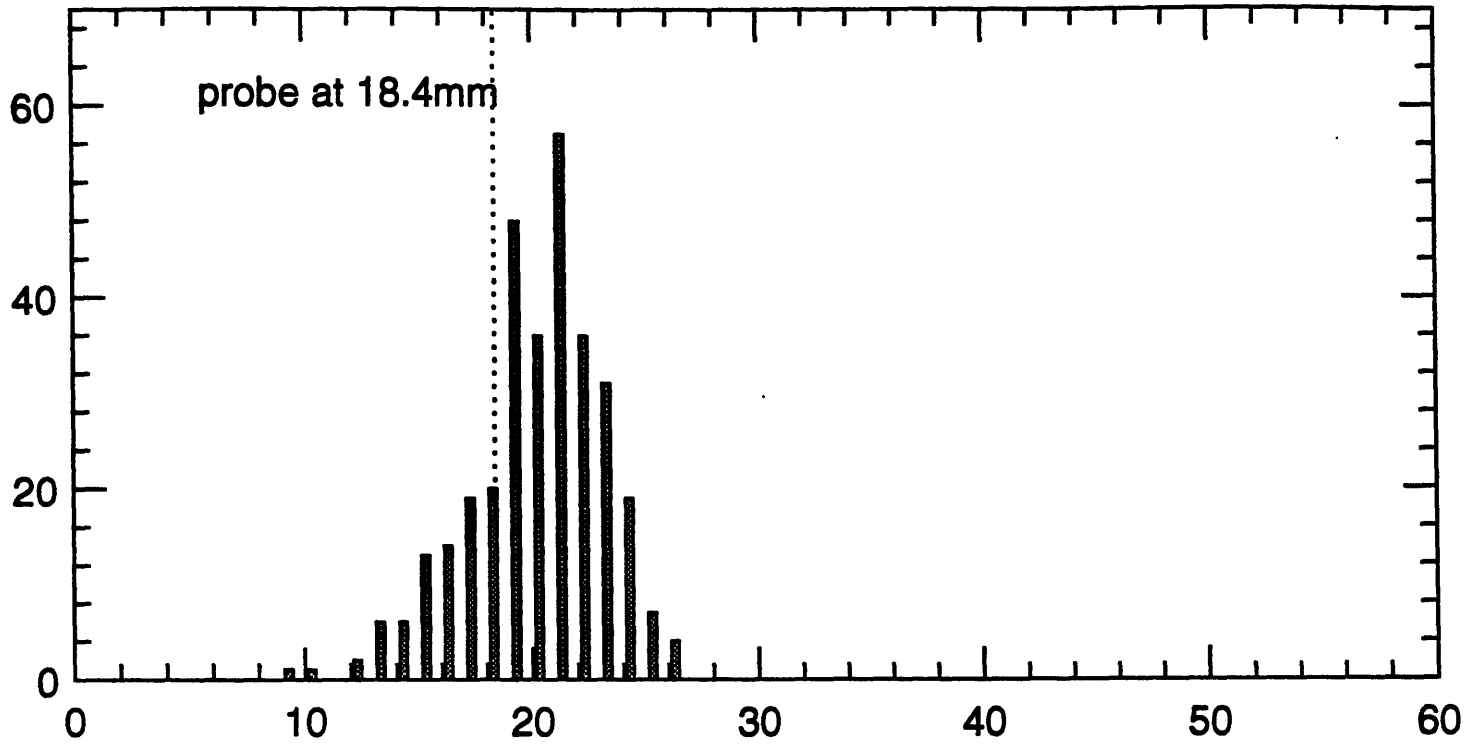


Figure 5.4 Verification experiment results. Frequency plot of one of the operating conditions (2500 rpm, $\lambda=1$, swirling flow).

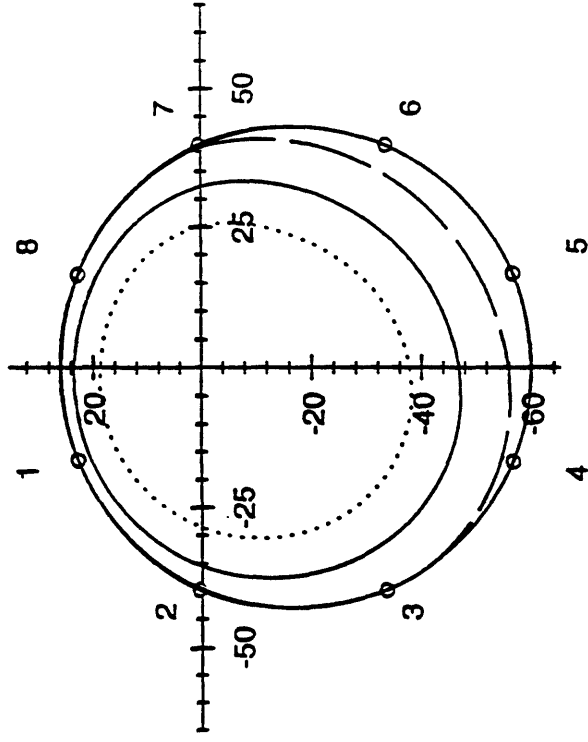
Average results for 300 cycles

1600 rpm, 0.5 bar

Spark adv. 26 CAD

Lambda=1

Quiescent chamber



Origin at spark plug

Numbers denote ionization probes

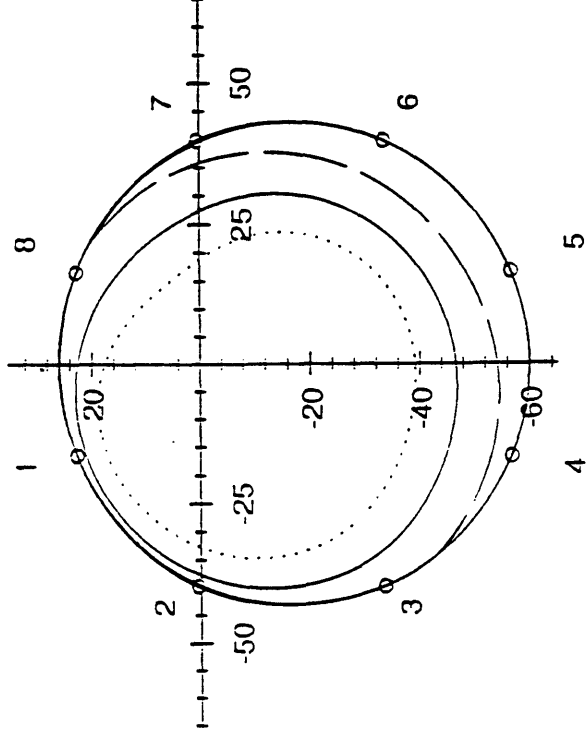
Contours drawn at $X_b=0.5$

1600 rpm, 0.5 bar

Spark adv. 21 CAD

Lambda=1

Swirling flow



..... mean-2 std

—— mean contour

—— mean+2 std

Figure 5.5 Effect of changing the flow field on the flame contours.

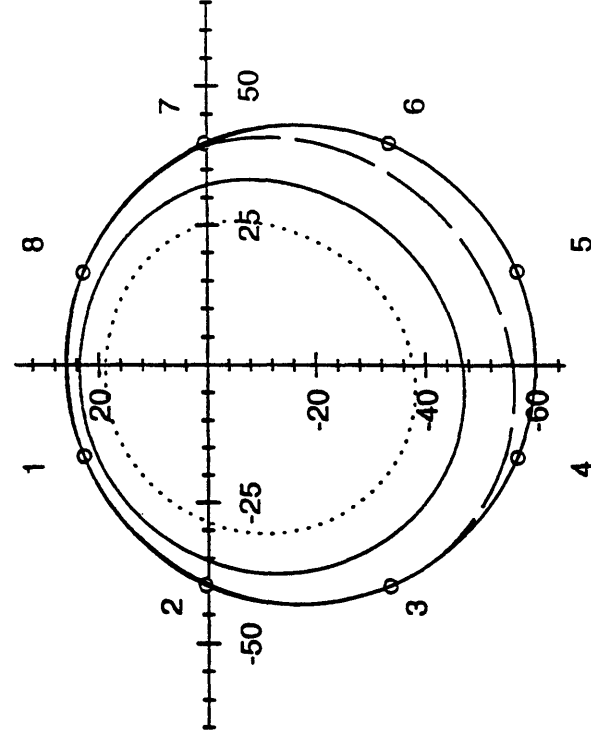
Average results for 300 cycles

1600 rpm, 0.5 bar

Spark adv. 26 CAD

Lambda=1

Quiescent chamber



Origin at spark plug

Numbers denote ionization probes

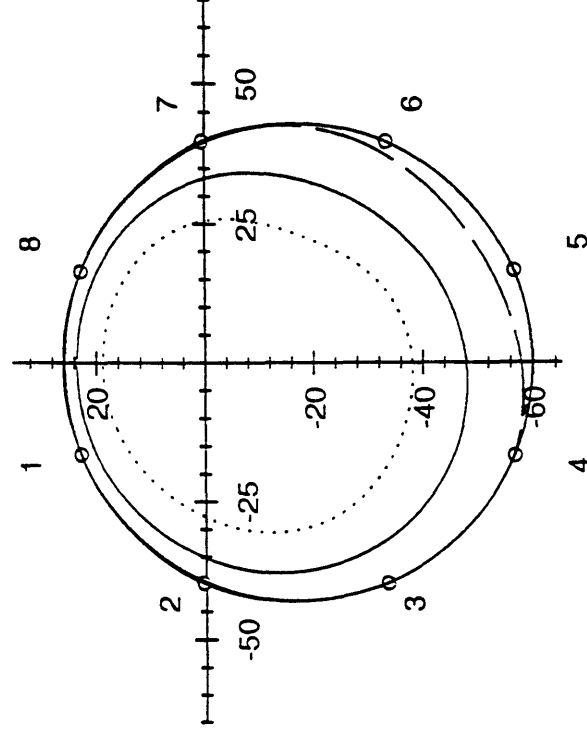
Contours drawn at $X_b=0.5$

1600 rpm, 0.5 bar

Spark adv. 40 CAD

Lambda=1.25

Quiescent chamber



..... mean-2 std

———— mean contour

----- mean+2 std

Figure 5.6 Effect of changing the equivalence ratio on the flame contours.

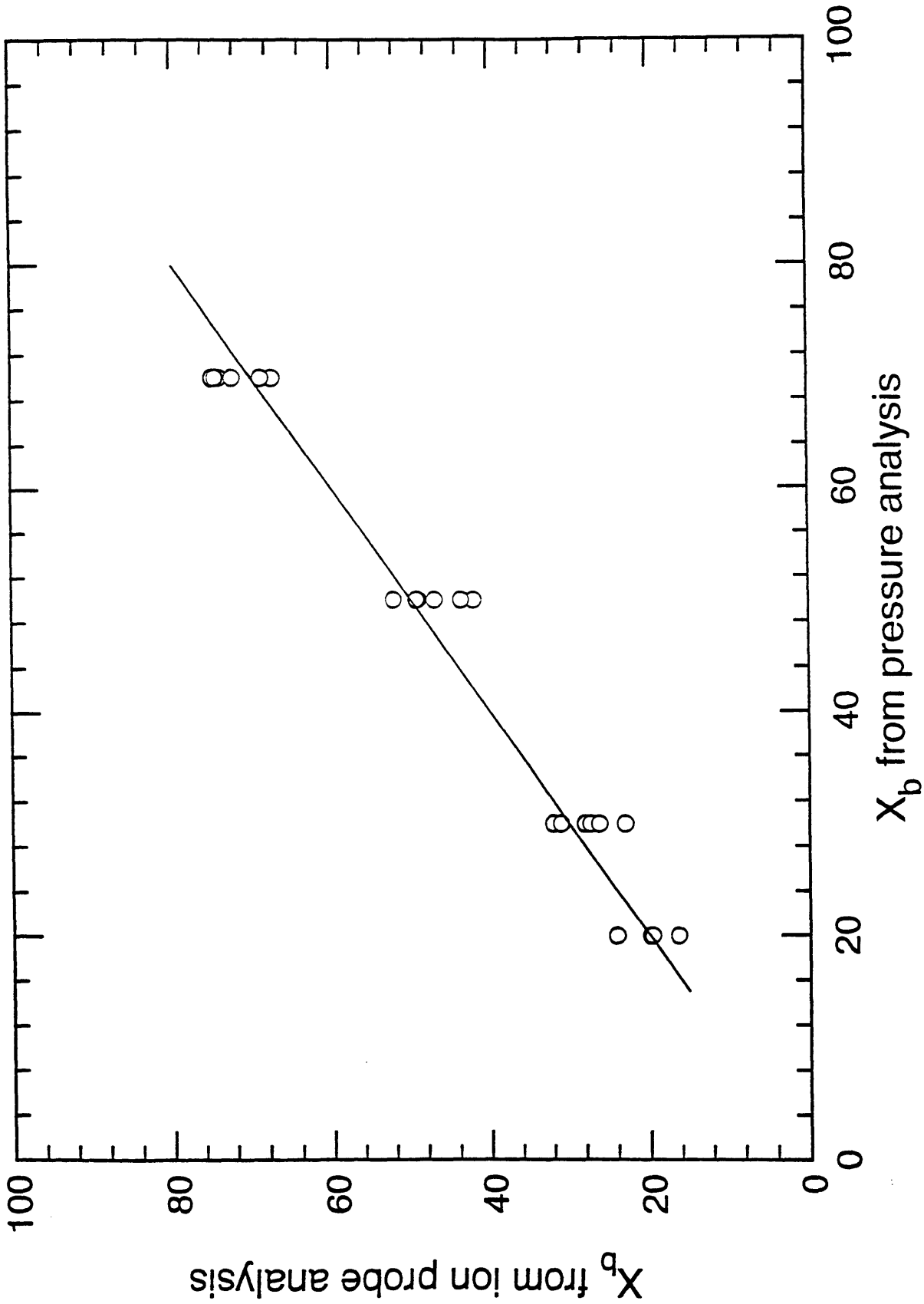


Figure 5.7 Comparison of mass fraction burned as predicted by the model and by an independent pressure trace analysis.

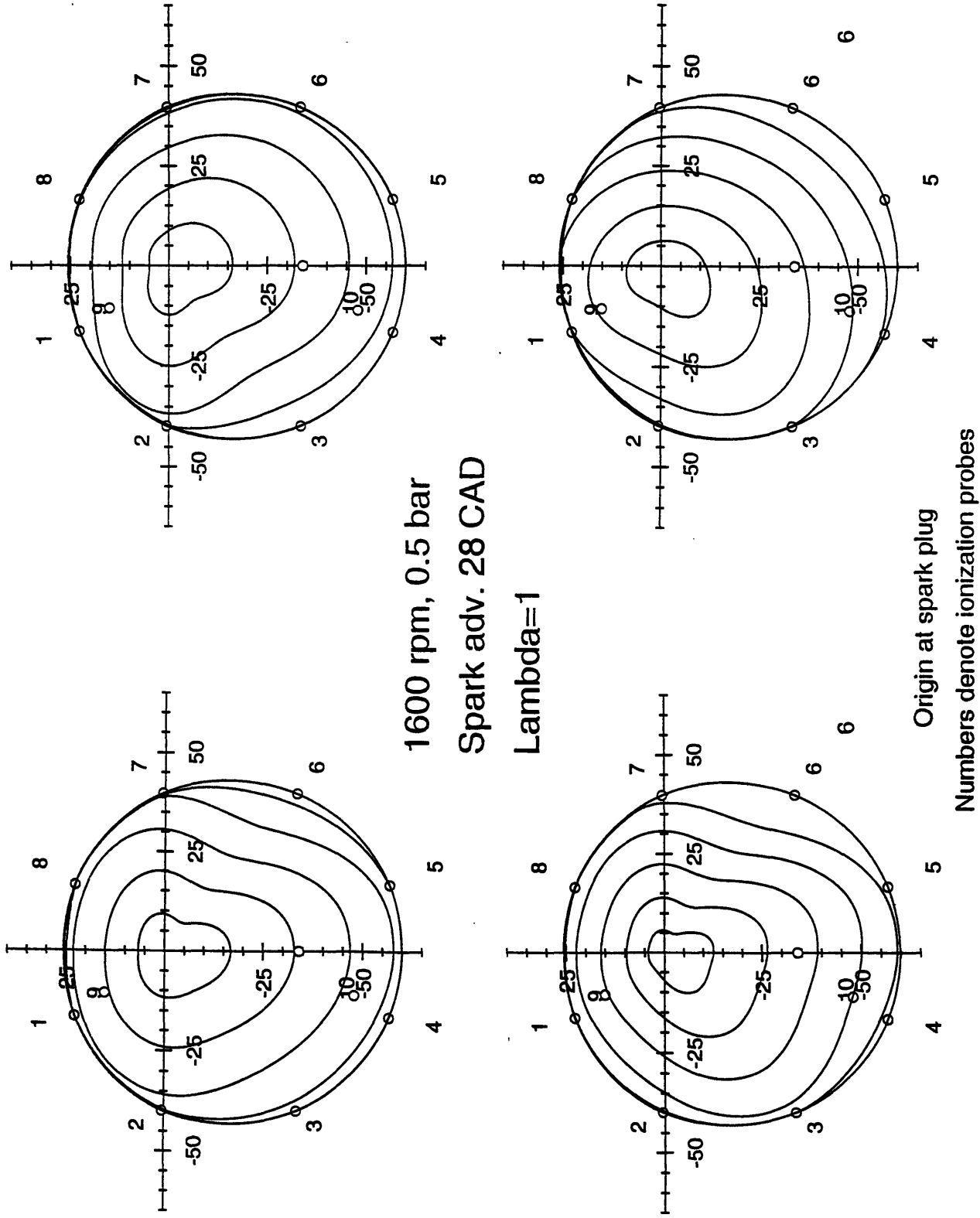


Figure 5.8 Examples of individual cycles demonstrating cyclic variability. Inlet pressure is 0.5 bar and lambda is 1.

Chapter 6: Investigation of poor combustion quality operating conditions

6.1 Background

The objective of this part of the work was to combine the fast response FID with the newly developed ionization probe diagnostic to gain some insight into the relationship between HC emissions and flame propagation characteristics, especially when combustion quality is very poor. It is well known that as the spark timing of an engine is retarded, more charge burns towards the end of the expansion stroke. This means that less work is extracted from it and hence the exhaust gas tends to be hotter. Retarded (by a fair amount) burning, however, also means that more charge escapes combustion (slower burning) and hence the hydrocarbon emissions should increase. The hotter exhaust, however, means that exhaust port oxidation is stronger. Therefore the hydrocarbon emissions of a cycle are dictated by the balance of the above two opposite trends. We are interested to see what happens to this balance when the engine was run fairly lean and whether some new effects are also important in this operating regime.

6.2 Experimental results

As explained in chapter 2 the fast response FID was sampling 15 cm downstream of the exhaust valve and gave us single cycle mass averaged hydrocarbon emissions. At the same time the flame arrival times were recorded and hence the flame contours of all the cycles were available. Experiments were conducted at 1600 and 2500 rpm in the air/fuel ratio ranges 1.25-1.5 and 1.25-1.55 respectively. However, because of the large spark advance required for the 2500 rpm cases (47 CAD) the sampling system did not allow us to take synchronized

simultaneous measurements of hydrocarbon emissions and flame arrival times for this operating condition. The spark timing was always chosen to be the maximum brake torque spark timing. At the lean end of the range the number of misfiring cycles was very large. The engine seemed capable to operate with leaner operating conditions at 2500 than at 1600 rpm. The results are shown in Figs. 6.1-6.4. They show that for λ up to about $\lambda=1.35$ the averaged hydrocarbon emissions are independent of the maximum pressure which is a measure of the burn rate. The hydrocarbon emissions could also be plotted against a measure of the area of the contours of the cycles all plotted at the same time (a given mass fraction burned say) which is another measure of the speed of combustion. Figure 6.5 shows that the maximum pressure and the effective flame radius are well correlated. The effective flame radius is a radius of a circle having the same area as the contours which are all plotted for the same time after ignition. This means that any tendency for the hydrocarbons to increase because of late burning is offset by the increased temperatures during the post flame period and the exhaust stroke. When, however, λ increases to 1.45 we see that the hydrocarbon emissions of slow burning cycles are higher than those of fast burning cycles. When plotted against the cycle imep, the hydrocarbon emissions exhibit the same behavior and the correlation is even more obvious, Fig.6.6. When λ is 1, the variation in imep is very small (stable operating condition) but it is nonetheless uncorellated with the emissions. The proposed explanation for the above behavior is that for the very lean operating conditions the exhaust gases are becoming too cool to be able to contibute significantly in post flame oxidation.

By looking at the above graphs we could see that the different cycles could be grouped according to their behavior into four separate groups or regions (Fig.6.7). In region 1 (Fig.6.8 shows the flame contours from representative cycles) the cycles are ones that we could describe as normal. Some may be slow burning and some fast but none is excessively so. In region 2 we have the cycles which are very slow and consequently have higher emissions but whithin the limits expected from the overall behavior of the dataset. Cycles in region 3, however, have significantly higher emissions while they retain about the same burn rate. The

increase in the emissions is attributed to a partial burn. Figures 6.9 and 6.10 plot the corresponding cycle hydrocarbon emissions. In region 4 the emissions are still high but the cycle has a significantly faster burn. The amount of charge unburned is smaller and presumably more localised (total mass fraction burned = 90%) than for cycles from region 3 (87%). This is probably the reason why cycles from region 3 tend to have their peak in their hydrocarbon emission signature (Fig. 6.10) at the time of blowdown whereas cycles from region 4 with less unburned mixture exhibit peaks during the last stages of the exhaust stroke. In cycles from region 3 slow burning probably continues after the exhaust valve opens and hence they tend to have emissions at the level of cycles from region 4 whereas their IMEP which reflects how usefully the mixture was burned is lower than that of cycles from region 4. This suggests that a fast burning cycle should have higher hydrocarbon emissions than a slow burning cycle having the same mass fraction burned and also lower IMEP. This has actually been observed in some cases. As an example cycle 138 has 3200 ppm C1 and IMEP of 3.3 whereas cycle 97 has 3000 ppm C1 and IMEP of 3.15 while both burned 87% of the charge. Figures 6.11 and 6.12 show cycles from regions 3 and 4 respectively so that the similarity between them can be assessed. Regions 1 and 2 represent regions of 'normal' combustion and cycles within them do not exhibit any distinguishing features apart from normal cyclic variability and a decrease in the burn rate as we move from region 1 to region 2.

As the relative air/fuel ratio becomes larger the number of partial burns (with significant amount of mixture unburned) becomes large. The hydrocarbon emissions for those cycles are very large. At the same time the ionization probe signals start becoming very weak and in some cases impossible to process and obtain digital arrival times from them. In order to assess the possibility of locating the partial burn region we have marked on Fig. 6.11 the cycles for which there was no arrival time in one or more electrode locations. As we can see the marked cycles constitute less than the half of the high emitting cycles. This can be explained as follows: 6000 ppm C1 at a relative air/fuel ratio of 1.55 means that the exhausted unburned mixture is about 5-8%. The arrival times at the ionization probes correspond to about 90%

mass fraction burned and hence it is likely that the partial burn occurs after the flame has arrived at the probe. Thus for the partial burn to be visible on the ionization probe, we need to go to relative air/fuel ratios appreciably higher than 1.5.

6.3 Changing the sampling location

In an attempt to quantify the above observations the location of the FID sampling probe was moved close to the exhaust valve seat (Fig. 6.14). This would enable us to obtain hydrocarbon emission signatures that could be directly related to the physical processes taking place during the blowdown period and the exhaust stroke. The disadvantage of this method is that the emission signature depends on the radial position of the probe. Hence the emission profile cannot be mass averaged because a major assumption in the mass averaging process is that the hydrocarbon concentration is uniform across the exhaust pipe section. The sampling location was thus moved to three different places: 1 cm from the valve seat center of the tube, 2 cm from the valve seat center of the tube and 1 cm from the valve seat close to the exhaust port wall. The two new sampling locations compared to the previous one are shown schematically in Fig. 6.14. Typical emission profiles for the case of 1 cm from the exhaust valve were averaged and compared (Fig. 6.15) to verify that the hydrocarbon concentration varies across the exhaust port. The three locations give different profiles that are radically different compared to the ones sampled 15 cm from the valve seat. They agree, however, in the conclusions that can be drawn from them. The existence of cycles falling into one of the four categories defined above is still evident and the hydrocarbon emissions profile again follows the expected pattern. The exact shape of the profile is different but now cycles from region 3 have a peak in the beginning and in the end of the exhaust stroke and cycles from region 4 have a peak at the end of the exhaust stroke. The change in the shape of the emission profiles depending on the sampling location is to be attributed to non uniform flow out of the cylinder, incomplete mixing and varying oxidation of the exhaust gases in the exhaust port. Figure 6.16 shows profiles-examples of signatures having a peak at the beginning (blowdown)

and the end of the exhaust stroke (hence belonging to region 3) or later on in the exhaust stroke (belonging to region 4) and a signature of a normal (region 1) cycle. The above observations are consistent with the previous ones (sampling location 15 cm from exhaust valve) in 90% of the cases. A possible explanation for that is that while sampling at one radial position in the exhaust port the profile is different at other positions thus providing us with 'incomplete' information. Table 6.1 contains an analysis performed on one data set. For this data set the high emitting cycles have been investigated and separated as above into two categories: globally slow burning and locally slow burning. Their mass fraction is also tabulated as well as a description of their hydrocarbon emission profiles. Instead of the IMEP the ionization probe contours could be used in order to determine the speed of burning. The IMEP was preferred, however, because it represents a well known measure of the quality of combustion. Thus cycles can be compared between them in order to see whether the phenomenon observed above (i.e. faster burning cycles with higher IMEP having a localized slow burn region tend to have a peak in their hydrocarbon concentration towards the end of the exhaust stroke) is also evident here. In order to facilitate the comparison the cycles having the same mass fraction burned are grouped together.. Datasets obtained at the other two locations (close to the valve seat) agree with the one presented here. Table 6.2 gives the relevant information for the case of sampling 15 cm away from the exhaust valve and Table 6.3 give the results of the analysis performed on a set with sampling close to the exhaust valve and $\lambda=1.5$.

6.4. Conclusions

The series of experiments performed enabled us to verify that when the relative air/fuel ratio is high the importance of post flame oxidation is diminished. This can be attributed to the lower temperatures resulting from burning a significantly smaller amount of fuel. As a result, although when close to stoichiometry there is no correlation between burn rate and

hydrocarbon emissions, the two variables start to become correlated when the engine is running substantially lean.

The partial burns resulting from poor combustion quality at these equivalence ratios take place at the very end of the combustion process (when the in-cylinder conditions are least favorable for combustion). The unburned mass fraction is of the order of 15 % and hence partial burns were not always observable on the ionization probe arrival times which coincide approximately with the 80% mass fraction burned interval.

Partial burns can be the result of either a globally slow burning cycle or a locally slow burning or quench region. The relation between the burn rate of a cycle, its IMEP, the mass fraction burned and the hydrocarbon profile is very complicated but useful comparisons can be made by keeping one or more of the above variables constant. The data suggest that a fast burning cycle with the same fraction burned (or actually unburned) as a slow burning cycle is expected to have higher hydrocarbon emissions. Table 6.4 summarizes the observations made above for the slow burning cycles.

Table 6.1 Comparison of single cycle hydrocarbon emission profiles

Operating cond: 1600 rpm, lambda=1.45

Mass fraction Burned (region)	IMEP (bar)	Hydrocarbon emission profile description
74% (3)	2.071	Peaks at the beginning and the end *
79% (4)	2.586	Peak at the end *
85% (4)	3.13	Peak at the end *
86% (3)	2.525	Peak at the beginning *
86% (4)	3.125	Whole of exhaust stroke (not beginning)*
87% (3)	3.068	Peak at the end
89% (4)	3.282	Peak at the end *
89% (3)	3.065	Peaks at the beginning and the end *
91% (3)	3.316	Peaks at the beginning and the end *
91% (4)	3.44	Peak in the end *

* means agreement with proposed explanation

Although difficult to compare the second case we see that since it has the same IMEP with the fourth case and case 4 was a slow burning one with respect to the mass fraction it burned then case 2 must be a fast burning one w.r.t. to the mass fraction it burned.

Table 6.2 Comparison of single cycle hydrocarbon emission profiles

Operating cond: 1600 rpm, lambda=1.45

Mass fraction Burned (region)	IMEP (bar)	Hydrocarbon emission profile description
85% (3)	2.831	Peak at the beginning*
85% (3)	3.153	Peak at the beginning and the end*1
86% (3)	3.166	Peak at the beginning*
87% (4)	3.318	Peak at the end*
87% (4)	3.209	Peak at the beginning and the end*1
87% (3)	3.013	Peak at the beginning*
89% (4)	3.519	Whole of the exhaust stroke*1
91% (4)	3.586	Peak at the end

* means agreement with proposed explanation

*1 means that we are close to the line dividing the two regions and so not suprisingly a combination of both behaviors is observed

Note that description of profiles here differs slightly from that of tables 6.1 and 6.3 as discussed in text.

Table 6.3 Comparison of single cycle hydrocarbon emission profiles

Operating cond: 1600 rpm, lambda=1.5

Mass fraction Burned (region)	IMEP (bar)	Hydrocarbon emission profile description
73% (3)	2.504	Peaks at the beginning and the end
74% (3)	2.529	Peaks at the beginning and the end
81% (3)	2.722	Peaks at the beginning and the end*
82% (3)	2.765	Peaks at the beginning and the end*
84% (3)	2.740	Peaks at the beginning and the end*
86% (3)	2.888	Peaks at the beginning and the end*
88% (4)	3.033	Peak at the end*
88% (3)	2.879	Peak at the beginning and the end*
90% (3)	3.228	Peak at the beginning and the end*
90% (4)	3.406	Peak at the end*

* means agreement with proposed explanation

Note that due to the leaner operating condition cycles of region 3 tend to be more common than cycles of region 4.

Table 2: Summary

Region	Characteristics	IMEP (bar)	Mass Fraction Burned	exhaust [HC] emission index
1 and 2	Normal cycles, slightly increasing HC emissions with decreasing burn rate.	3.5-5	91-95%	3-5%
3	Globally slow burning cycles, low IMEP, high emissions due to incomplete burn. Most of emissions during blowdown.	2-3.5	75-90%	6-8%
4	'Relatively' fast cycles. Localized partial burn. Higher IMEP and emissions (compared to region 3 for the same mass fraction burned). Most of emissions during displacement part of exhaust stroke.	2-3.5	75-90%	6-8%

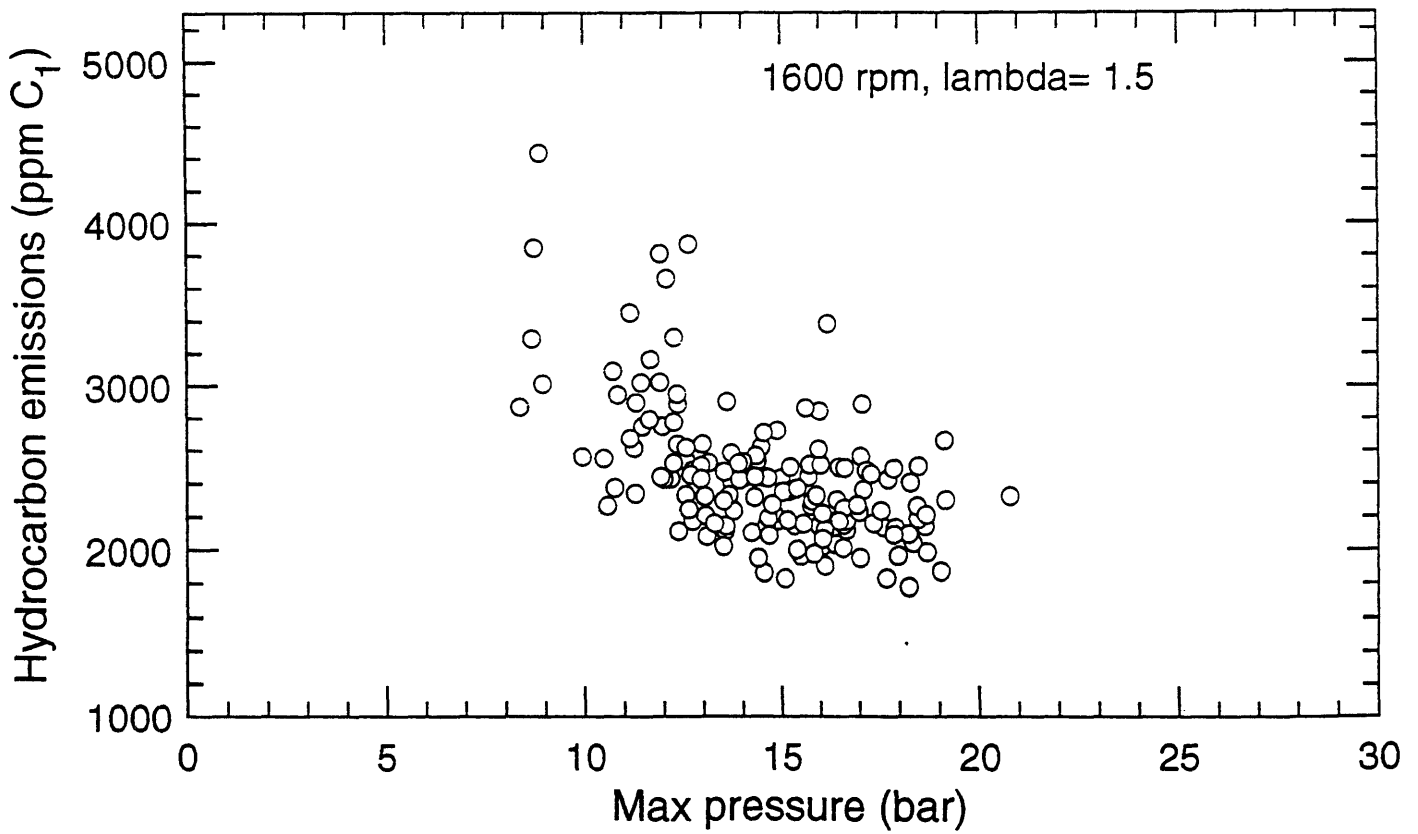
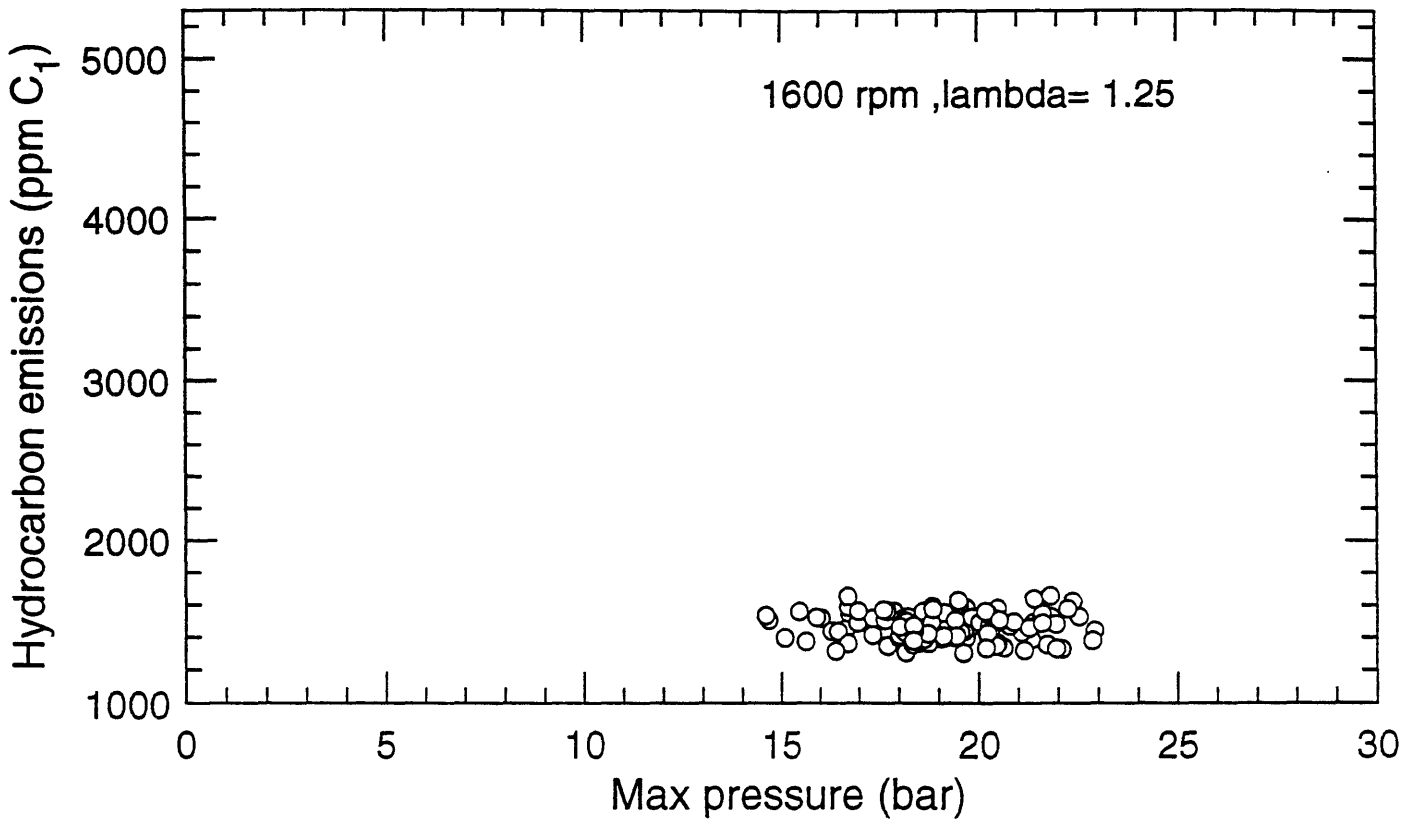


Figure 6.1 Mass averaged hydrocarbon emissions plotted against max pressure for 120 cycles.

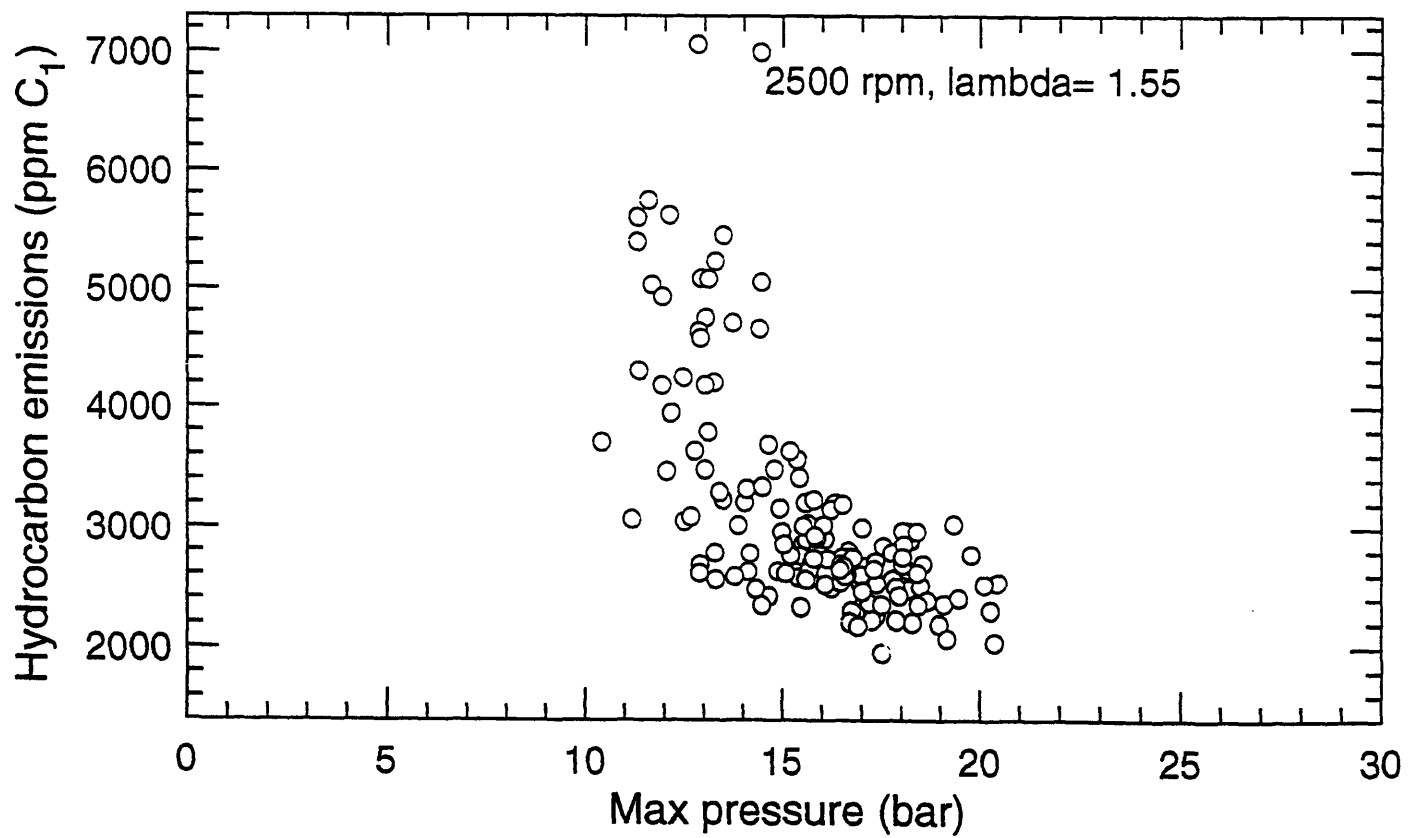
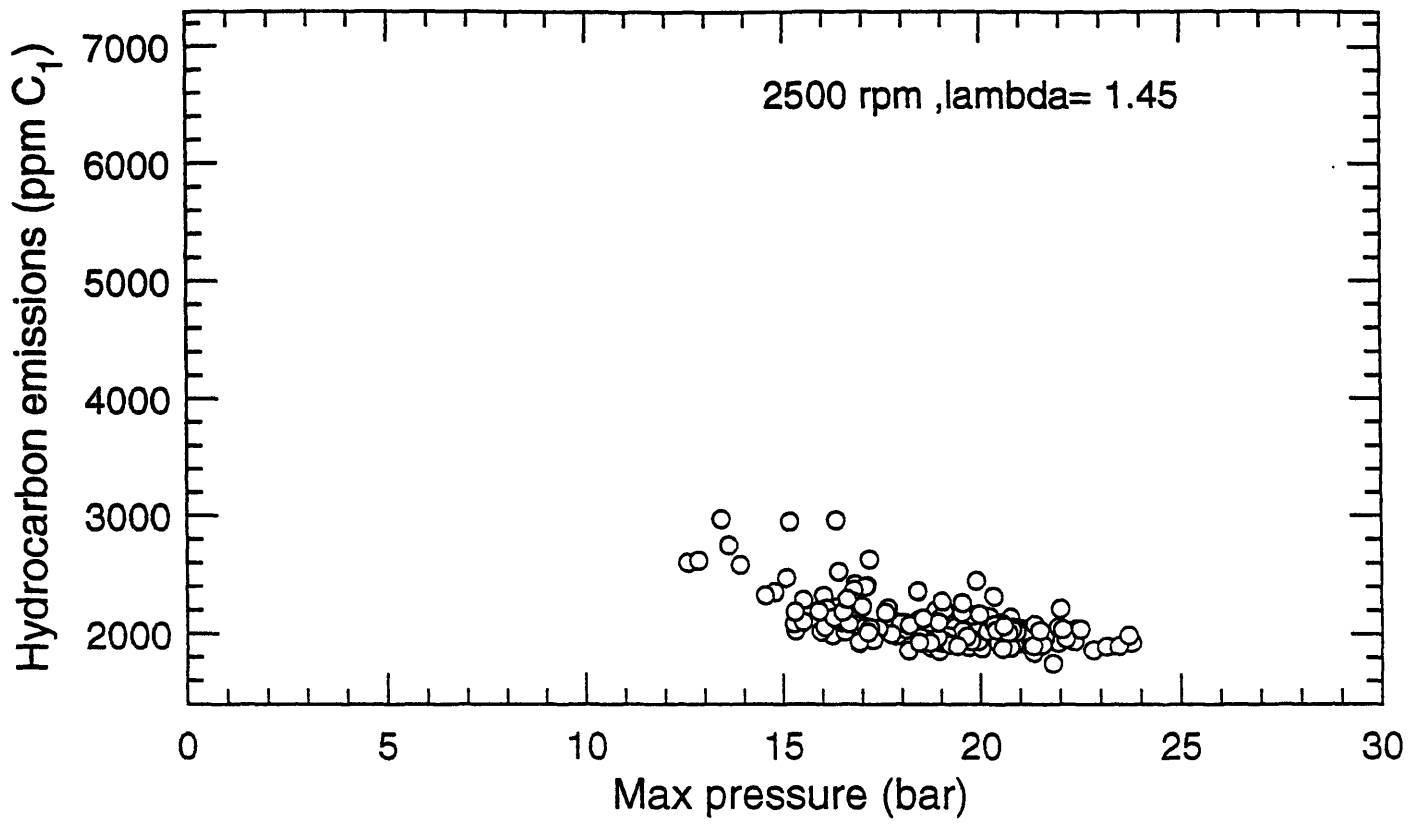


Figure 6.2 Mass averaged hydrocarbon emissions plotted against max pressure for 120 cycles.

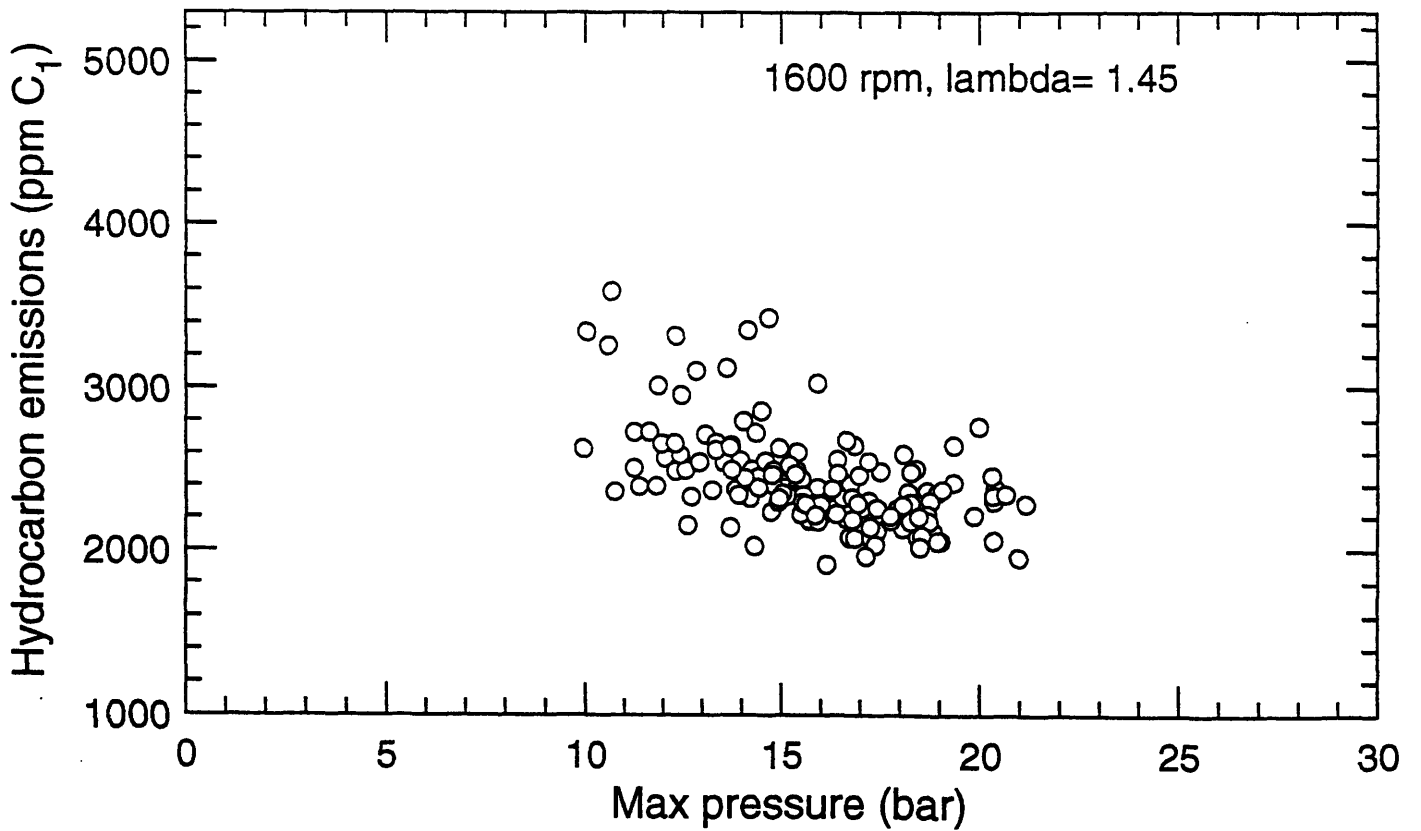
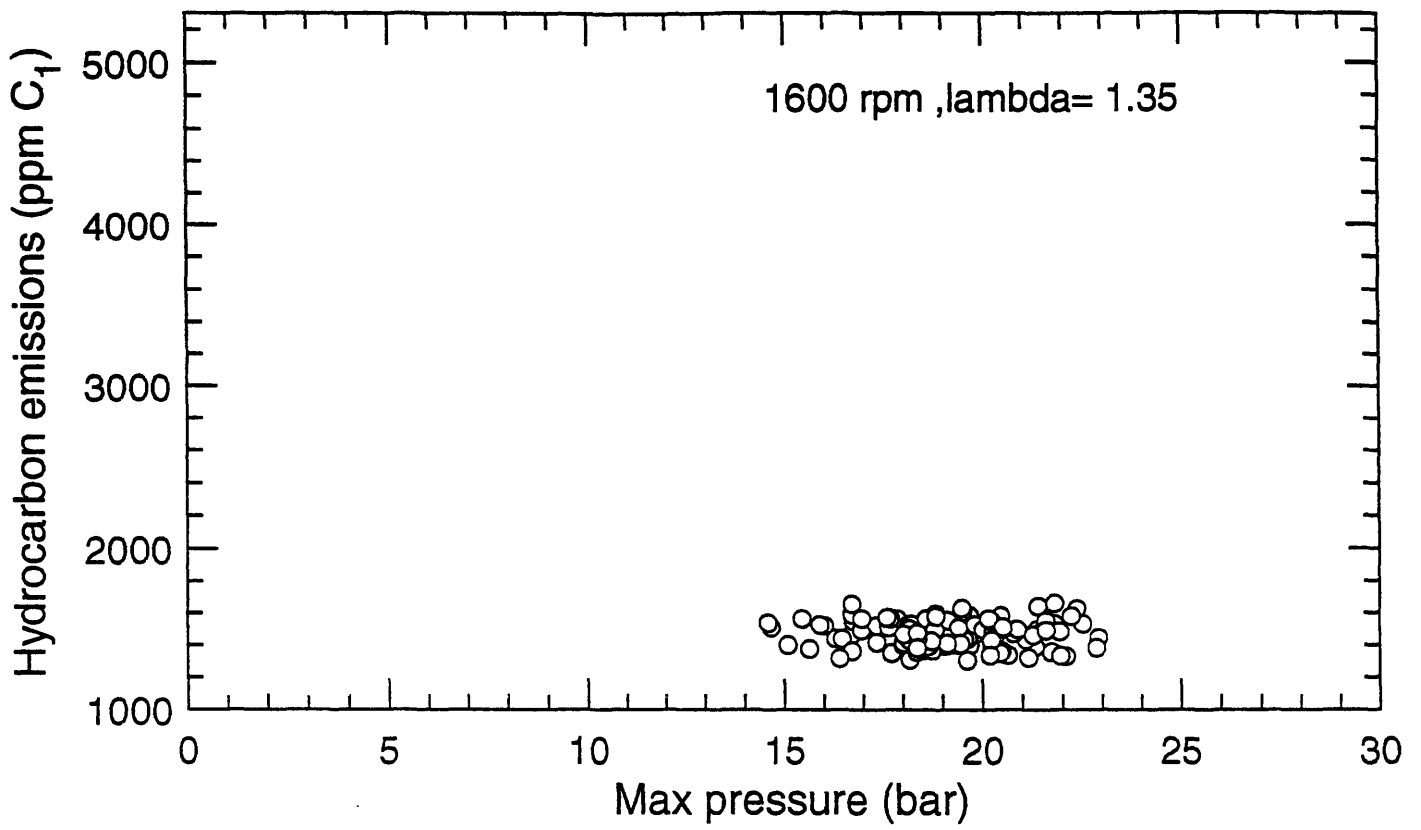


Figure 6.3 Mass averaged hydrocarbon emissions plotted against max pressure for 120 cycles.

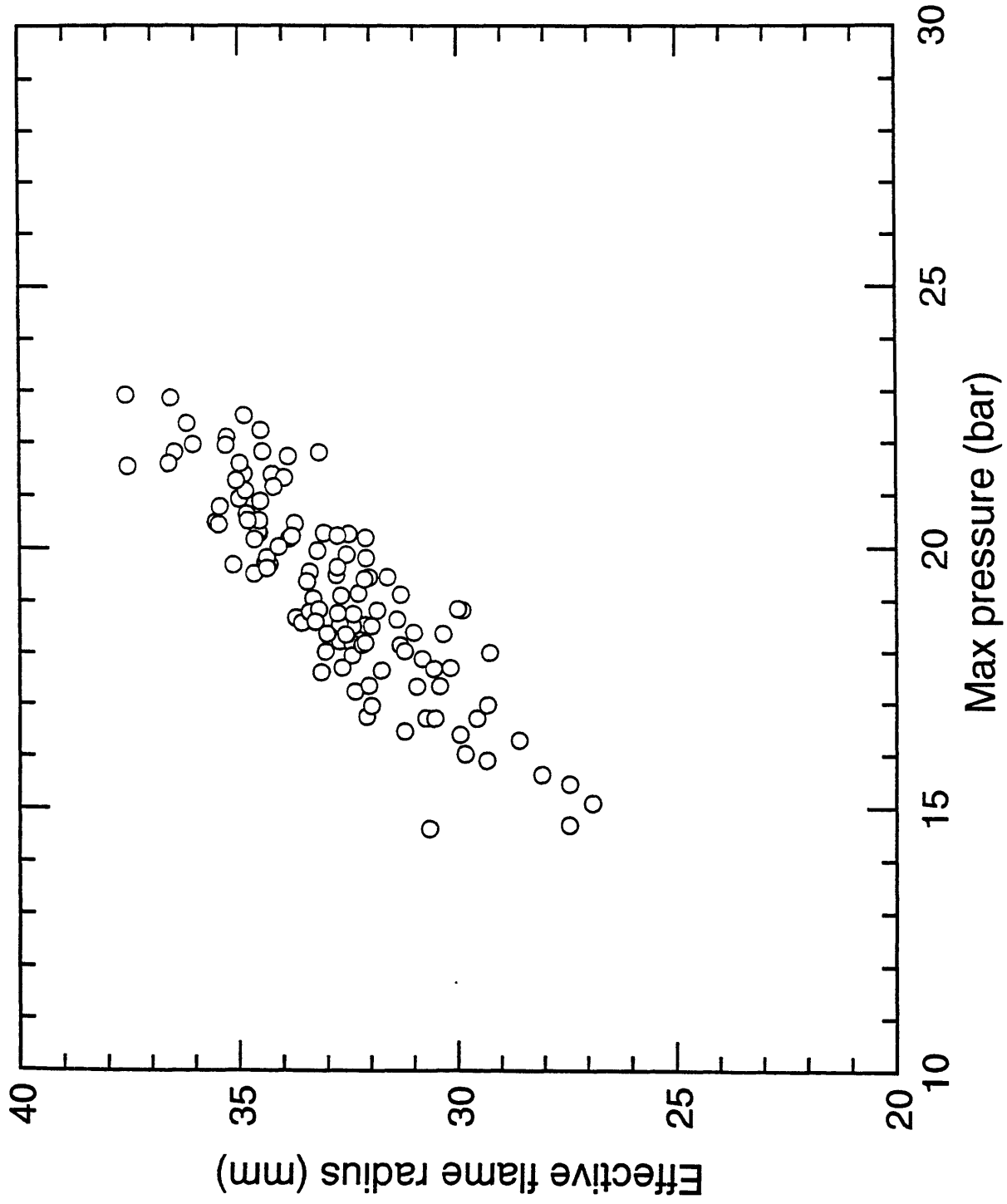


Figure 6.4 Relation between the 'Effective flame radius' and max pressure for 120 cycles at 1600 rpm 0.5 bar and $\lambda=1.45$.

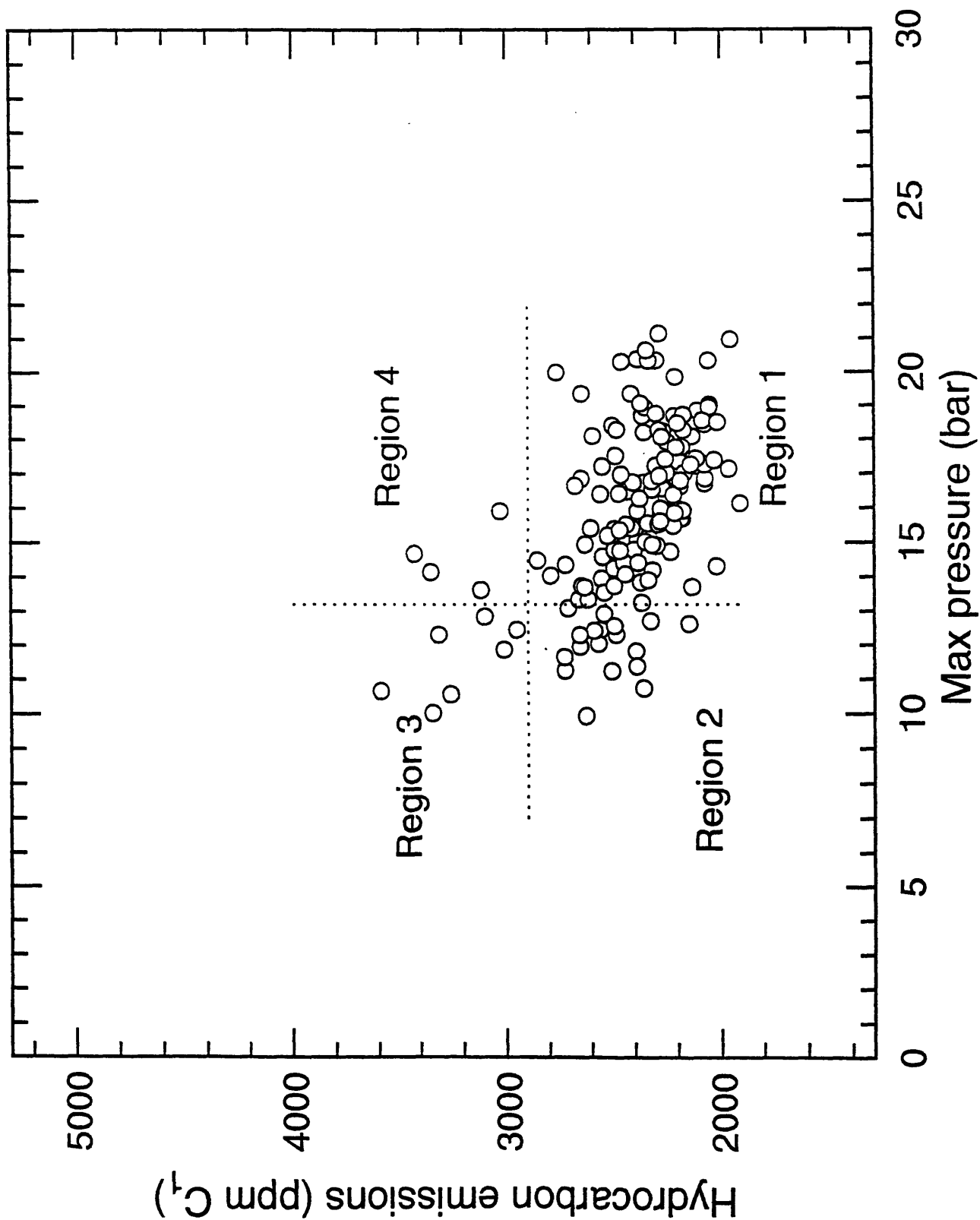


Figure 6.5 Investigation of single cycle behavior.

Average results for 300 cycles

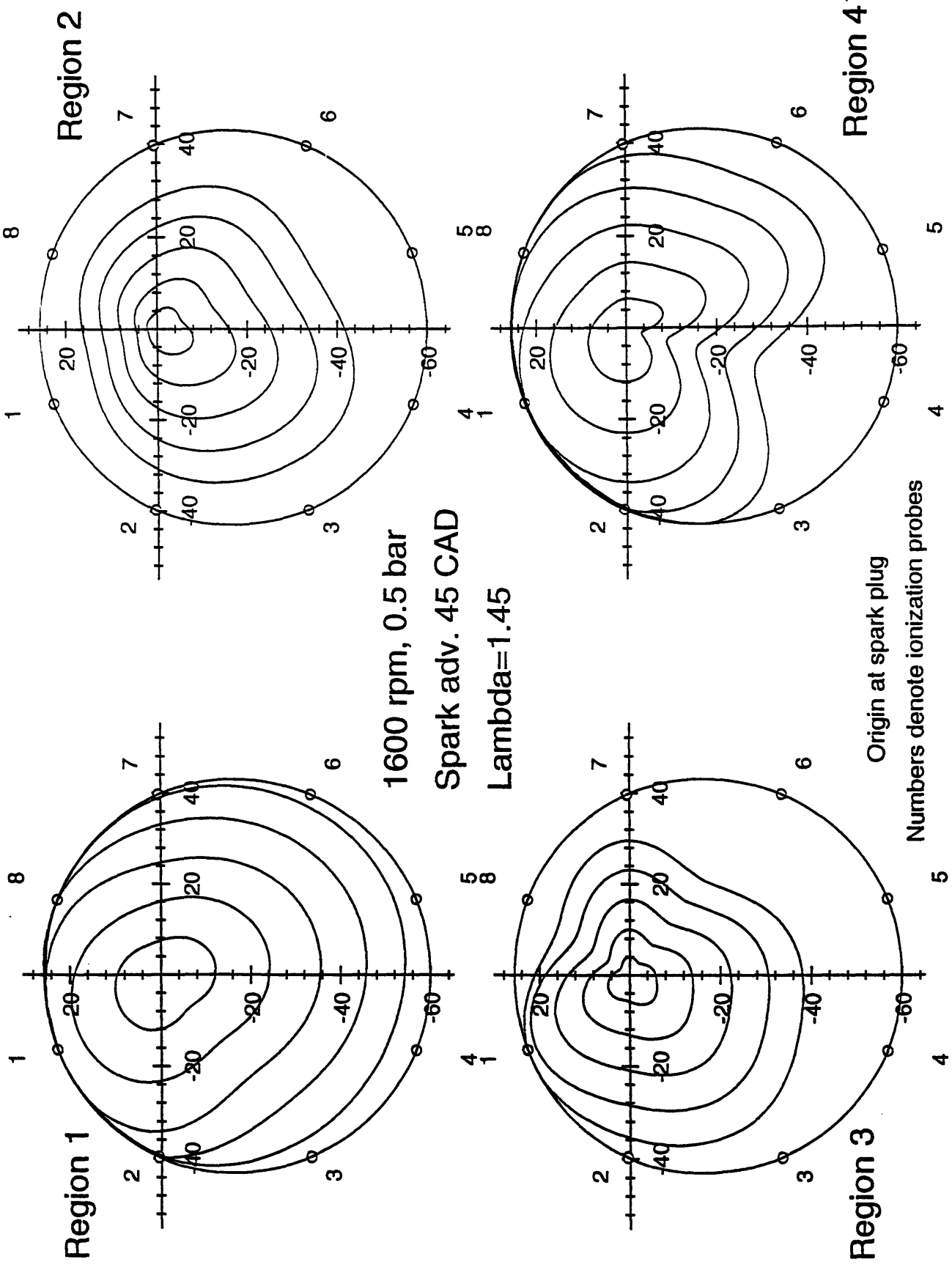


Figure 6.6 Representative flame evolution contours for the four regions identified in figure 6.5.

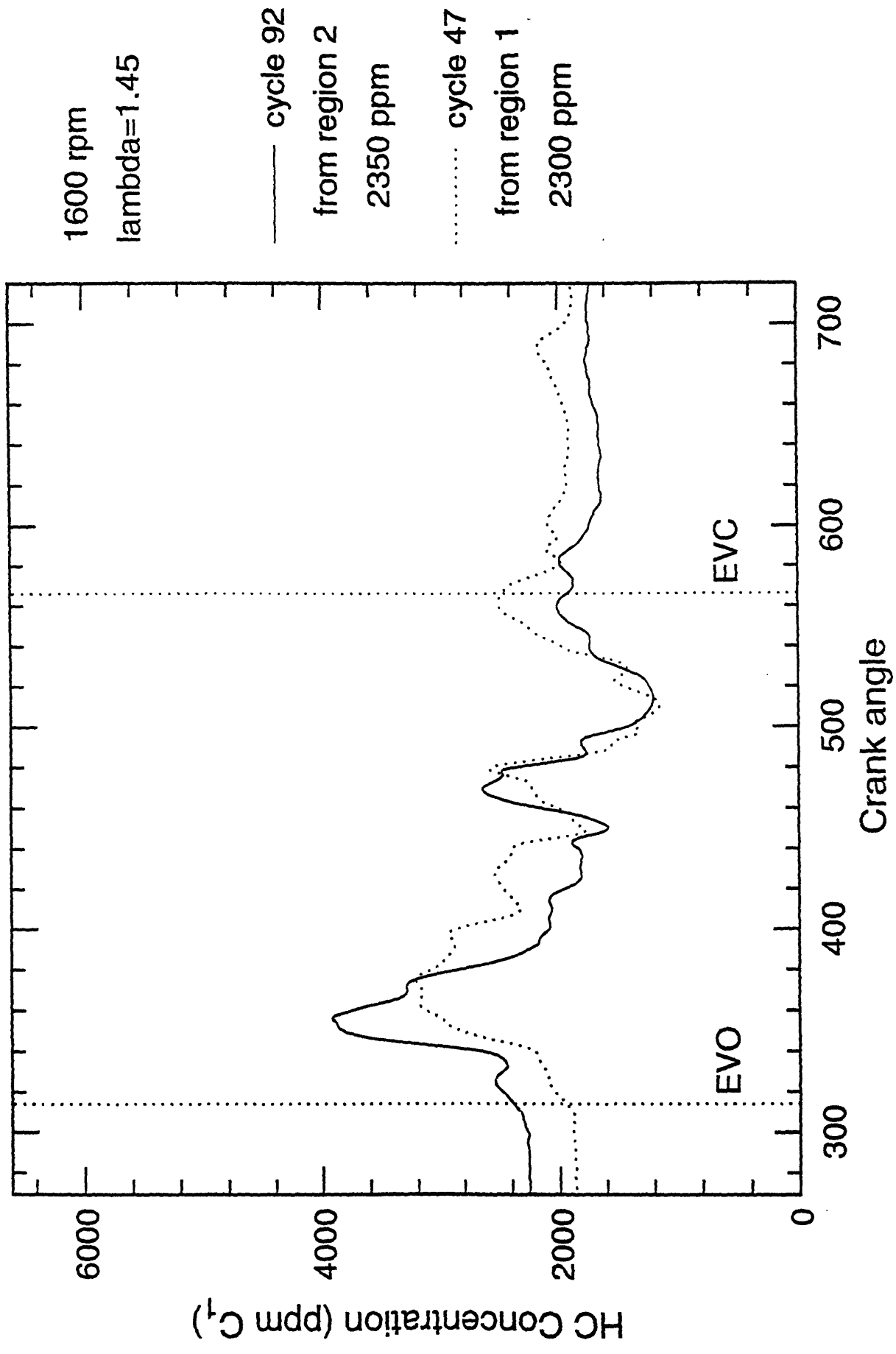


Figure 6.7 Representative single cycle hydrocarbon emissions profiles for the regions identified in figure 6.5.

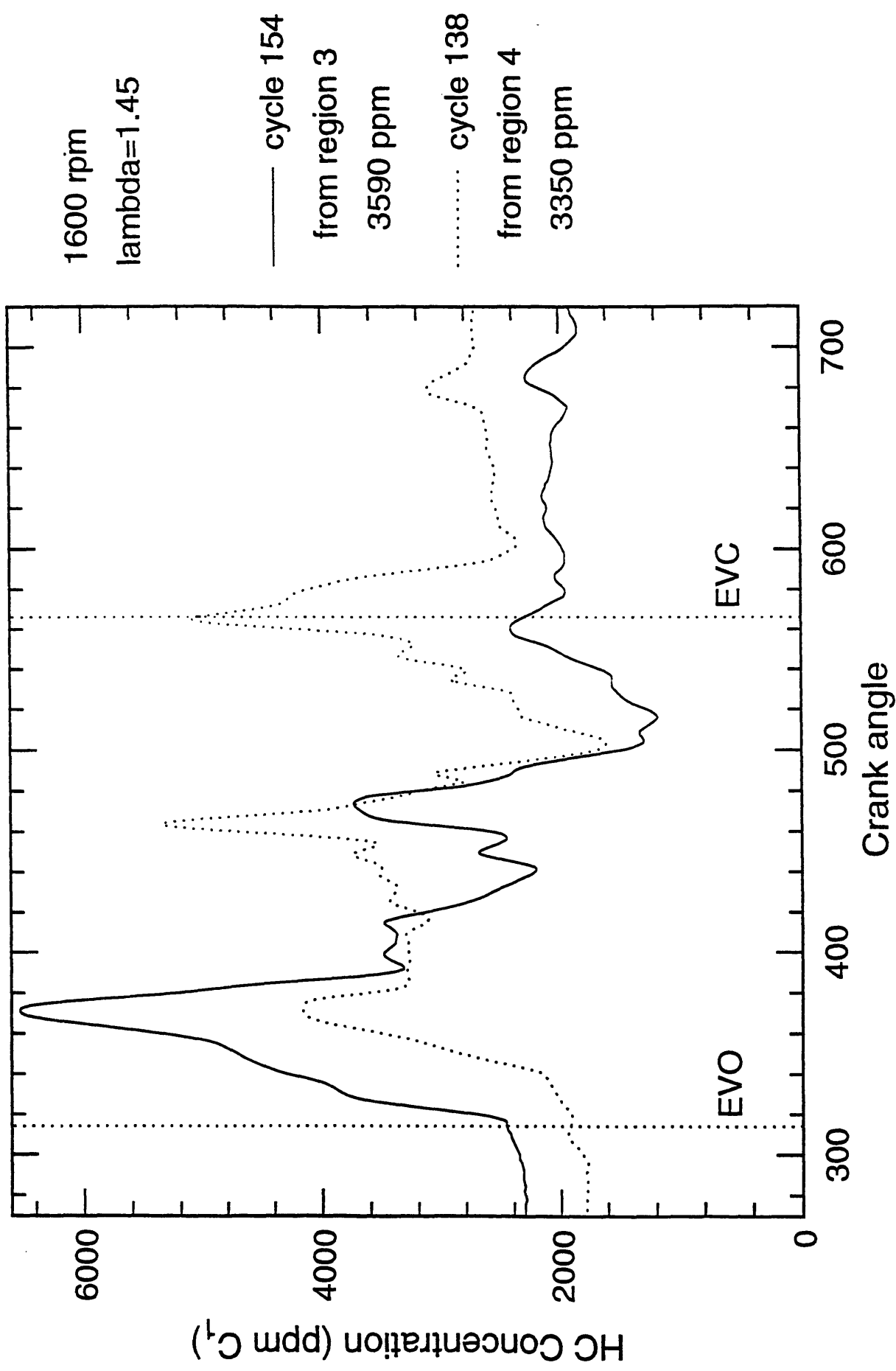


Figure 6.8 Representative single cycle hydrocarbon emissions profiles for the regions identified in figure 6.5.

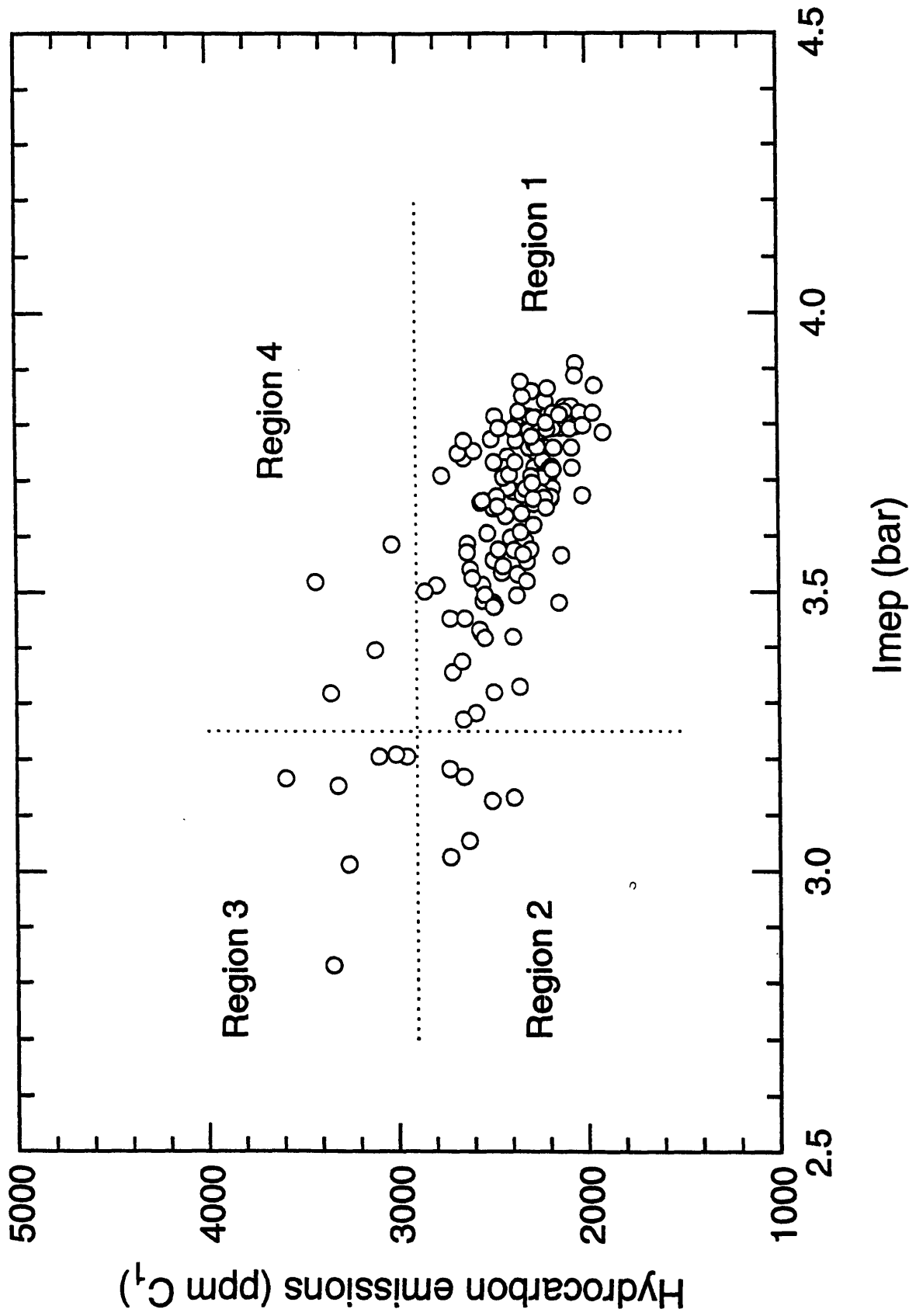


Figure 6.9 Mass averaged hydrocarbon emissions plotted against cycle IMEP for 120 cycles at 1600 rpm, 0.5 bar, lambda= 1.45.

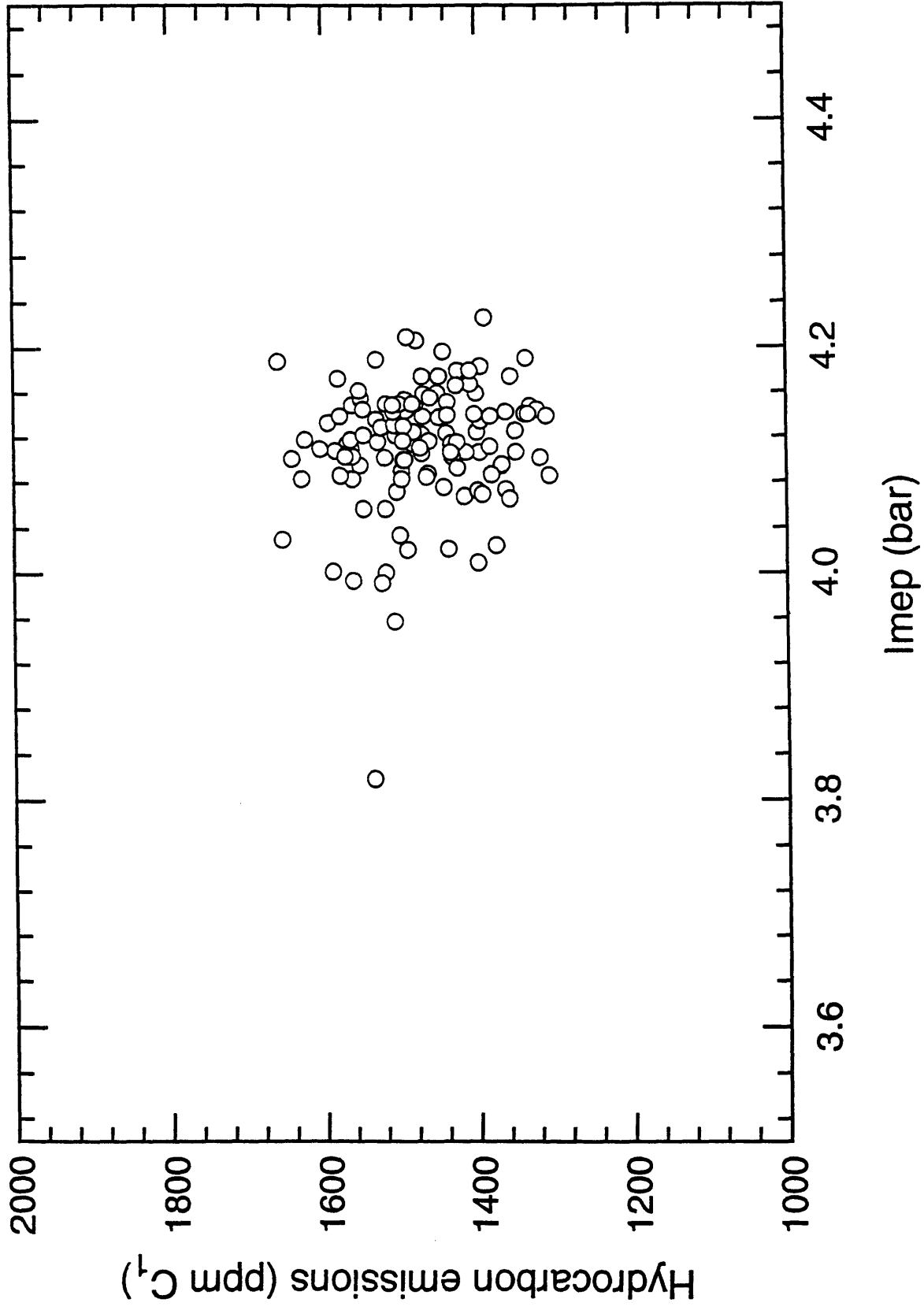
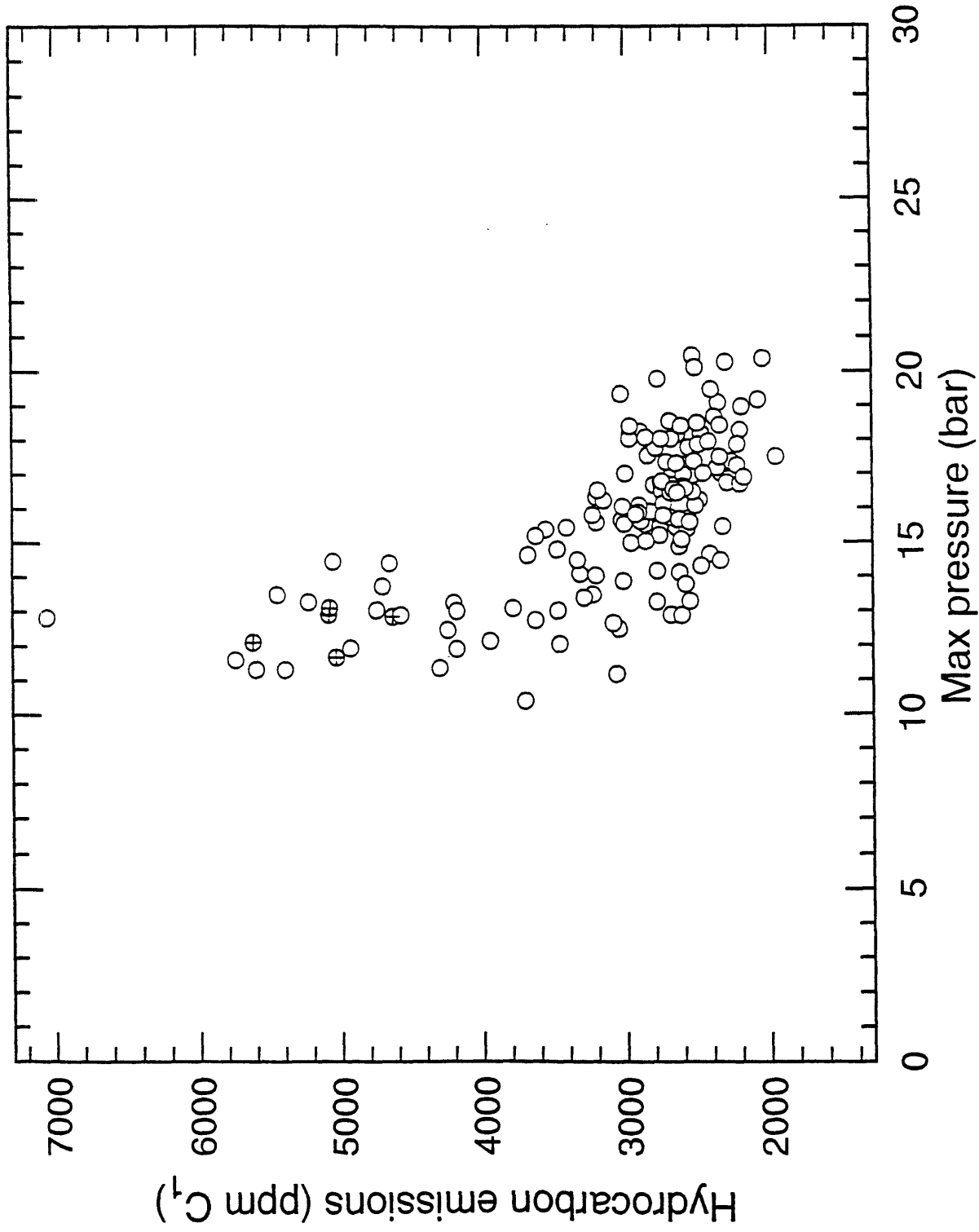
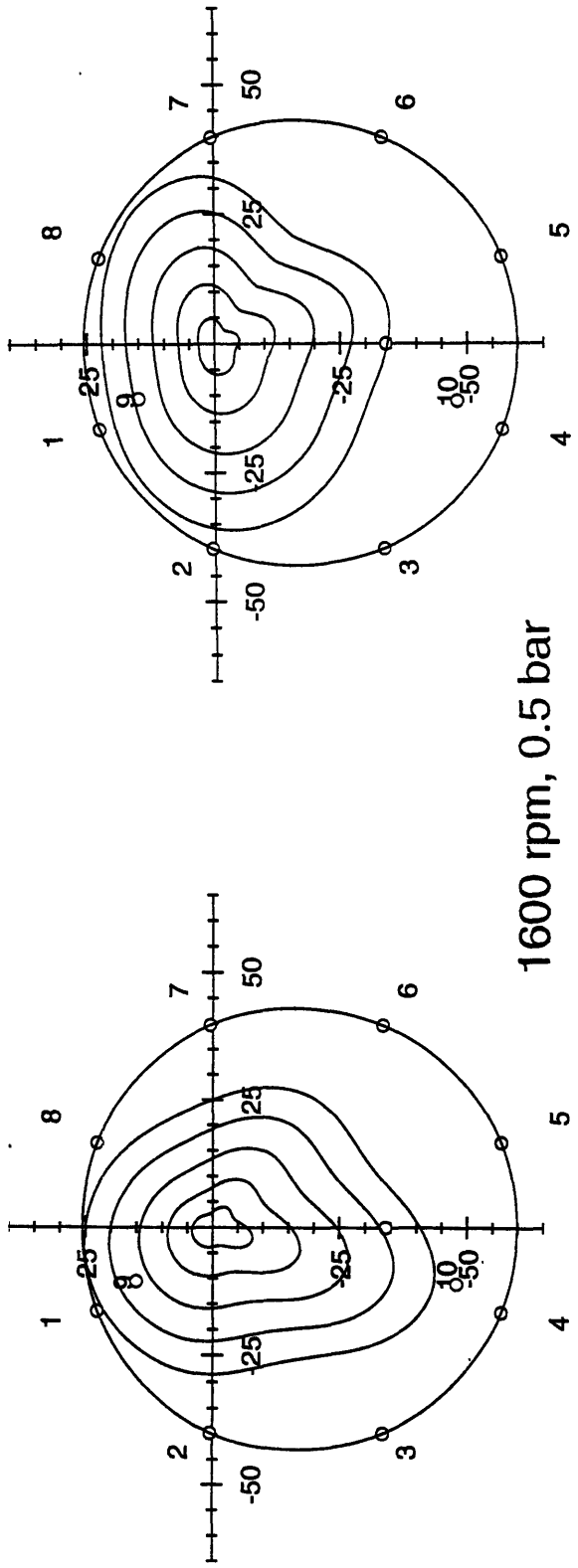
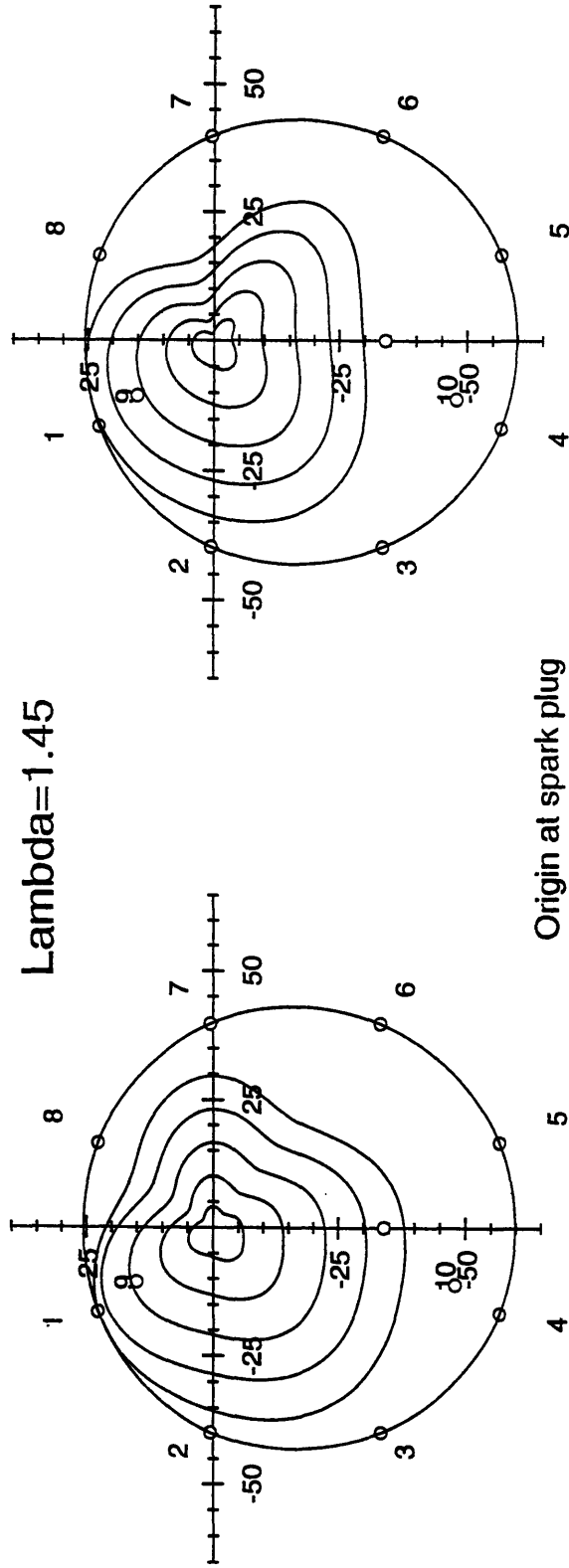


Figure 6.10 Mass averaged hydrocarbon emissions plotted against cycle IMEP for 120 cycles at 1600 rpm, 0.5 bar, $\lambda=1$.





1600 rpm, 0.5 bar
 Spark adv. 45 CAD
 $\Lambda = 1.45$



Origin at spark plug
 Numbers denote ionization probes

Figure 6.12 Examples of individual cycles from region 3

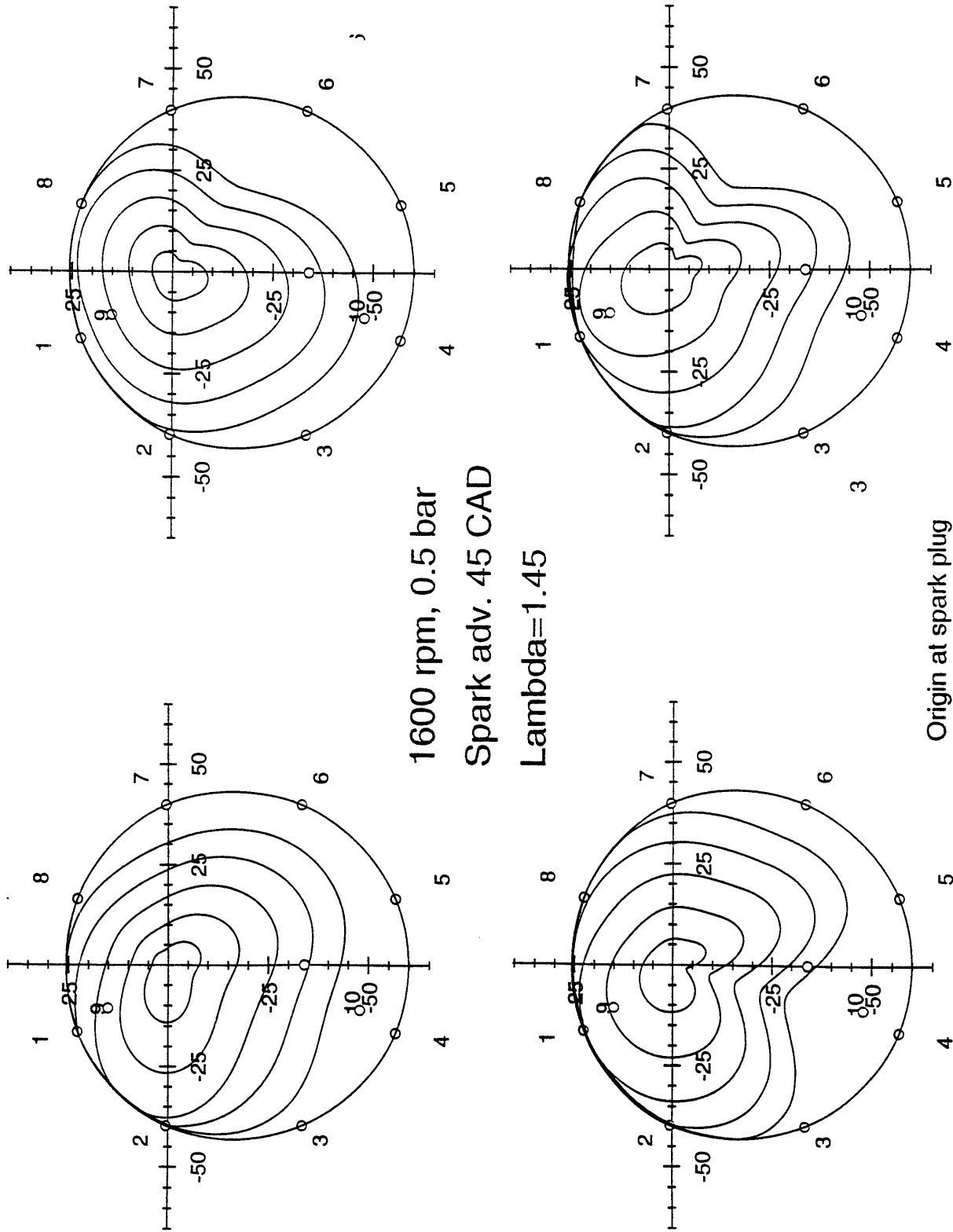


Figure 6.13 Examples of individual cycles from region 4

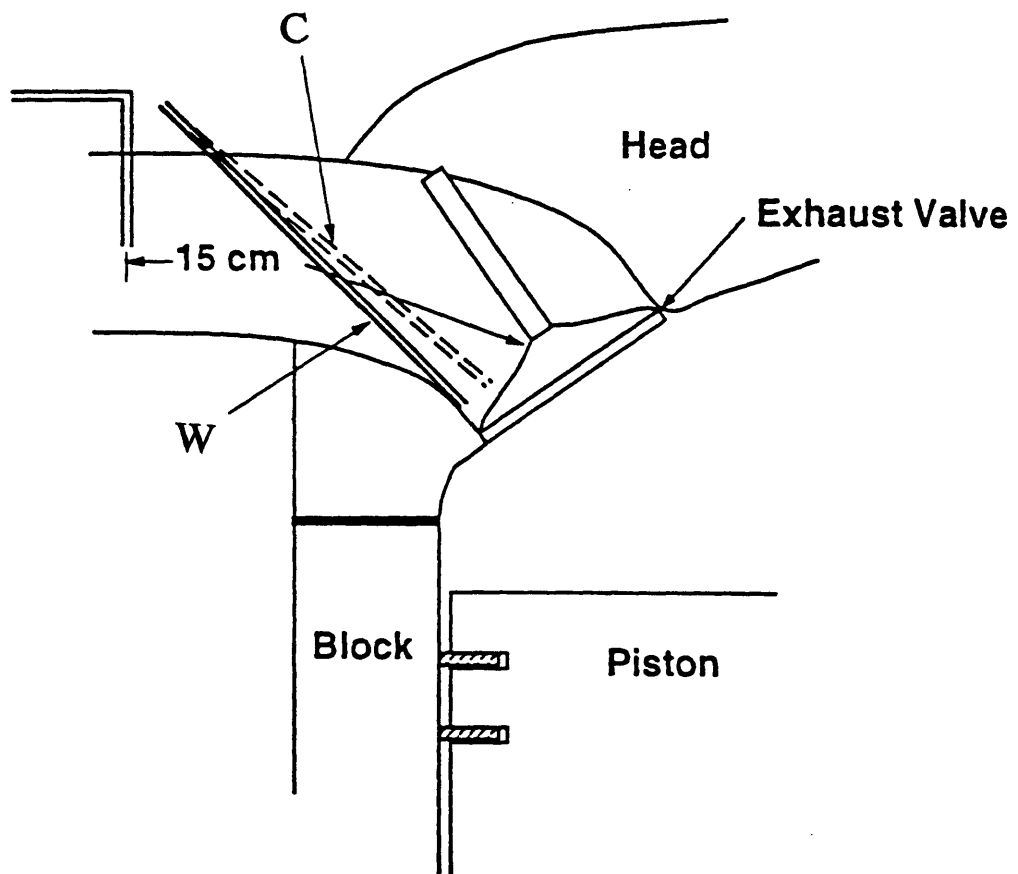


Figure 6.14 Schematic of the three different sampling locations for the FR FID.

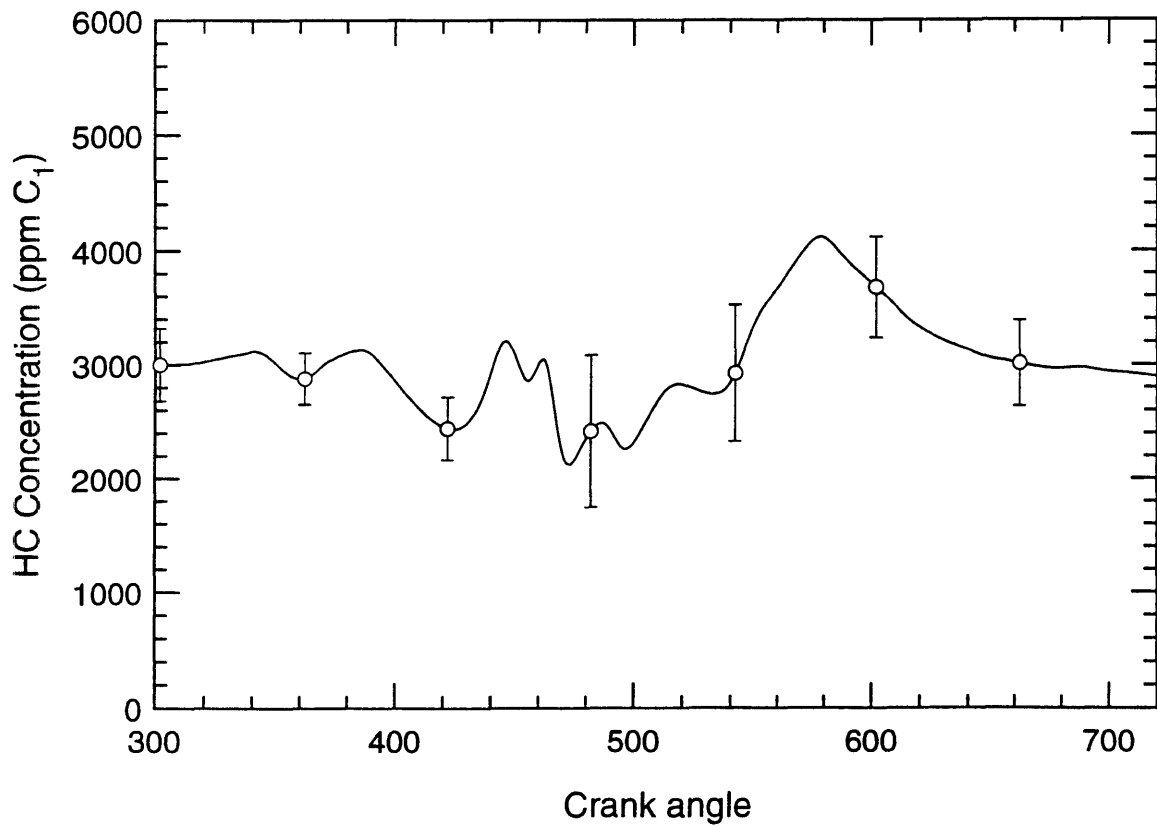
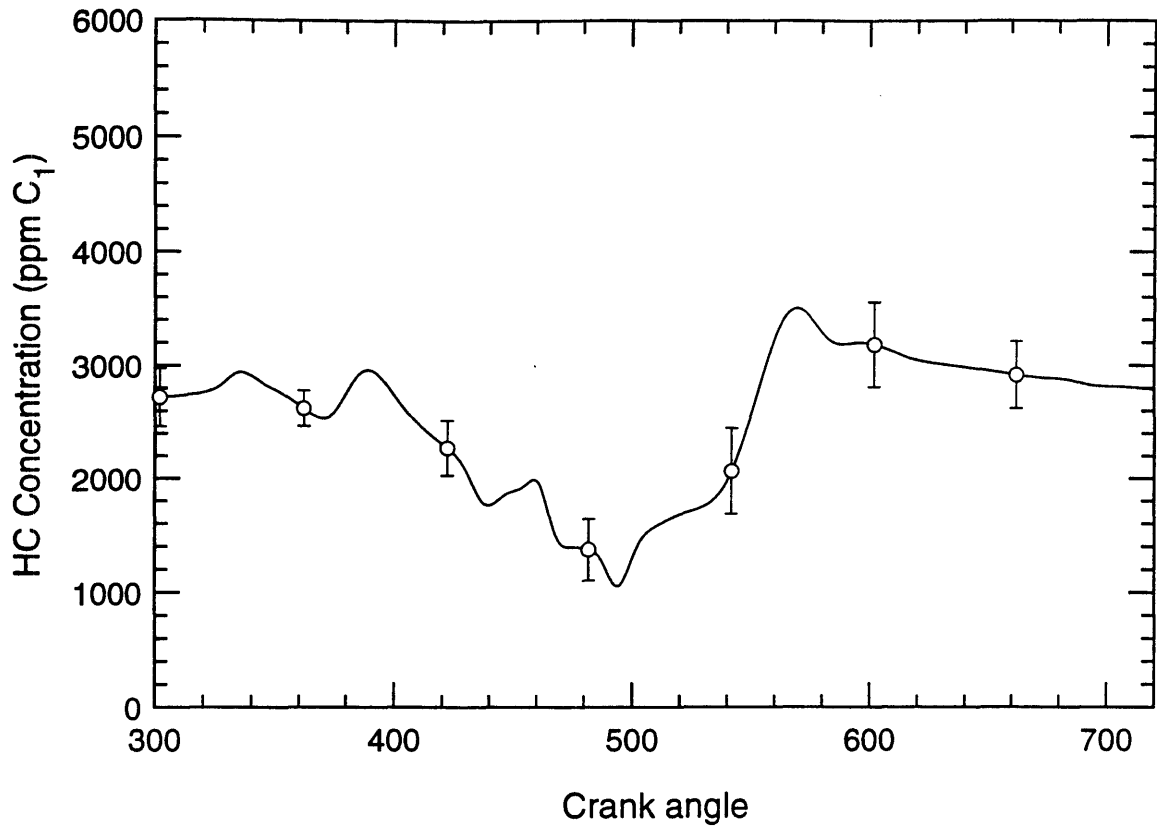


Figure 6.15 Averaged emission profiles (200 cycles) at different sampling positions close to exhaust valve at 0.5 bar and $\lambda=1$. Sampling in the center of the exhaust port (top) and close to the port wall (bottom).

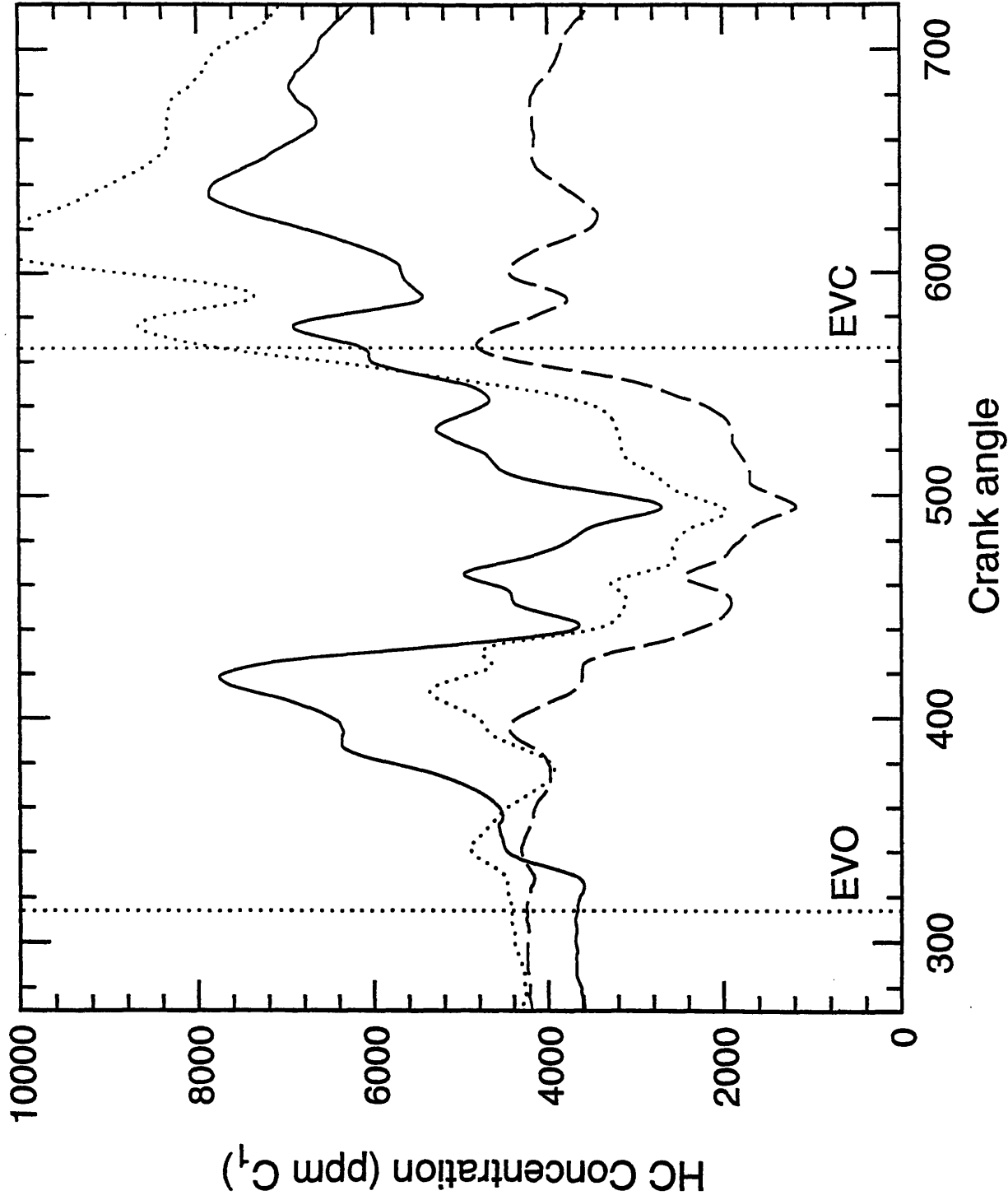


Figure 6.16 Examples of different high hydrocarbon emitting behavior at 1600 rpm, 0.5 bar, $\lambda = 1.45$.

Chapter 7: Summary and conclusions

7.1 Summary

A head gasket ionization probe circuit providing flame arrival times at eight different points on the cylinder liner has been successfully implemented. The probe has been working for more than 100 hours with no operational problems. The engine speed was limited to 2500 rpm and the maximum inlet pressure was 0.5 bar for sustained operation and 0.7 bar for intermittent operation.

A model was developed that converts the flame arrival times at this ionization probe to flame contours at any desired time. The model is based on flame contour data taken from the literature. Experiments were run to validate the model predictions and good agreement was found. The experiments included varying fuel/air ratios, engine speeds, and cylinder flowfields.

Experiments were also run under marginal combustion conditions. A fast response FID was used to measure the hydrocarbon emissions of the engine. The experiments were repeated with the sampling probe of the instrument being close to the exhaust valve and 15 cm away from it. The conclusions drawn are consistent and independent of the sampling location. The ionization probe signals become very weak when the relative air/fuel ratio becomes higher than 1.4 (approximately). Flame arrival triggering problems set in before misfires become frequent and so extensive study of misfires or partial burns was not possible.

7.2 Conclusions

- 1) Ionization probe signals signify flame arrival by a rise in signal strength. The most appropriate way to trigger flame arrival is to set a threshold value of the order of 10 % of the difference between the maximum and minimum signal value.

2) The flame inside the cylinder of a SI Engine can be assumed to propagate in all directions, and independently of operating conditions, obeying the same general relation which, however, depends on the engine. A more general scaling relation in terms of the entrainment velocity that is obeyed by all engines can be obtained.

3) A model based on the above mentioned relations provides flame contours that are in good agreement with measurements. The model also suggests a turbulent flame brush thickness of 2-3 mm. The mass fraction of the unburned fuel contained in the flame brush is estimated to be of the order of 10 %.

4) In contrast to the operation close to stoichiometry, exhaust hydrocarbon emissions increase rapidly with increasing relative air/fuel ratio, when this ratio approaches a value of 1.4. At these values of relative air/fuel ratio post flame oxidation becomes less important.

5) Partial burns at the above mentioned operating conditions take place at the end of the combustion process (when the charge left to burn is of the order of 15 % of the total initial charge).

6) Partial burns result either from localized slow burning regions or global slow burning. The two causes of partial burning can be identified via the ionization probe or by using a fast response FID.

Appendix A: Relation between apparent flame speed and entrainment speed

We choose a control volume bounding all the unburned gas. A fixed surface A_f just ahead of the flame front divides the burned by the unburned fluid and is crossed by fluid with velocity u_{gf} . The mass conservation equation is:

$$\frac{d}{dt} \int_{V_{\bar{f}}} \rho_u dV - \int_{A_f} \rho_u \underline{u}_{gf} \cdot \underline{n} dA = 0 \quad (1)$$

where $V_{\bar{f}}$ is the non-enflamed volume

Under the assumption of constant ρ_u and using the definition of the mean u_{gf} the mass conservation equation becomes:

$$\frac{d}{dt} (\rho_u V_{\bar{f}}) - \rho_u A_f \bar{u}_{gf} = 0 \quad (2)$$

The control volume varies only due to piston movement:

$$\frac{dV_{\bar{f}}}{dt} = -A_p \bar{u}_p$$

Hence

$$\bar{u}_{gf} = \frac{V_{\bar{f}} \dot{\rho}_u}{A_f \rho_u} - \frac{A_p \bar{u}_p}{A_f} \quad (3)$$

and from the definitions in chapter 4:

$$u_u = u_f - \frac{V_{\bar{f}} \dot{\rho}_u}{A_f \rho_u} + \frac{A_p \bar{u}_p}{A_f} \quad (4)$$

The overall mass balance equation gives:

$$\frac{V}{m} = x_b \left(\frac{1}{\rho_b} - \frac{1}{\rho_u} \right) + \frac{1}{\rho_u} \quad (5)$$

Taking the time derivative and neglecting the rate of change of $\frac{\rho_u}{\rho_b}$ we get:

$$\frac{\dot{\rho}_u}{\rho_u} + \frac{\dot{V}}{V} \equiv \frac{m x_b}{\rho_u V} \left(\frac{\dot{\rho}_u}{\rho_u} - 1 \right) \quad (6)$$

Multiplying both sides by $\frac{V_{\bar{f}}}{A_f}$ and using the fact that $\dot{V} = -u_p A_p$ we get:

$$\frac{V_{\bar{f}} \dot{\rho}_u}{A_f \rho_u} - \frac{A_p V_{\bar{f}}}{A_f V} u_p \equiv \frac{m \dot{x}_b V_{\bar{f}}}{\rho_u A_f V} \left(\frac{\rho_u}{\rho_b} - 1 \right) \quad (7)$$

If we neglect the piston motion we get:

$$u_e \equiv u_f - \frac{m \dot{x}_b V_{\bar{f}}}{\rho_u A_f V} \left(\frac{\rho_u}{\rho_b} - 1 \right) \quad (8)$$

Using a control volume like the previous one but with the surface separating the unburned from the burned region moving with the flame we get :

$$\frac{d}{dt} \int_{V_{\bar{f}}} \rho_u dV + \int_{A_f} \rho_u (\underline{u}_f - \underline{u}_e) \cdot \underline{n} dA = 0 \quad (9)$$

Under the previous assumptions and the definition of the average entrainment speed:

$$\frac{d}{dt} (\rho_u V_{\bar{f}}) + \rho_u A_f u_e = 0 \quad (10)$$

or

$$\dot{m}_f = \rho_u A_f u_e \quad (11)$$

Substitution of eq. (11) in eq. (8) gives:

$$u_e \equiv u_f - u_e \left(\frac{\rho_u}{\rho_b} - 1 \right) (1 - y_b)$$

where y_b is the burned volume fraction. After rearrangement we get the required:

$$u_f \equiv u_e \left[(1 - y_b) \frac{\rho_u}{\rho_b} + y_b \right] \quad (12)$$

Appendix B: Fitting coefficients for the Ricardo Hydra engine

The relation for the flame evolution profile for the Ricardo Hydra engine is:

$$y = Ax^5 + Bx^4 + Cx^3 + Dx^2 + Ex + F$$

where y is $r/25$ mm and x is t/t_0 , where t_0 is the time taken by the flame to reach a radius of 25 mm, and the constants A, B, C, D, E, F take 4 different values depending on the direction of flame propagation.

For probes 4 and 5: $A = -1.11483E-1$, $B = 7.67084E-1$, $C = -2.09495$, $D = 2.66163$, $E = 1.75756E-1$, $F = -5.46269E-2$.

For probes 3 and 6: $A = -2.72204E-1$, $B = 1.58894$, $C = -3.66023$, $D = 4.06407$, $E = -7.97336E-1$, $F = 6.70956E-2$.

For probes 2 and 7: $A = -7.3437E-1$, $B = 3.48633$, $C = -6.57829$, $D = 6.13392$, $E = -1.45728$, $F = 1.36638E-1$.

For probes 1 and 8: $A = -1.22256$, $B = 4.30965$, $C = -6.2144$, $D = 4.74409$, $E = -6.13084E-1$, $F = -1.74974E-2$.

References:

- 1 Schnauffer, K. "Engine-Cylinder Flame-Propagation Studied by new Methods" SAE Transactions, Vol. 34, 1934.
- 2 Muller, K., Linder, E. and Maurer, H., U.S. Patent 4,393,687, 1983.
- 3 Witze, P. "Cycle-Resolved Multipoint Ionization Probe Measurements in a Spark Ignition Engine", SAE Paper 892099, 1989.
- 4 Witze, P. and Bopp, S. "Investigation of In-Cylinder Fluid Motion Using a Head Gasket Instrumented with Ionization Probes", SAE Paper 910719, 1991.
- 5 Nicholson, D. and Witze, P. "Flame Location Measurements in a Production Engine Using Ionization Probes Embodied in a Printed-Circuit-Board Head Gasket", SAE Paper 930390, 1993.
- 6 Min K. "The Effects of Crevices on the Engine-Out Hydrocarbon Emissions in a Spark Ignition Engine", Ph.D. Thesis, Department of Mechanical Engineering, Massachusetts Institute of Technology, 1994
- 7 Cheng, A. S., "The Head-Gasket Ionization Probe as a Combustion Diagnostic for Spark Ignition Engines" S.M. Thesis, Department of Mechanical Engineering, Massachusetts Institute of Technology.
- 8 Collings, N., "A New Technique for Measuring HC Concentration in Real Time in a Running Engine", SAE Paper 880517, 1988.
- 9 Cheng, W. K., Galliot, F. and Collings, N., "On the Time Delay in Continuous In-Cylinder Sampling from I.C. Engines." SAE Paper 890579, 1989.
- 10 Fox, J. W., Cheng, W. K. and Heywood, J. B., "A Model for Predicting Residual Gas Fraction in Spark-Ignition Engines", SAE Paper 931025, 1993.

- 11 HFR 400 High Frequency Response Flame Ionization Detector User Manual, Cambustion Ltd., 1992
- 12 Heywood, J.B. " Combustion and its Modelling in Spark Ignition Engines", COMODIA 94, Third International Symposium on Diagnostics and Modelling of Combustion in Internal Combustion Engines, Yokohama, Japan, July 11-14, 1994, pp. 1-15.
- 13 Spicher, U. and Backer, H., "Correlation of Flame Propagation and In-Cylinder Pressure in a Spark Ignition Engine", SAE Paper 902126, 1990
- 14 Baritaud, T. A., "Combustion and Fluid Dynamic Measurements in a Spark Ignition Engine: Effects of Thermochemistry and Velocity Field; Turbulent Flame Speeds", SAE Paper 892098, 1989.
- 15 Witze, P. O. and Mendes-Lopes, J. M. C., "Direct Measurement of the Turbulent Burning Velocity in a Homogeneous-Charge Engine", SAE Paper 861531, 1986.
- 16 Beretta, P. G., "Thermodynamic Analysis of Turbulent Combustion in a Spark Ignition Engine. Experimental Evidence and Analytical Methods", S.M. Thesis, Department of Mechanical Engineering, Massachusetts Institute of Technology, 1980.
- 17 Blizard, N.C. and Keck J. C., "Experimental and Theoretical Investigation of Turbulent Burning Model for Internal Combustion Engines", SAE Paper 740191, 1974
- 18 Beretta, G.P., Rashidi, M. and Keck, J.C., "Thermodynamic Analysis of Turbulent Combustion in a Spark Ignition Engine. Experimental Evidence", 1980 Spring Meeting, Western States Section, The Combustion Institute.
- 19 McCuiston, F.D., Lavoie, G. A. and Jr., " Validation of a Turbulent Flame Propagation Model for a Spark Ignition Engine", SAE Paper 770045, 1977

- 20 Hires, S. D., Tabaczynski, R. J. and Novak, J. M., " The Prediction of Ignition Delay and Combustion Intervals fro a Homogeneous Charge, Spark Ignition Engine" , SAE Paper 780232, 1978.
- 21 Tabaczynski, R. J., Ferguson, C. R. and Radhakrishnan K., "A Turbulent Entrainment Model for Spark-Ignition Engine Combustion", SAE Paper 770647, 1977.
- 22 Maly, R. R, and Herweg, R., " A Fundamental Model for Flame Kernel Formation in S.I. Engines", SAE Paper 922243, 1992.
- 23 Boulouchos, K., Steiner, T. and Dimopoulos, P., "Investigation of Flame Speed Models for the Flame Growth Period During Premixed Engine Combustion", SAE Paper 940476, 1994.
- 24 Andrews, G. E., Bradley, D. and Lwakabamba S. B., "Turbulence and Turbulent Flame Propagation --A Critical Appraisal", Combustion and Flame, Vol.24, pp. 285-304, 1975.
- 25 Abdel-Gayed R.G., Bradley D. and Lawes., M., "Turbulent burning Velocities: a General Correlation in Terms of Straining Rates", Proc. R. Soc. Lond. A 414, pp. 389-413, 1987.
- 26 Schetinkov, E.S. "Calculation of Flame Propagation in a Turbulent Flow", Combustion in Turbulent Flow (Khitrin L. N., Ed.), Moscow (English Translation, IPST (1963), pp1-40).
- 27 Wright, F.H. and Zukoski, E.E., "Flame Spreading from Bluff-Body Flame Holders", Eighth Symposium (International) on Combustion, Williams and Wilkins, pp.933-943, 1962.
- 28 Cheung, H. "A Practical Burn Rate Analysis for Use in Engine Development and Design", S.M. Thesis, Department of Mechanical Engineering, Massachusetts Institute of Technology, 1993